Reservoir Effect in bichromophoric Fe^{III} Complexes with Methylene Bridge

Supporting Information

Lennart Schmitz, Samira Dabelstein, Miguel Argüello Cordero, Lorena Fritsch, Bastian Bracht, Roland Schoch, Hans Egold, Jakob Steube, Felix Fischer, Stefan Lochbrunner and Matthias Bauer

Table of Contents

1. Experimental Section

Synthesis

The chemicals used were commercially obtained and used without further purification. Column chromatography was conducted on silica gel columns. Reactions under inert conditions were done using Schlenk techniques with argon gas or inside an argon filled glove box. Dry and degassed solvents were obtained utilizing molar sieves in an MBraun SPS solvent purifying system, and subsequent bubbling of argon. For all complexes with chromophores attached via the imidazole groups the same central ligand structure was necessary. A well-established synthetic procedure was applied to obtain 1,3-di(1H-imidazol-1-yl)benzene (1).[1] The used methyl halides for coupling were available commercially. To synthesize 2-Ph, 1 (1 eq, 1 mmol, 210 mg) was dissolved in acetonitrile (5 mL/mmol). Benzylbromide (3 eq., 3mmol, 513 mg) was added, and the solution was stirred for 16 h under reflux. After cooling to room temperature, the resulting suspension was filtered, and the product was washed with acetone.

2-Ph (1,1'-(1,3-phenylene)bis(3-benzyl-1H-imidazol-3-ium)) was obtained as a colorless solid (0.75 mmol, 485 mg, 75%).

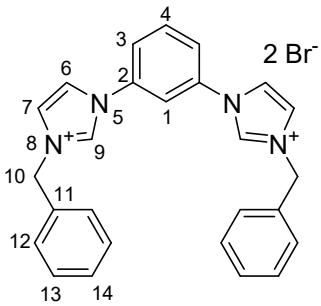

1H NMR (700 MHz, DMSO-d6): δ (ppm) = 10.35 (2H, H9, s), 8.52 (2H, H7, t), 8.46 (1H, H1, t), 8.15 (2H, H6, t), 8.06 (2H, H3, dd), 7.97 (1H, H4, t), 7.57 (4H, H12, d), 7.44-7.48 (4H, H13, m), 7.42 (2H, H14, t), 5.57 (4H, H10, s). 13C NMR (176 MHz, DMSO-d6)): δ (ppm) = 136.0 (2C, C9, CH), 135.6 (2C, C2, Cq), 134.3 (2C, C11, Cq), 131.9 (1C, C4, CH), 129.0 (4C, C13, CH), 128.9 (2C, C14, CH), 128.6 (4C, C12, CH), 123.5 (2C, C6, CH), 122.7 (2C, C3, CH), 121.6 (2C, C7, CH), 115.9 (1C, C1, CH), 52.5 (2C, C10, CH2). 15N NMR (71 MHz, DMSO-d6): δ (ppm) = 188.1 (2N, N8), 186.9 (2N, N5).

ESI-MS ([M-H]+ for C26H24N42+): m/z 391.1906. Found: m/z 391.1923.

Elemental analysis calculated for $C_{42}H_{32}N_4Br_2$: C, 56.54; H, 4.38; N, 10.14. found: C, 56.18; H, 4.66; N, 10.33

For **2-Ant**, an *in-situ* Finkelstein reaction was performed to boost yield of the alkylation:[2] **1** (1 eq., 4 mmol, 841 mg) was suspended in acetone (10mL/mmol). 9-(Chloromethyl)anthracene (3 eq., 12 mmol, 2721 mg) and NaI (4 eq., 16 mmol, 2398 mg) were added and the suspension was refluxed overnight. The hot suspension was filtered, and the product was washed with acetone. Mass spectrometry revealed that some Cl^- salt remained in the product.

2-Ant (1,1'-(1,3-phenylene)bis(9-anthracenyl-1H-imidazol-3-ium))was obtained as a yellow solid (3.4 mmol, 2.9 g, 86%).

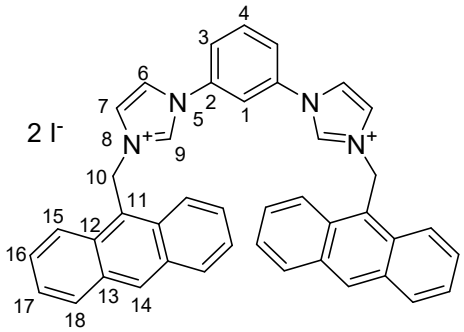

^{1}H NMR (700 MHz, DMSO-d_6): δ (ppm) = 9.90 (2H, H^9, s), 8.87 (2H, H^{14}, s) 8.49 (4H, H^{15}, d), 8.28 (2H, H^6, s), 8.24 (4H, H^{18}, d),

8.16 (1H, H^1, s), 7.93 (2H, H^3, dd), 7.86 (1H, H^4, t), 7.74 (2H, H^7, s), 7.69 (4H, H^{16}, t), 7.63 (4H, H^{17}, t), 6.57 (4H, H^{10}, s). **^{13}C NMR (176 MHz, DMSO-d6)): δ (ppm) =** 135.44 (2C, C^9, CH), 135.38 (2C, C^2, Cq), 131.6 (1C, C^4, CH), 131.1 (4C, C^{13}, Cq), 130.8 (4C, C^{12}, Cq), 130.4 (2C, C^{14}, CH), 129.4 (4C, C^{15}, CH), 127.8 (4C, C^{17}, CH), 125.6 (4C, C^{16}, CH), 123.4 (4C, C^{18}, CH), 123.3 (2C, C^7, CH), 123.2 (2C, C^3, CH), 122.7 (2C, C^{11}, Cq), 121.6 (2C, C^6, CH), 116.5 (1C, C^1, CH), 45.7 (2C, C^{10}, CH_2). **^{15}N NMR (71 MHz, DMSO-d6): δ (ppm) =** 188.2 (2N, N^8), 187.1 (2N, N^5).

ESI-MS ($[M-H]^+$ for $C_{42}H_{32}N_4^{2+}$): m/z 591.2532. Found: m/z 591.2549

Elemental analysis calculated for $C_{42}H_{32}N_4I_2$ + 1 H_2O: C, 58.35; H, 3.96; N, 6.48. found: C, 58.14; H, 4.06; N, 6.48

The complexes **C-R-side** were obtained utilizing a previously published synthetic route.[3] The reactions were carried out in a glovebox with an argon atmosphere in dry solvents. The corresponding proligand (2 eq.) was suspended in THF (20 mL), and Zr(NMe2)$_4$ (2.1 eq.) was added. The resulting suspension was stirred at room temperature for 16 h. $FeBr_2$ (1 eq.) was added to the resulting yellow suspension resulting in a quick color change to red (for **$[Fe((ImPh)_2P)_2]^+$**) or green (for **$[Fe((ImAnt)_2P)_2]^+$**). After stirring for another 24 hours the reaction was exposed to air and quenched with MeOH, resulting in green solutions with solid residue. The residue was filtered off, and the solvent was evaporated. The resulting brownish green solid was dissolved in DCM and filtered off, leaving a yellow residue. After concentrating the solution, it was passed over a silica gel column and thoroughly rinsed with DCM. By switching to MeCN, the green fraction containing the desired product was eluted. KPF_6 was added and the solution volume was reduced by evaporation. Addition of water led to the precipitation of the desired complex. The product was crystallized by diffusion of *n*-pentane into a DCM solution of the respective complex.

$[Fe((ImPh)_2P)_2]^+$ was obtained as green needles (0.08 mmol, 80 mg, 10.9%).

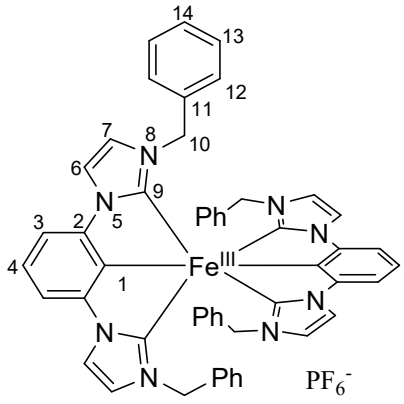

^{1}H NMR (700 MHz, DMSO-d_6): δ (ppm) = 25.17 (4H, H^3, s), 11.03 (8H, H^{10}, s), 6.62 (4H, H^{14}, t), 6.27 (8H, H^{13}, t), 3.73 (8H, H^{12}, d), 2.33 (4H, H^7, s), -2.75 (4H, H^6, s), -35.47 (2H, H^4, s). **^{13}C NMR (176 MHz, DMSO-d6) δ (ppm) =** 515.0 (4C, C^2, C_q), 477.2 (2C, C^4, CH), 149.8 (4C, C^{11}, C_q), 129.9 (8C, C^{13}, CH), 127.6 (4C, C^{14}, CH), 124.3 (8C, C^{12}, CH), 87.3 (4C, C^6, CH), 76.9 (4C, C^7, CH), 16.2 (4C, C^{10}, CH_2), -199.9 (4C, C^3, CH).

ESI-MS ($[M]^+$ for $C_{52}H_{42}FeN_8$): m/z 834.2876. Found: m/z 834.2872.

Elemental analysis calculated for $C_{52}H_{42}FeN_8PF_6$ + 0.5 H_2O: C, 63.17; H, 4.38; N, 11.33. found: C, 63.17; H, 4.62; N, 11.49

$[Fe((ImAnt)_2P)_2]^+$ was obtained as green needles (0.04 mmol, 66 mg, 4.2%).

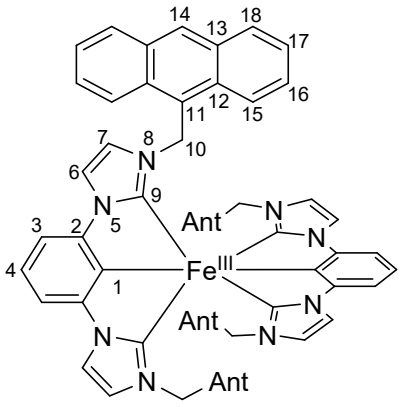

^{1}H NMR (700 MHz, DMSO-d_6): δ (ppm) = 24.77 (4H, H^3, s), 15.70 (8H, H^{10}, s), 8.17 (4H, H^{14}, s), 7.65 (8H, H^{18}, d), 6.78 (8H, H^{17}, t), 5.53 (8H, H^{16}, t), 3.53 (8H, H^{15}, d), 1.74 (4H, H^6, d), -2.85 (4H, H^7, s), -37.4 (2H, H^4, s). **^{13}C NMR (176 MHz, DMSO-d6) δ (ppm) =** 514.8 (4C, C^2, C_q), 483.1 (2C, C^4, CH), 131.2 (8C, C^{13}, C_q), 129.9 (8C, C^{12}, C_q), 129.4 (8C, C^{18}, CH), 127.1 (4C, C^{14}, C_q), 126.9 (8C, C^{16}, CH), 125.1 (8C, C^{17}, CH), 121.1 (8C, C^{15}, CH), 87.5 (4C, C^7,CH), 74.7 (4C, C^6,CH), 9.9 (4C,C^{10},CH_2), -203.3 (4C, C^3,CH).

ESI-MS ($[M]^+$ for $C_{84}H_{58}FeN_8^+$): m/z 1234.4128. Found: m/z 1234.4147.

Elemental analysis calculated for $C_{84}H_{58}FeN_8PF_6$ + 4 H_2O (Due to the inherent photoinstability decomposition products may be the origin of this deviation): C, 69.47; H, 4.58; N, 7.85. found: C, 69.73; H, 4.38; N, 7.77

During our studies we uncovered a photoinstability for **$[Fe((ImAnt)_2P)_2]^+$** as mentioned above. The complex decomposes slightly after excitation in the MLCT/chromophore band, i.e. at wavelengths below 450 nm, resulting in the release of anthracene species. This was first observed during fluorescence measurements, since the normally strongly quenched anthracene emission (compared to free anthracene) was growing with each measurement due to the release of the much more emissive anthracene species, see left panel of Figure S1. This effect is much less pronounced for the more relevant LMCT emission as the decomposed complex is no longer emissive which can be seen in the right panel of Figure S1. Nevertheless, it is difficult to keep the samples of **$[Fe((ImAnt)_2P)_2]^+$** completely clean. Therefore, for measurements on this complex, we always prepared fresh solutions, allowing sensitive analytical methods to remain viable. For the other complexes we didn't observe indications for a photoinstability.

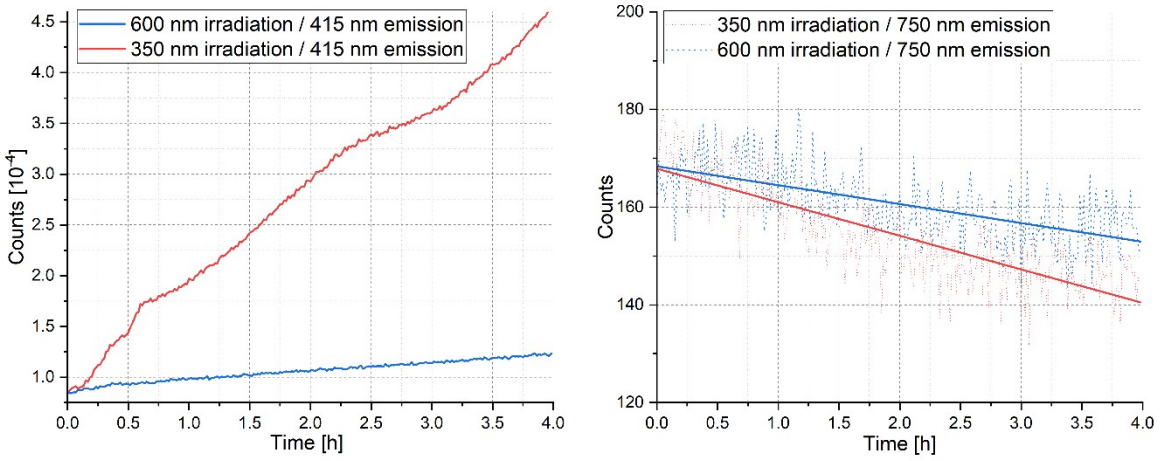

Figure S1: Decomposition study on **[Fe((ImAnt)$_2$P)$_2$]$^+$** with a concentration of 1⋅10-5 mol/l dissolved in MeCN. The samples were irradiated at 350 nm or 600 nm for 1 minute. Then the emission at 415 nm resulting from free antracene species and at 750 nm resulting from the LMCT state is measured after excitation at 350 nm. This sequence was repeated many times to monitor the evolution of the emission over a total irradiation time of four hours. Please note, that the sample irradiated at 600 nm was also irradiated at 350 nm for about 3 seconds per minute to measure the anthracene emission. To show the trend of the weak emission at 750, a linear regression was applied.

The proligand precursors **3-R** were synthesized applying a known synthetic procedure for the phenyl derivative, that was adjusted for the anthracenyl species.[4] 1,3,5-tribromobenzene (1 eq.) was suspended in Et_2O under Argon atmosphere and cooled to -78°C. n-Buthyllithium (n-BuLi) (2.5 mol/L in hexane, 1 eq.) was added slowly and the solution was stirred at this temperature for 45 min. The corresponding chromophore-benzaldehyde (1 eq.) was added, and the solution was stirred while reaching room temperature over 16h. Brine was added, and the mixture was stirred for 10 minutes. The organic phase was separated, and the aqueous phase extracted with Et_2O. After combination of the organic phases, they were dried over $MgSO_4$, and the solvent was reduced by evaporation. The resulting solid was dissolved in DCM under Argon atmosphere and Triethylsilane (4 eq.) was added. After cooling to 0°C BF_3OEt_2 (48 %, 1.5 eq.) was added slowly, and the solution was allowed to reach room temperature overnight under stirring. The mixture was quenched with aqueous $NaHCO_3$ until no bubbling was observed and the organic phase was separated. The aqueous phase was subsequently extracted with DCM, and the organic phases were combined. After drying over $MgSO_4$ and removal of solvent a crude product was obtained. Purification through column chromatography (SiO_2; Hexane/EtOAc 9:1) yielded the desired product.

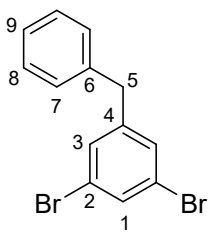

3-Ph (1-benzyl-3,5-dibromobenzene) was obtained as a colorless solid (12.3 mmol, 4.0 g, 61 %)

^{1}H NMR (700 MHz, DMSO-d$_6$): δ (ppm) = 7.63 (1H, H^1, t), 7.47 (2H, H^3, d), 7.30 (2H, H^8, t), 7.26 (2H, H^7, d), 7.20 (1H, H^9, t), 3.94 (2H, H^5, s). **^{13}C NMR (176 MHz, DMSO-**

d6) δ (ppm) = 146.3 (1C, C^4, C_q), 139.9 (1C, C^6, C_q), 131.0 (1C, C^1, CH), 130.6 (2C, C^3, CH), 128.7 (2C, C^7, CH), 128.6 (2C, C^8, CH), 126.4 (1C, C^9, CH), 122.4 (2C, C^2, C_q), 39.9 (1C, C^5,CH_2).

ESI-MS ([M+H]⁺ for $C_{13}H_{10}Br_2$): m/z 326.2902. Found: m/z 326.2936.

3-Ant (9-(3,5-dibromobenzyl)anthracene) was obtained as a pale yellow solid. (2.0 mmol, 830 mg, 9.74 %)

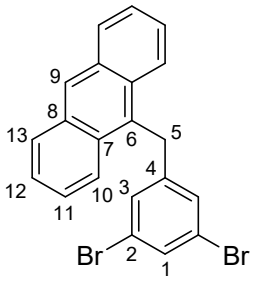

^{1}H NMR (700 MHz, DMSO-d_6): δ (ppm) = 8.63 (1H, H^9, s), 8.31 (2H, H^{13}, d), 8.14 (2H, H^{10}, d), 7.61 (1H, H^1, t), 7.57 (2H, H^{11}, ddd), 7.54 (2H, H^{12}, ddd), 7.28 (2H, H^3, d), 5.07 (2H, H^5, s). **^{13}C NMR (176 MHz, DMSO-d6) δ (ppm) =** 146.1 (1C, C^6, Cq), 131.2 (2C, C^7, Cq), 131.0 (1C, C^1, CH), 130.6 (2C, C^8, Cq), 129.9 (1C, C^4, Cq), 129.8 (2C, C^3, CH), 129.1 (2C, C^{10}, CH), 126.9 (1C, C^9, CH), 126.6 (2C, C^{11}, CH), 125.3 (2C, C^{12}, CH), 124.5 (2C, C^{13}, CH), 122.5 (2C, C^2, Cq), 31.5 (1C, C^5, CH_3)

EI-MS ([M]⁺ for $C_{21}H_{14}Br_2$): m/z 423.9462. Found: m/z 423.9446.

These precursors were then used in an Ullmann adjacent coupling reaction with imidazole to obtain the molecules **4-R**.[5] **3-R** (1 eq.), imidazole (3 eq.), K_2CO_3 (4 eq.) and CuI (0.2 eq.) were suspended in DMSO (2 mL/mmol). The suspension was heated to 150°C for 18 h. Afterwards, the suspension was concentrated under reduced pressure at 150°C until it solidified. The resulting solid was suspended in water and filtered. The residue was repeatedly rinsed with water until no further coloration was visible. The remaining residue was suspended in methanol and filtered. The resulting solution was evaporated under reduced pressure and the remaining solid was purified with column chromatography (SiO_2; CH_2Cl_2/MeOH 9:1).

4-Ph (1,1'-(5-benzyl-1,3-phenylene)bis(1H-imidazole)) was obtained as a colorless solid (0.46 mmol, 140 mg, 46.6%)

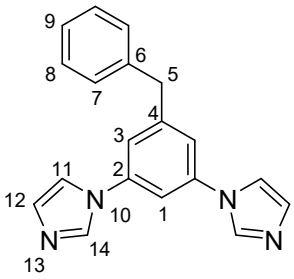

^{1}H NMR (700 MHz, DMSO-d_6): δ (ppm) = 8.38 (2H, H^{12}, s), 7.86 (2H, H^{11}, s), 7.82 (1H, H^1, t), 7.59 (2H, H^3, d), 7.36 (2H, H^7, d), 7.3 (2H, H^8, t), 7.2 (1H, H^9, tt), 7.13 (2H, H^{14}, s), 4.04 (2H, H^5, s). **^{13}C NMR (176 MHz, DMSO-d6) δ (ppm) =** 145.2 (1C, C^4, Cq), 140.4 (1C, C^6, Cq), 138.1 (2C, C^2, Cq), 135.8 (2C, C^{12}, CH), 130.0 (2C, C^{14}, CH), 128.7 (2C, C^7, CH), 128.5 (2C, C^8, CH), 126.2 (2C, C^9, CH), 118.5 (2C, C^3, CH), 118.1 (2C, C^{11}, CH), 109.7 (1C, C^1, CH), 40.9 (1C, C^5, CH_3). **^{15}N NMR (71 MHz, DMSO-d6): δ (ppm) =** 266.0 (2N, N^{13}), 184.4 (2N, N^{10}).

ESI-MS ([M+H]⁺ for $C_{19}H_{16}N_4$): m/z 301.1448. Found: m/z 301.1444.

4-Ant was obtained as a pale yellow solid (4.0 mmol, 1.6 g, 33.3 %)

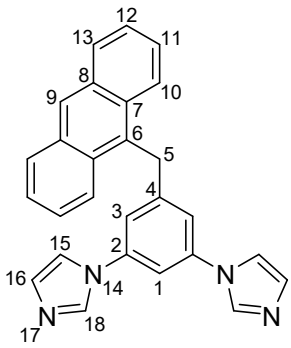

^{1}H NMR (700 MHz, DMSO-d$_6$): δ (ppm) = 8.61 (1H, H^{9}, s), 8.46 (2H, H^{13}, d), 8.17 (2H, H^{16}, s), 8.13 (2H, H^{10}, d), 7.75 (1H, H^{1}, t), 7.59 (4H, H^{12} u H^{15}, m), 7.54 (2H, H^{11}, t), 7.39 (2H, H^{3}, d), 7.06 (2H, H^{18}, d), 5.15 (2H, H^{5}, s). **^{13}C NMR (176 MHz, DMSO-d6) δ (ppm) =** 145.2 (1C, C^{6}, Cq), 138.0 (2C, C^{2}, Cq), 135.6 (2C, C^{16}, CH), 131.2 (2C, C^{7}, Cq), 131.1 (2C, C^{8}, Cq), 130.0 (2C, C^{18}, CH), 129.9 (1C, C^{4}, Cq), 129.1 (2C, C^{10}, CH), 126.9 (1C, C^{9}, CH), 126.5 (2C, C^{12}, CH), 125.2 (2C, C^{11}, CH), 124.6 (2C, C^{13}, CH), 118.04 (2C, C^{3}, CH), 117.99 (2C, C^{15}, CH), 110.6 (1C, C^{1}, CH), 32.3 (1C, C^{5}, CH$_2$). **^{15}N NMR (71 MHz, DMSO-d6): δ (ppm) =** 266.5 (2N, N^{17}), 184.0 (2N, N^{14}).

ESI-MS ([M+H]$^{+}$ for $C_{27}H_{20}N_4$): m/z 401.1761. Found: m/z 401.1768.

The proligands **5-R** were obtained by methylation.[6] The matching **4-R** (1 eq.) is suspended in MeCN (10 mL/mmol). Methyliodide (4 eq.) was added, and the mixture was refluxed overnight. After cooling down the acetonitrile was filtered off, and the remaining crude product was washed with acetone.

5-Ph was obtained as colorless crystalline powder (0.23 mmol, 135 mg, 49.7 %)

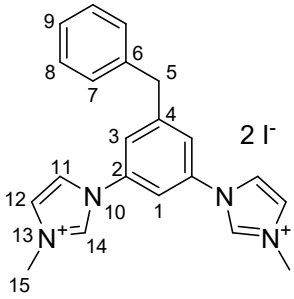

^{1}H NMR (700 MHz, DMSO-d$_6$): δ (ppm) = 9.87 (2H, H^{14}, s), 8.35 (2H, H^{12}, t), 8.16 (1H, H^{1}, t), 8.01 (2H, H^{11}, t), 7.98 (2H, H^{3}, d), 7.37 (2H, H^{7}, d), 7.33 (2H, H^{8}, t), 7.24 (1H, H^{9}, tt), 4.15 (2H, H^{5}, s), 3.98 (6H, H^{15}, s). **^{13}C NMR (176 MHz, DMSO-d6) δ (ppm) =** 145.9 (1C, C^{6}, Cq), 139.5 (1C, C^{4}, Cq), 136.3 (2C, C^{14}, CH), 135.8 (2C, C^{2}, Cq), 128.72 (2C, C^{7}, CH), 128.67 (2C, C^{8}, CH), 126.6 (1C, C^{9}, CH), 124.7 (2C, C^{11}, CH), 122.7 (2C, C^{3}, CH), 120.8 (2C, C^{12}, CH), 113.3 (1C, C^{1}, CH), 40.7 (1C, C^{5}, CH$_2$), 36.4 (2C, C^{15}, CH$_3$). **^{15}N NMR (71 MHz, DMSO-d6): δ (ppm) =** 186.5 (2N, N^{13}), 175.2 (2N, N^{10}).

ESI-MS ([M]$^{2+}$ for $C_{29}H_{26}N_4^{2+}$): m/z 165.0917. Found: m/z 165.095.

Elemental analysis calculated for $C_{21}H_{22}N_4I_2$ + 0.1 H_2O: C, 43.04; H, 3.82; N, 9.56. found: C, 42.67; H, 4.15; N, 9.64

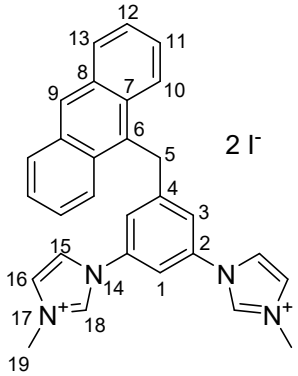

5-Ant was obtained as a faint yellow solid (0.15 mmol, 104 mg, 60.6 %)

^{1}H NMR (700 MHz, DMSO-d$_6$): δ (ppm) = 9.63 (2H, H^{18}, s), 8.67 (1H, H^{9}, s), 8.36 (2H, H^{10}, d, J = 8.6 Hz), 8.19 (2H, H^{16}, t, J = 1.9 Hz), 8.16 (2H, H^{13}, d, J = 8.0 Hz), 8.05 (1H, H^{1}, s), 7.93 (2H, H^{15}, t, J = 18 Hz), 7.73 (2H, H^{3}, d, J = 2.0 Hz), 7.60-7.53 (4H, H$^{1!}$ and H^{12}, m), 5.22 (2H, H^{5}, s), 3.91 (6H, H^{19}, s). **^{13}C NMR (176**

MHz, DMSO-d6) δ (ppm) = 146.4 (1C, C^6, Cq), 136.3 (2C, C^{18}, CH), 135.8 (2C, C^2, Cq), 131.3 (2C, C^8, Cq), 130.1 (2C, C^7, Cq), 129.8 (1C, C^4,Cq), 129.2 (2C, C^{13}, CH), 127.3 (1C, C^9, CH), 126.7 and 125.3 (4C, C^{11} and C^{12}, CH), 124.7 (2C, C^{15}, CH), 124.4 (2C, C^{10}, CH), 122.3 (2C, C^3, CH), 121.1 (2C, C^{16}, CH), 114.5 (1C, C^1, CH), 36.3 (1C, C^5, CH_2), 32.8 (2C, C^{19}, CH_3). **^{15}N NMR (71 MHz, DMSO-d6): δ (ppm) =** 186.5 (2N, N^{14}), 175.2 (2N, N^{17}).

ESI-MS ([M]$^{2+}$ for $C_{29}H_{26}N_4^{2+}$): m/z 215.1073. Found: m/z 215.108.

Elemental analysis calculated for $C_{29}H_{26}N_4I_2$ + 0.5 H_2O: C, 50.24; H, 3.93; N, 8.08. found: C, 49.87; H, 4.20; N, 8.25

The complexes **C-R-backbone** were synthesized based on a modified procedure previously established for heteroleptic complexes of Fe^{II}.[7] In a glove box with Argon atmosphere, the corresponding proligand was dissolved in THF and cooled to -25°C. Lithium-bis-trimethylsilylamide was added and the solution was stirred for 2h at this temperature. Iron-(bis-bis-trimethylsilylamide) was dissolved in THF, added to the prepared ligand solution and the combined solution was allowed to reach room temperature overnight. The resulting suspension was removed from the glove box and additionally quenched with methanol to obtain a green suspension, which was filtered. After removal of the solvent under reduced pressure the remaining solid was dissolved in DCM and filtered off again before it was concentrated and added to a silica column. After elution of impurities with DCM, the product was recovered from the column with MeCN. The obtained green solution again concentrated before adding KPF_6. After addition of water the desired product precipitated as a green PF_6^- salt. The product was filtered off and then dissolved in DCM to obtain crystals by diffusion of pentane. In addition, **[Fe(Im$_2$PAnt)$_2$]$^+$** shows photoinstability to a certain degree, as discussed below.

[Fe(Im$_2$PPh)$_2$]$^+$ was obtained as green plates (0.75 mmol, 80 mg, 10.9%)

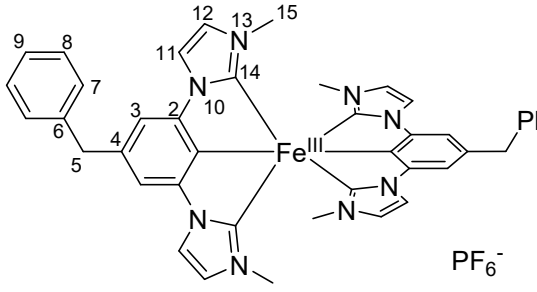

^{1}H NMR (700 MHz, DMSO-d$_6$): δ (ppm) = 49.33 (2H, H^5, s) 25.45 (4H, H^3, s), 9.64 (12H, H^{15}, s), 9.52 (4H, H^7, d, J = 7.8 Hz), 8.89 (4H, H^8, t, J = 7.6 Hz), 7.79 (2H, H^9, t, J = 7.4 Hz), 2.81 (4H, H^{12}, s), -2.64 (2H, H^{11}, s). **^{13}C NMR (176 MHz, DMSO-d6) δ (ppm) =** 528.9 (2C, C^2, Cq), 520.5 (1C, C^4, Cq), 321.9 (2C, C^6, Cq), 132.1 (2C, C^8, CH), 131.0 (1C, C^9, CH), 128.6 (2C, C^7, CH), 89.6 (2C, C^{11}, CH), 77.4 (2C, C^{12}, CH), 1.2 (2C, C^{15}, CH_3), -72.9 (1C, C^5, CH_2), -212.5 (2C, C^3, CH).

ESI-MS ([M]$^+$ for $C_{42}H_{38}FeN_8^+$): m/z 710.2563. Found: m/z 710.2568.

Elemental analysis calculated for $C_{42}H_{38}FeN_8PF_6$ + 1.5 H_2O: C, 57.15; H, 4.68; N, 12.70. found: C, 57.19; H, 4.93; N, 12.61

$[Fe(Im_2PAnt)_2]^+$ was obtained as a green solid (0.5 mmol, 37 mg, 4.7%)

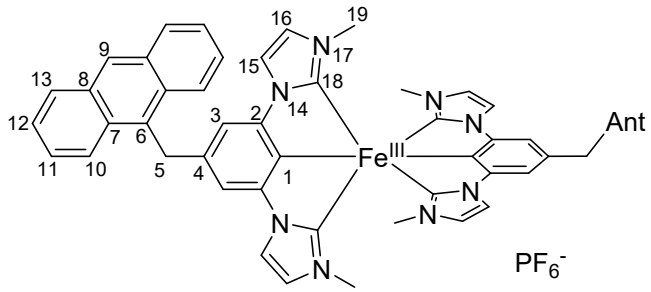

^{1}H NMR (700 MHz, DMSO-d_6): δ (ppm) = 25.23 (4H, H^3, s) 11.71 (4H, H^{10}, d, J = 9.2 Hz), 9.55 (12H, H^{19}, s), 9.26 (2H, H^9, s), 8.78 (4H, H^4, d, J = 8.9 Hz), 8.49 (4H, H^{11}, dd, J = 9.3, 6.5 Hz), 8.00 (4H, H^{12}, dd, J = 8.8, 6.5 Hz), 2.49 (4H, H^{16}, s), -3.08 (4H, H^{15}, s). **^{13}C NMR (176ki MHz, DMSO-d6) δ (ppm) =** 535.0 (4C, C^2, Cq), 517.6 (2C, C^4, Cq), 196.7 (2C, C^6, Cq), 135.7 (4C, C^7, C_q), 130.6 (4C, C^{13}, CH), 130.2 (4C,C^8, Cq), 130.0 (4C, C^{10}, CH),k 128.0 (4C, C^{11}, Cq), 127.7 (2C, C^9, CH), 126.9 (4C, C^{12}, CH), 88.0 (4C, C^{15}, CH), 76.4 (4C, C^{16}, CH), 1.96 (4C, C^{19}, CH_3), -83.9 (2C, C^5, CH_2), -216.1 (4C, C^3, CH).

ESI-MS ($[M]^+$ for $C_{58}H_{46}FeN_8^+$): m/z 910.3189. Found: m/z 910.3182.

Elemental analysis calculated for $C_{58}H_{46}FeN_8PF_6$ + 1.5 H_2O: C, 64.33; H, 4.56; N, 10.35. found: C, 64.23; H, 4.76; N, 10.26

Experimental Methods

Cyclic Voltammetry

Potentiostatic measurements were performed at room temperature using a PGSTAT 101 potentiostat from Metrohm in dry and degassed 0.1 M [*n*-Bu_4N][PF_6] MeCN solution with an analyte concentration of 10^{-3} M. A platinum working electrode (1 mm diameter), an Ag/$AgNO_3$ reference electrode and a platinum pin electrode were utilized in a three-electrode configuration. After measurements, Ferrocene was added as an internal standard to reference against the $FcH^{0/+}$ redox couple. The resulting voltammograms were analyzed using the *NOVA 2.1.3* software. The reversibility of redox couples was investigated with the criteria proposed by Nicholson and Shain, and the Randles-Sevcik equation.[8]

UV/VIS Spectroscopy

Spectroscopic-grade solvents from VWR in quartz cuvettes by Hellma with an optical path length of 10 mm were used. Absorption spectra were recorded at concentrations of 10^{-5} M in 99.9% pure acetonitrile with a PerkinElmer Lambda465 single-beam spectrophotometer.

Luminescence Measurements

The emission and excitation spectra were recorded with an Edinburgh Instruments FLS1000 spectrometer with single monochromators and a red-extended PMT-980 detector. The samples were dissolved in MeCN at a concentration of $1*10^{-5}$ mol/L. and degassed by bubbling argon through.

Time-Correlated Single Photon Counting

Time-Correlated Single Photon Counting (TCSPC) was done using an Ultima 01-DD TCSPC system (HORIBA Jobin Yvon). The degassed sample solution was excited at 374 nm with a HORIBA DD375L laser diode with a maximum repetition rate of 100 MHz. The emission was recorded with an emission monochromator which was set to 415 nm. A histogram of photons was recorded as a function of 16,383 channels on a time range of 100 ns (0.012 ns per channel) until one channel reached 10000 counts. In addition, a scattering solution was measured to characterize the prompt response.

Time-Resolved Emission Measurements

Time-resolved emission measurements were carried out by means of a streak camera system (Streakscope C10627, Hamamatsu Photonics) and applying ultrashort excitation pulses at 350 nm. The latter were generated by frequency doubling the output of a noncollinear optical parametrical amplifier (NOPA) tuned to a center wavelength of 700 nm. The NOPA is pumped by a regenerative Ti:sapphire amplifier system (CPA 2001, CLARK MXR, INC.) operating at a center wavelength of 775 nm and a repetition rate of 1 kHz. MeCN solutions of the compounds were prepared under argon and measured in 1 cm thick fused silica cuvettes. All samples were prepared with an optical density of about 0.1 at the excitation wavelength to avoid signal distortions due to self-absorption. To determine the emission lifetime, the time and wavelength resolved emission was integrated over its spectrum and the resulting decay curve fitted by a monoexponential decay function.

Transient Absorption Spectroscopy

Transient absorption (TA) spectra were recorded with a time resolution of about 100 fs employing a pump-probe setup in which a white light continuum is used for probing and a NOPA for the generation of the excitation pulses.[9] Both, the NOPA and the white light stage are pumped by the regenerative Ti:sapphire laser system (CPA 2001, CLARK MXR, INC.) used also for the measurements with the streak camera. The white light continuum is generated by focusing a small fraction of the near infrared pump light into a moving CaF_2 crystal. To excite the compounds at their lowest absorption band, the NOPA was tuned to a center wavelength of 600 nm. The dispersion of the NOPA output was minimized by a compressor based on fused silica prisms resulting in excitation pulses with a length of about 30 fs. The excitation energy was chosen as low as possible to reduce the probability for photodegradation and was approx. 200 nJ in all measurements. Excitation and probe beam were focused onto the sample to

overlapping spots with diameters of approximately 200 µm and 140 µm, respectively. Behind the sample, the probe was dispersed by a prism and transient absorption changes were spectrally resolved recorded by a photodiode array detector. The chirp of the white light probe was corrected in the evaluated TA spectra. To exclude effects caused by orientational relaxation, the polarizations of the pump and probe pulses were set to magic angle with respect to each other. For the TA measurements, the compounds were dissolved in MeCN and the sample solutions filled into 2 mm thick fused silica cuvettes. The optical density (OD) varied depending on the sample solution and was in the range of 0.13 - 0.2 at the excitation wavelength. The variation was necessary to minimize signal contribution due to scattering of the excitation light.

Quantum-Chemical Calculations of Absorption Spectra

Quantum chemical calculations employing Density Functional Theory (DFT) were carried out using the ORCA quantum chemistry package (version 5.0.3).[10] Geometry optimizations were performed with the PBEh-3c composite method,[11] applying very tight convergence criteria and tight optimization parameters. Frequency calculations confirmed the optimized structures as minima by verifying the absence of imaginary frequencies. The optimized geometries align well with the experimental crystal structures (see Supporting Information, Fig. X) and were used as input for further calculations.)

Absorption spectra were calculated using the linear-response time-dependent density functional theory (TD-DFT) by calculating the vertical electronic singlet-transitions, employing the B3LYP functional[12] in combination with the triple-zeta valence basis set def2-TZVP[13] and the D4 dispersion correction.[14] For comparison with experimental UV/Vis spectra, calculated transitions were shifted by -5000 cm^{-1} for all complexes to account for the well-known systematic overestimations of excitation energies by TD-DFT using hybrid functionals such as B3LYP, particularly for transition-metal complexes.[15] The analysis of the character of the excited states was done using the TheoDORE package.[16] The visualization of spin-density plots was performed with Avogadro version 1.2.0 using an isovalue of 0.0001, while the orbital visualizations were created with IboView v20211019.[17]

NMR-Spectroscopy

NMR spectra were recorded on a Bruker Ascent 700 spectrometer. Chemical shifts are expressed in parts per million (ppm, δ) downfield from tetramethyl silane (TMS). The spectra were referenced to the residual proton signals of the respective deuterated solvent or the solvent carbons respectively. The ^{15}N-HMBC spectra were referenced externally against liquid ammonia. The spectra were analyzed according to first order. Exact assignment of signals was done under consideration of ^{1}H–^{1}H-COSY, ^{1}H–^{13}C-HMQC, ^{1}H^{13}C- HMBC, ^{1}H–^{15}N-HMBC, ^{1}H–^{1}H-NOESY and DEPT135 spectra. For the paramagnetic ^{13}C-NMR spectra no proton decoupling was applied leading to multiplets in ^{13}C-NMR spectra.

2. Single Crystal X-ray diffraction

Despite several attempts, it was not possible to obtain single crystals of the four presented complexes suitable for publication. Due to the high flexibility of the phenyl and anthracene substituents the obtained structures are highly disordered leading to high R_{int} values and could therefore not be modelled precisely. Nevertheless, in case of **[Fe(Im$_2$PPh)$_2$]$^+$** blue crystals and **[Fe(Im$_2$PAnt)$_2$]$^+$** green crystals could be isolated and measured leading to pictures of the complexes demonstrating their connectivities (see Figure S11). In accordance with the calculated structures, **[Fe(Im$_2$PPh)$_2$]$^+$** and **[Fe(Im$_2$PAnt)$_2$]$^+$** both allow the estimation of a distorted octahedral coordination of the iron center and a misalignment of the chromophores with the ligand system due to the methyl bridge.

Figure S2: Connectivities of **[Fe(Im$_2$PPh)$_2$]$^+$** and **[Fe(Im$_2$PAnt)$_2$]$^+$** obtained by single crystal X-ray diffraction. Due to low single crystal quality, it was not possible to obtain more detailed structure.

3. NMR investigation of electronic decoupling

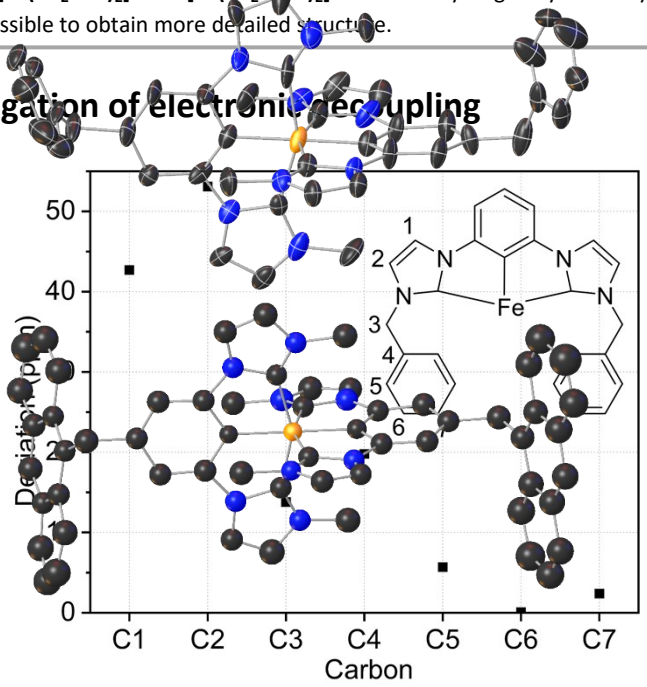

Figure S3: Absolute deviation from the expected chemical shift in ^{13}C-NMR spectroscopy. The imidazole carbons C1 and C2 and sidegroup carbons C4 to C7 for the **[Fe((ImPh)$_2$P)$_2$]$^+$** is referenced against an expected value of 130 ppm.[18] In addition, the aliphatic bridging carbon C3 is referenced against 30 ppm.[18]

4. Linear Combination of absorption spectra

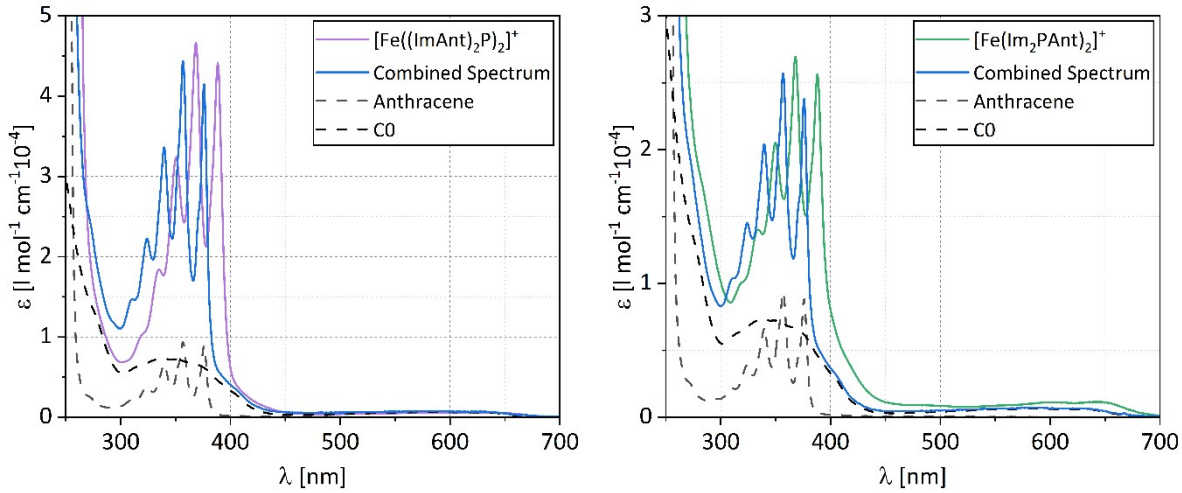

Figure S4: Linear combination of the absorption spectra of base complex C0 and free anthracene compared to the complexes **[Fe((ImAnt$_2$)P)$_2$]$^+$** (left) and **[Fe(Im$_2$PAnt)$_2$]$^+$** (right). The anthracene spectrum was multiplied by 2 or 4 to align with the number of chromophore units in the corresponding complex.

The comparison of the linear combination of the base complex C0 and anthracene with the anthracene substituted complexes (Figure S4) reveals a high similarity, suggesting a decoupling of both moieties. A coupled organic system would lead to excitations delocalized over the entire ligand structure leading to a strong redshift.

5. Steady State Emission

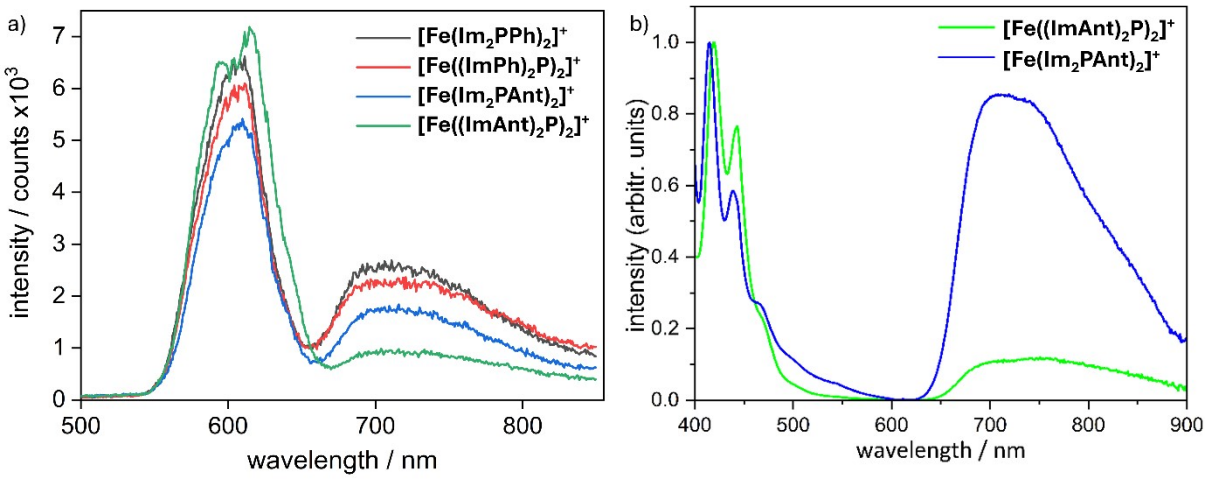

Figure S5: a) Emission spectra of the investigated complexes dissolved in MeCN at an optical density of 0.1 at the excitation wavelength of 600 nm. The emission peak at 600 nm results from scattering of the excitation light source. b) Normalized emission spectra of the investigated anthracene complexes excited at 350 nm. The singlet anthracene emission, most likely originating from an anthracene impurity is clearly stronger in **[Fe((ImAnt)$_2$P)$_2$]$^+$**. Both spectra were measured in MeCN (10^{-5} M).

From the not normalized emission spectra (Figure S5, Panel a) the weaker emission intensity of the anthracene substituted complexes is evident. **[Fe((ImAnt)$_2$P)$_2$]$^+$** exhibits an especially weakened emission, which may be influenced by the increased amount of anthracene moieties. The singlet

emission shown in Panel b) is much stronger in relation to the LMCT emission for **[Fe((ImAnt)$_2$P)$_2$]$^+$**, most likely due to its photo instability, resulting in a higher concentration of dissociated anthracene species.

6. Variable Temperature Emission Spectroscopy

The four chromophore-appended complexes were investigated in the temperature range of 77 K to 297 K in 20 K steps. The results are depicted in Figure S6. All complexes show an increase in general emission intensity at 77 K due to reduced vibrational relaxation, as is expected for lower temperatures. However, an increased solvent background at lower temperatures increases apparent emission intensities additionally. This effect is especially strong for the anthracene substituted complexes due to the weaker emission at 77 K. For the phenyl-substituted complexes, the broad emission bands between 650 and 900 nm are boosted significantly by about one order of magnitude. This behaviour is expected, since there is no low-lying chromophore state to quench the LMCT state and nonradiative decay is reduced at low temperatures. In addition to the general increase, the broadening of the spectra decreases, and two distinct peaks of the vibronic progression become visible for the C-Ph complexes. This was previously observed for the directly conjugated phenyl complex **Fe[(ImP-Ph)2]$^+$**.[19] This behaviour is also observed for **[Fe(Im$_2$PAnt)$_2$]$^+$**, however, the increase in intensity is only half of that in the C-Ph complexes, suggesting an influence of the anthracene substitution. Due to the 3anthracene state being lower in energy than the emissive 2LMCT state it can function as an efficient quenching channel, since no sufficient thermal energy for a back transfer to the 2LMCT state is available. This effect partially compensates for the decreased nonradiative decay, resulting in an overall increase in emission intensity. For **[Fe((ImAnt)$_2$P)$_2$]$^+$**, a faster 2LMCT to 3anthracene transition rate, as is evident in transient absorption spectroscopy, leads to an even stronger quenching, now almost fully offsetting the reduced nonradiative decay, reducing the intensity increase to a factor of 2 , which is almost fully masked by the rising baseline. For the phenyl complexes and **[Fe(Im$_2$PAnt)$_2$]$^+$**, the emission intensity generally rises with decreasing temperature as can be seen in Figure S6. This trend is interrupted around the freezing point of butyronitrile at 161.3 K, with the intensity dropping slightly after freezing. Only for **[Fe((ImAnt)$_2$P)$_2$]$^+$** this trend is not consistent. Here the strongest emission is recorded at 177 K. This may be due to the backtransfer being fully inhibited below this temperature. However, this may also just be an effect of the baseline which is also stronger at these temperatures and/or due to scattering.

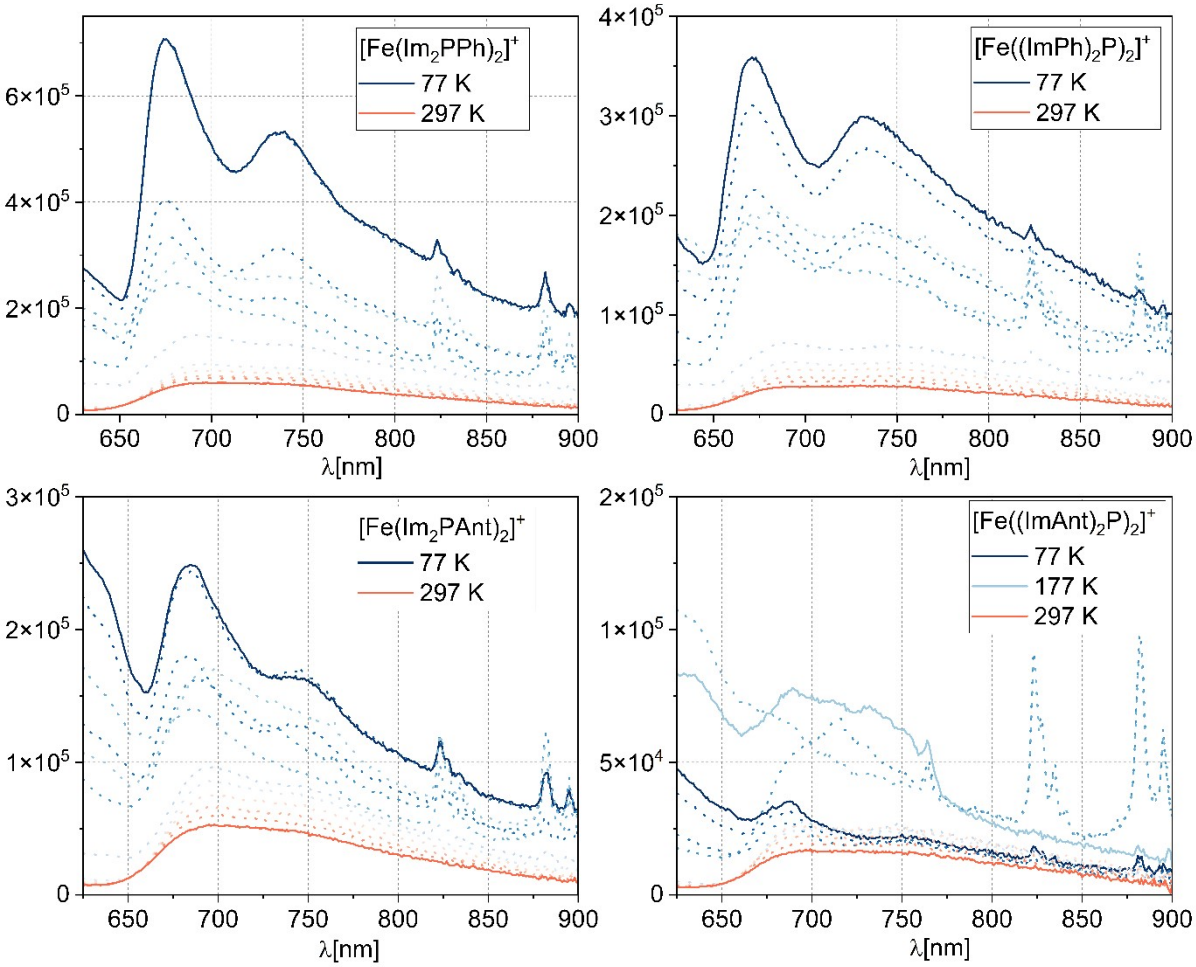

Figure S6: Variable temperature emission spectra in BuCN at 10^{-4} mol/L. Emission intensity in counts is plotted against the wavelength. Measurements were done in 20 K steps. The highest and lowest temperatures are highlighted (77 K and 297 K). For **$[Fe((ImAnt)_2P)_2]^+$** the 197 K spectrum is also highlighted as it is the lowest temperature that still shows a clear fluorescence in the LMCT range. The spectra are further discussed in the manuscript.

7. Time-Resolved Emission Measurements

Streak Camera Measurements

The following figures present the results of time-resolved emission measurements on the complexes dissolved in MeCN which were conducted by means of a streak camera system.

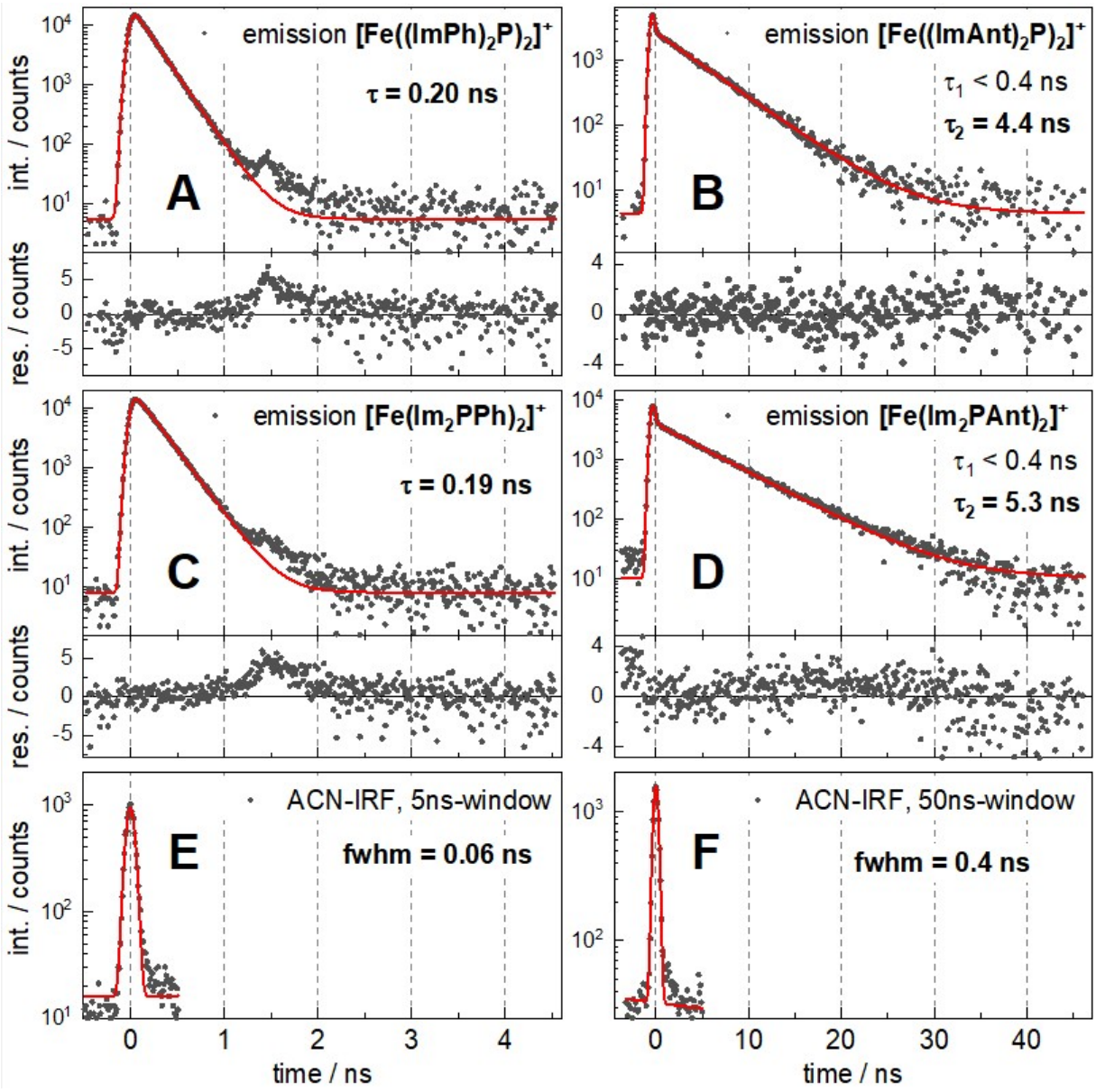

Figure S7: Time traces of the spectrally integrated emission intensity (int., black dots) for the four complexes **[Fe((ImPh)$_2$P)$_2$]$^+$** (A), **[Fe((ImAnt)$_2$P)$_2$]$^+$** (B), **[Fe(Im$_2$PPh)$_2$]$^+$** (C) and **[Fe(Im$_2$PAnt)$_2$]$^+$** (D) dissolved in MeCN as well as the respective exponential fits (red lines) and the corresponding residuals (res., lower graphs). The time constants obtained by the fitting procedure are given in the graphs E and F: Instrument response function (IRF) of the streak camera recorded in pure MeCN and fitted with a Gauss-function. The resulting full width at half maximum (fwhm) represents the time resolution for the time window of the measurement. All samples were excited at 600 nm.

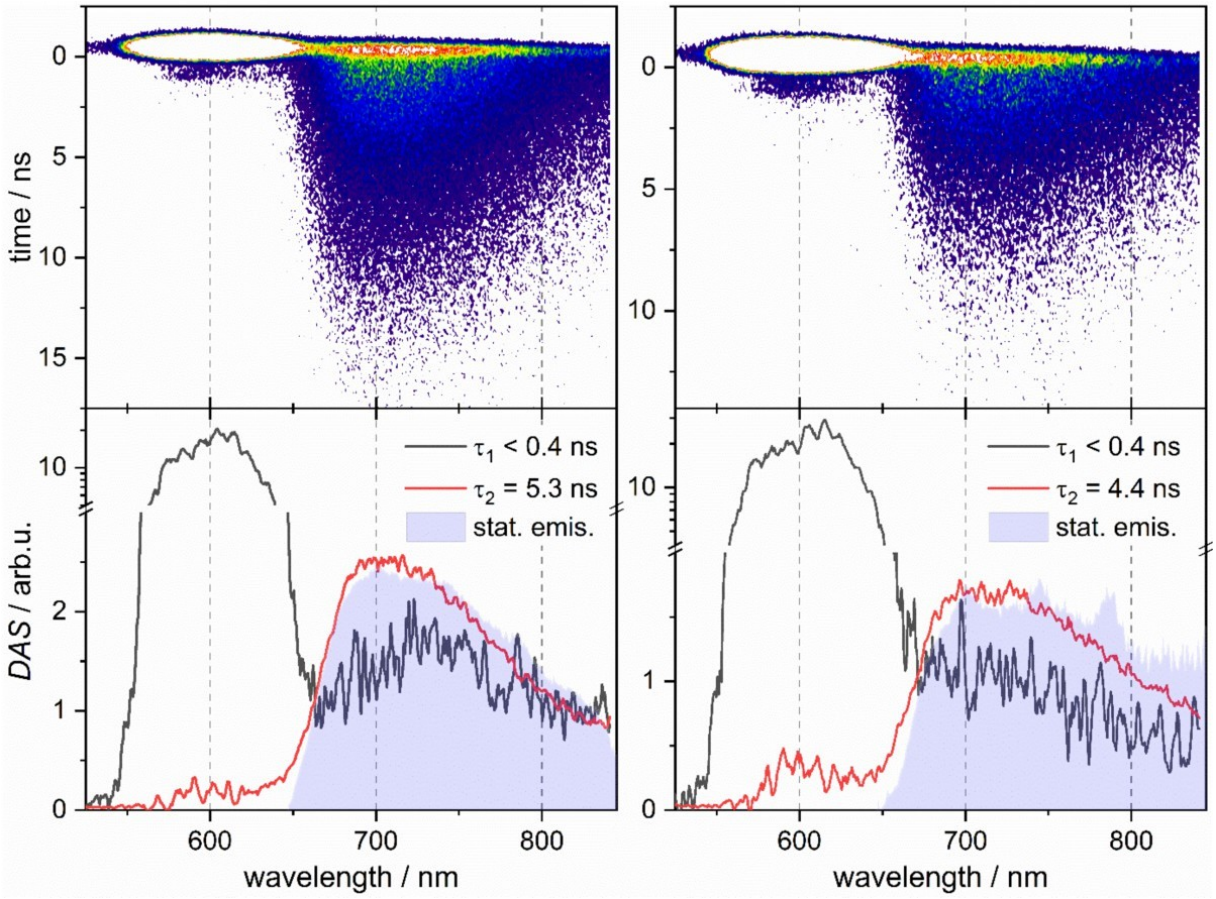

Figure S8: Time-resolved emission of **$[Fe(Im_2PAnt)_2]^+$** (left) and **$[Fe((ImAnt)_2P)_2]^+$** (right) dissolved in MeCN after optical excitation at 600 nm. Top: Two-dimensional plot of the time-resolved emission intensity (color coded). Bottom: Decay associated amplitude spectra (DAS) resulting from a GLA of the datasets with two exponential decay components and labelled by the respective time constants. For comparison also the stationary emission-spectrum is shown (gray area). The y-axis has a logarithmic scale above a break at 3 arb.u. so that the strong scattered light can be shown. The short time constant of the fit is below the time resolution of the measurement, and the corresponding signal contribution can be regarded as practically instantaneous.

TCSPC Measurements

The LMCT emission of **[Fe(Im$_2$PAnt)$_2$]$^+$** was also investigated by time correlated single photon counting (TCSPC). It shows the kinetics of LMCT emission after optical excitation at 374 nm, i.e. in the MLCT/anthracene absorption band, by a pulsed laser diode. A strong signal due to scattering of the excitation light appears at the doubled excitation wavelength because of second order diffraction in the monochromator. The data was fitted with a biexponential function. A fast decay component with a lifetime shorter than the time-resolution of the TCSPC setup is assumed to originate from scattered excitation light. A second decay component exhibits a lifetime of 5.8 ns. It is assigned to the LMCT emission. To support the assignment time-resolved emission spectra were recorded and evaluated by a GLA. The obtained DAS are shown in Figure S9. The DAS of the decay component with a lifetime of about 6 ns fits well to the LMCT emission, whereas the fast decay component appears indeed at the doubled excitation wavelength. Thus, the TCSPC measurements are within the experimental accuracy in perfect agreement with the results obtained by the streak camera.

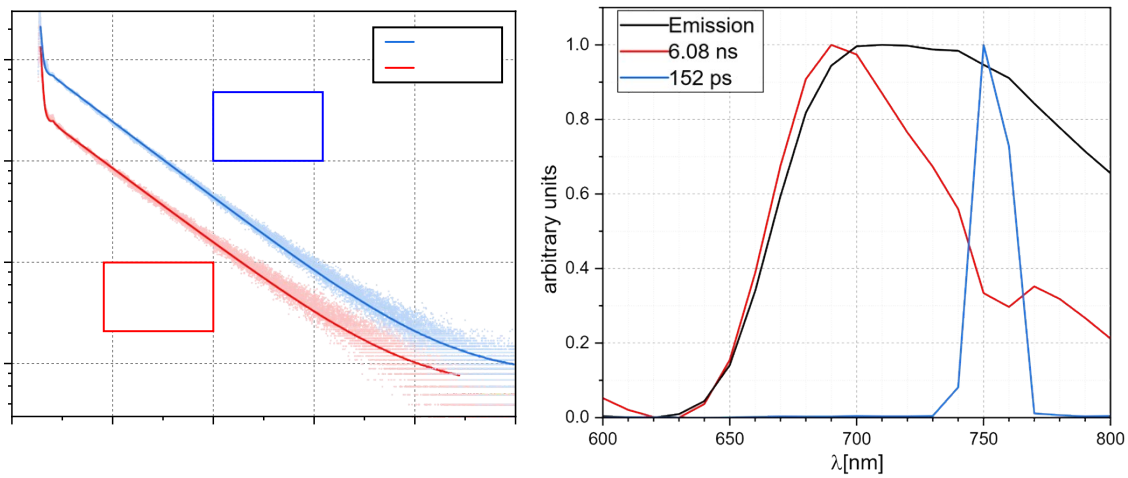

Figure S9: Left panel: Kinetics of the emission of **[Fe(Im$_2$PAnt)$_2$]$^+$** dissolved in MeCN at a concentration of 1*10^{-5} mol/l, measured by TCSPC at two detection wavelengths. The excitation was carried out at 374 nm; Emission up to 30000 counts was measured at 680 nm and 800 nm. The emission maximum at 710 nm was avoided to prevent interference with the second order diffraction of the excitation light (at 750 nm). Right panel: DAS of a GLA applied to spectrally resolved TCSPC data of the same solution recorded in 10 nm steps. The sharp peak at 750 nm and the corresponding lifetime is only due to second order diffraction of scattered excitation light.

Unfortunately, similar experiments with **[Fe((ImAnt)$_2$P)$_2$]$^+$** turned out to be problematic, since no laser diode emitting above 400 nm was in our TCSPC setup and the complex exhibiting photo instability after excitation at wavelengths below 450 nm. However, as the streak camera and the TA experiments show, the photodynamics of both anthracenyl substituted complexes are very similar.

8. Femtosecond Transient-Absorption Spectroscopy

The TA data $\Delta OD(\lambda,t)$ was globally analysed by fitting a sum of exponential decay components to the transient spectra using the following fit function:

$$\Delta OD(\lambda,t) = \sum_i A_i(\lambda) \cdot exp(-\frac{t}{\tau_i})$$

The i-th decay component is characterized by its time constant τ_i and the decay associated amplitude spectrum (DAS) $A_i(\lambda)$.

The following figures present the results of the ultrafast TA measurements on the four complexes **[Fe(Im$_2$PPh)$_2$]$^+$**, **[Fe((ImPh)$_2$P)$_2$]$^+$**, **[Fe(Im$_2$PAnt)$_2$]$^+$** and **[Fe((ImAnt)$_2$P)$_2$]$^+$**.

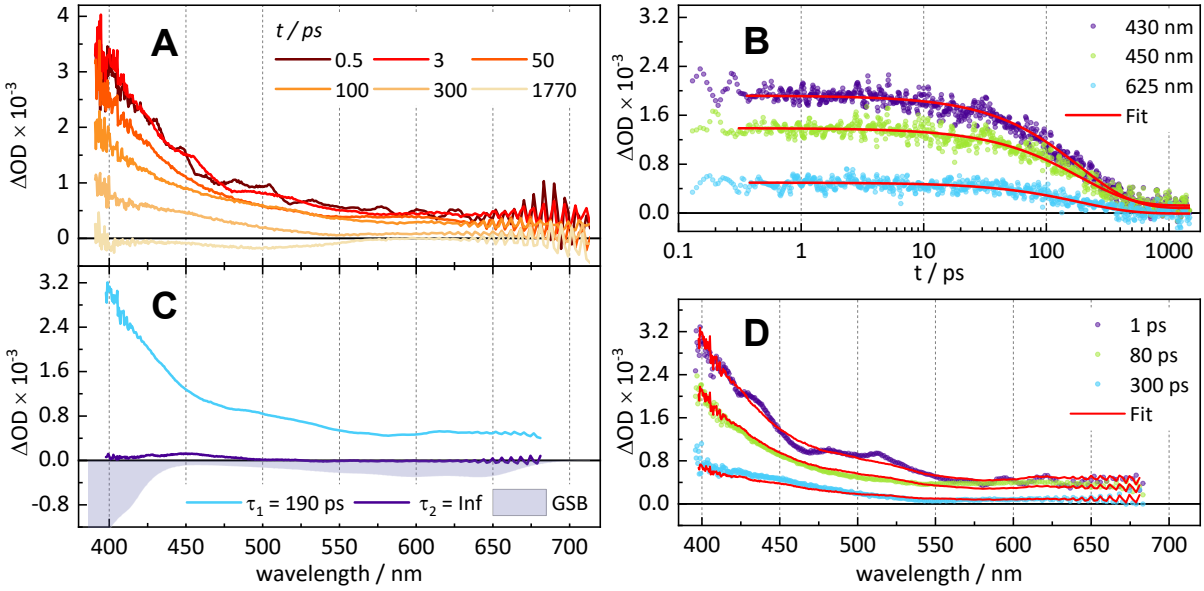

Figure S10, A: TA spectra of **[Fe(Im$_2$PPh)$_2$]$^+$** dissolved in MeCN at different times t after optical excitation at 600 nm. B: Time traces (dots) at the specified probe wavelengths together with respective fit curves resulting from the GLA (red solid lines). C: DAS obtained by the GLA and labelled by the respective time constants. The dynamics is well described by a monoexponential decay with the time constant τ_1 = 190 ps. A further, long-lived component modelled by a decay with an infinite time constant τ_2 = Inf was used to account for tiny offsets at long delay times. The component is at all wavelengths practically zero and within the experimental accuracy insignificant. The negative of the ground state absorption is shown as grey area to indicate where ground state bleach (GSB) might contribute to the TA signal. D: TA spectra (dots) at the given time points together with fitted spectra obtained by the GLA (red solid lines).

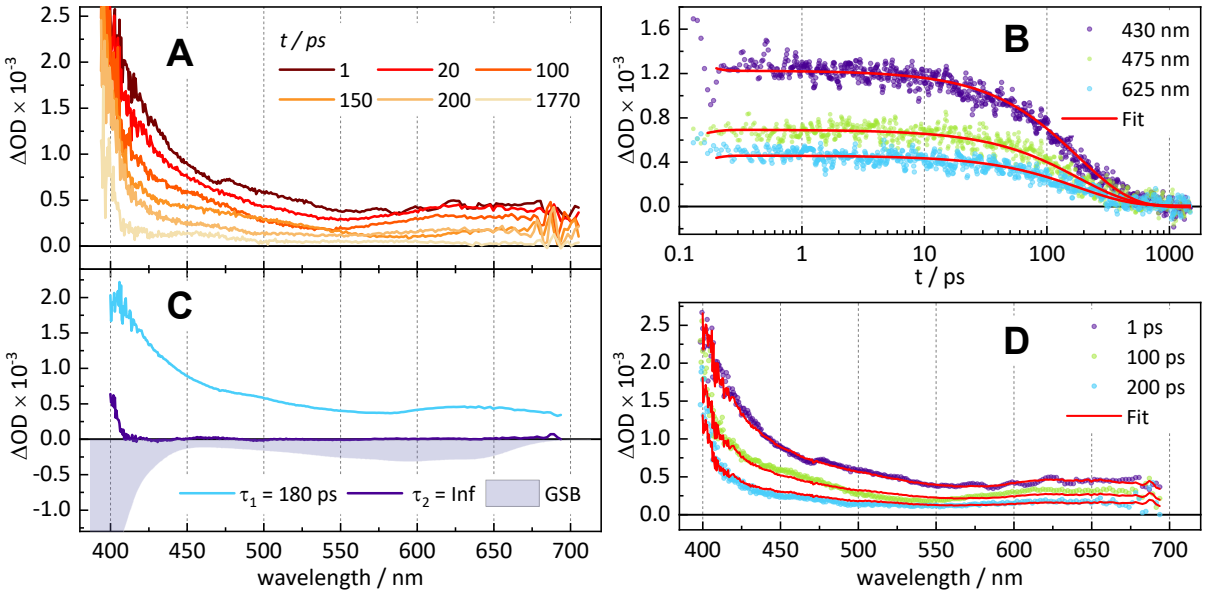

Figure S11, A: TA spectra of **[Fe((ImPh)$_2$P)$_2$]$^+$** dissolved in MeCN at different times t after optical excitation at 600 nm. B: Time traces (dots) at the specified probe wavelengths together with respective fit curves resulting from the GLA (red solid lines). C: DAS obtained by the GLA and labelled by the respective time constants. The dynamics is well described by a monoexponential decay with the time constant τ_1 = 180 ps. A further, long-lived component modelled by a decay with an infinite time constant τ_2 = Inf was used to account for tiny offsets at long delay times. The component is at almost all wavelengths practically zero and within the experimental accuracy insignificant. The negative of the ground state absorption is shown as grey area to indicate where ground state bleach (GSB) might contribute to the TA signal. D: TA spectra (dots) at the given time points together with fitted spectra obtained by the GLA (red solid lines).

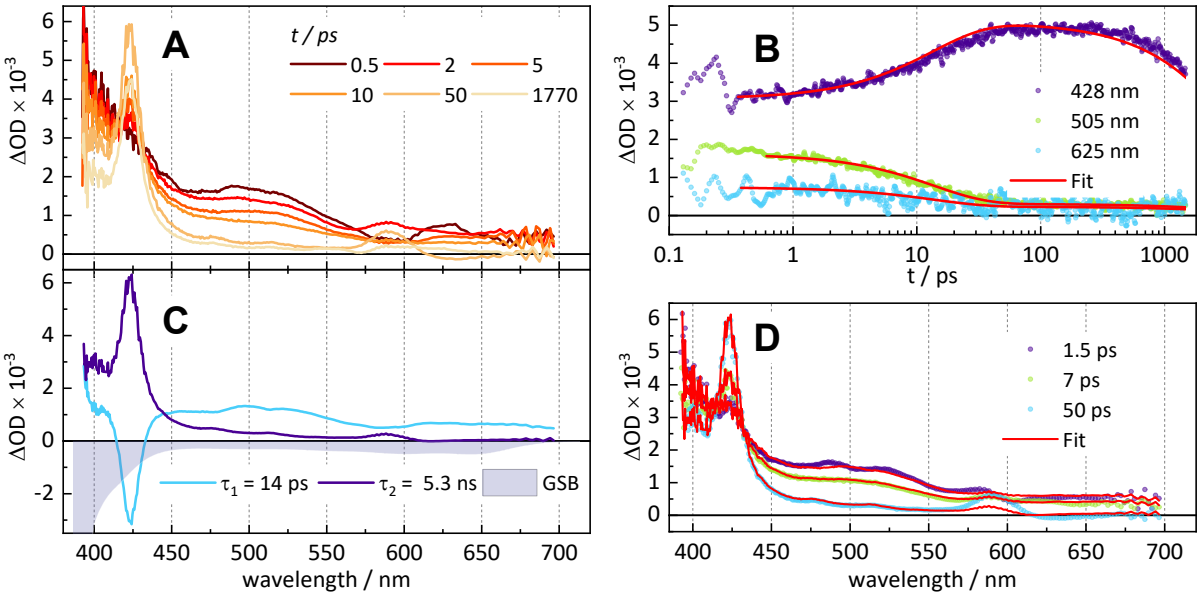

Figure S12, A: TA spectra of **[Fe(Im$_2$PAnt)$_2$]$^+$** dissolved in MeCN at different times t after optical excitation at 600 nm. B: Time traces (dots) at the specified probe wavelengths together with respective fit curves resulting from the GLA (red solid lines). C: DAS obtained by the GLA and labelled by the respective time constants. The dynamics is well described by a double exponential decay with the time constants τ_1 = 14 ps and τ_2 = 5.3 ns. The negative of the ground state absorption is shown as grey area to indicate where ground state bleach (GSB) might contribute to the TA signal. D: TA spectra (dots) at the given time points together with fitted spectra obtained by the GLA (red solid lines).

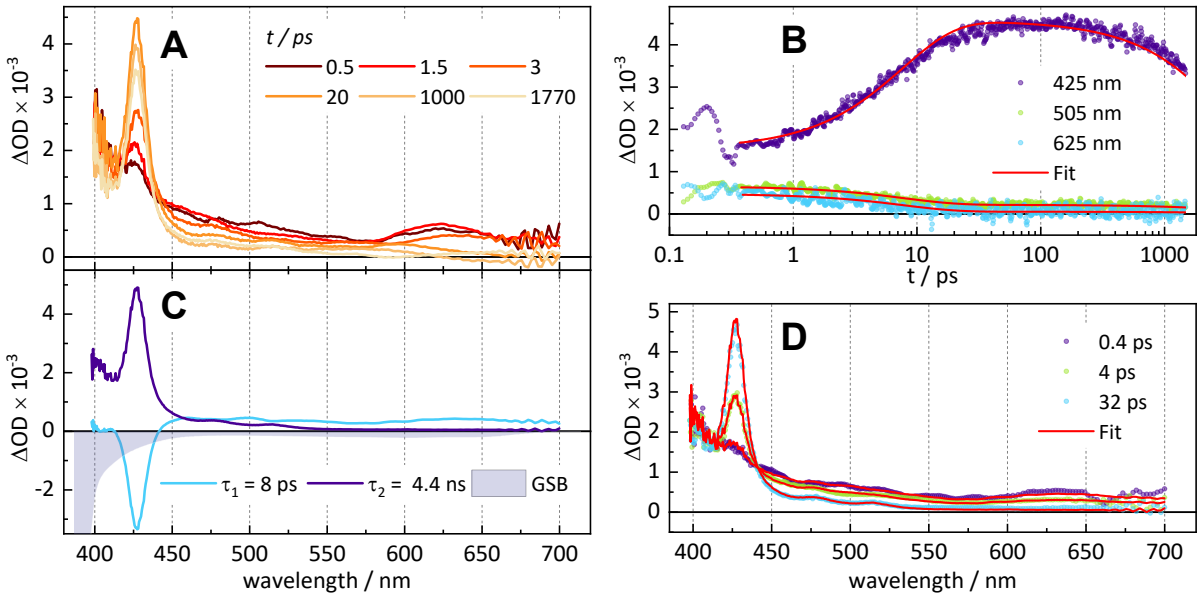

Figure S13, A: TA spectra of **[Fe((ImAnt)$_2$P)$_2$]$^+$** dissolved in MeCN at different times t after optical excitation at 600 nm. B: Time traces (dots) at the specified probe wavelengths together with respective fit curves resulting from the GLA (red solid lines). C: DAS obtained by the GLA and labelled by the respective time constants. The dynamics is well described by a double exponential decay with the time constants τ_1 = 8 ps and τ_2 = 4.4 ns. The negative of the ground state absorption is shown as grey area to indicate where ground state bleach (GSB) might contribute to the TA signal. D: TA spectra (dots) at the given time points together with fitted spectra obtained by the GLA (red solid lines).

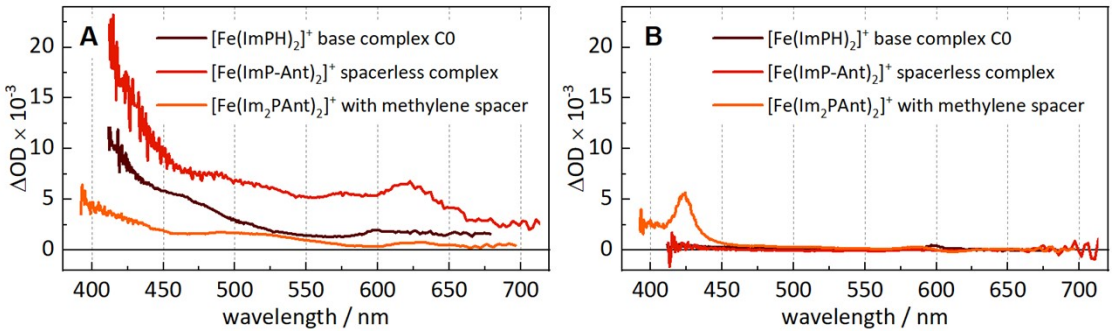

Figure S14: TA spectra of **[Fe(ImPH)$_2$]$^+$**, **[Fe(ImP-Ant)$_2$]$^+$** and **[Fe(Im$_2$PAnt)$_2$]$^+$** at a time delay of 0.5 ps (A) and at a time delay of 600 ps (B). The data from **[Fe(ImPH)$_2$]$^+$** and **[Fe(ImP-Ant)$_2$]$^+$** were adopted from our previous publication.[19] At 0.5 ps the TA signatures of all three compounds are similar indicating that in all cases the LMCT state is initially populated. At 600 ps **[Fe(ImPH)$_2$]$^+$** and **[Fe(ImP-Ant)$_2$]$^+$** show no TA signal any more since the excited state population has already returned to the ground state. In the case of **[Fe(Im$_2$PAnt)$_2$]$^+$** a rather sharp band at about 425 nm remains which is characteristic for the triplet state of anthracene. This demonstrates that at longer delay times the excited state population resides in the local triplet state of the anthracene moiety.

9. TD-DFT calculations

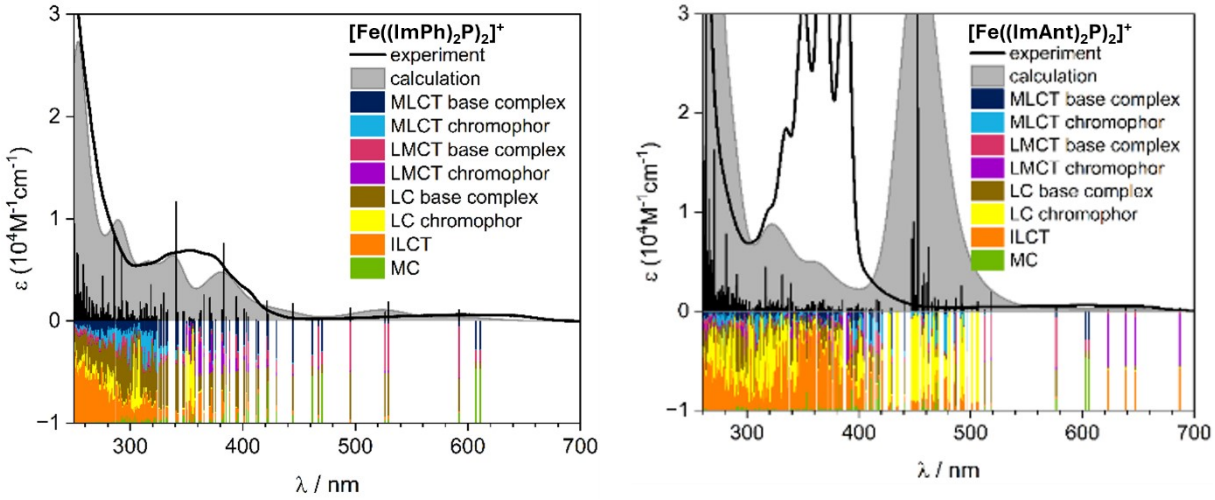

Figure S15: Experimental and TD-DFT-calculated UV-Vis spectra (broadened with a full-width at half maximum (FWHM) of 2000 cm^{-1}) of **$[Fe((ImPh)_2P)_2]^+$** and **$[Fe((ImAnt)_2P)_2]^+$**. LC refers to electronic transitions where the charge remains localized within the same part of the ligand (base complex ligand or chomophore), whereas ILCT describes charge transfer between different regions within the same ligand.

10. NMR-spectroscopy

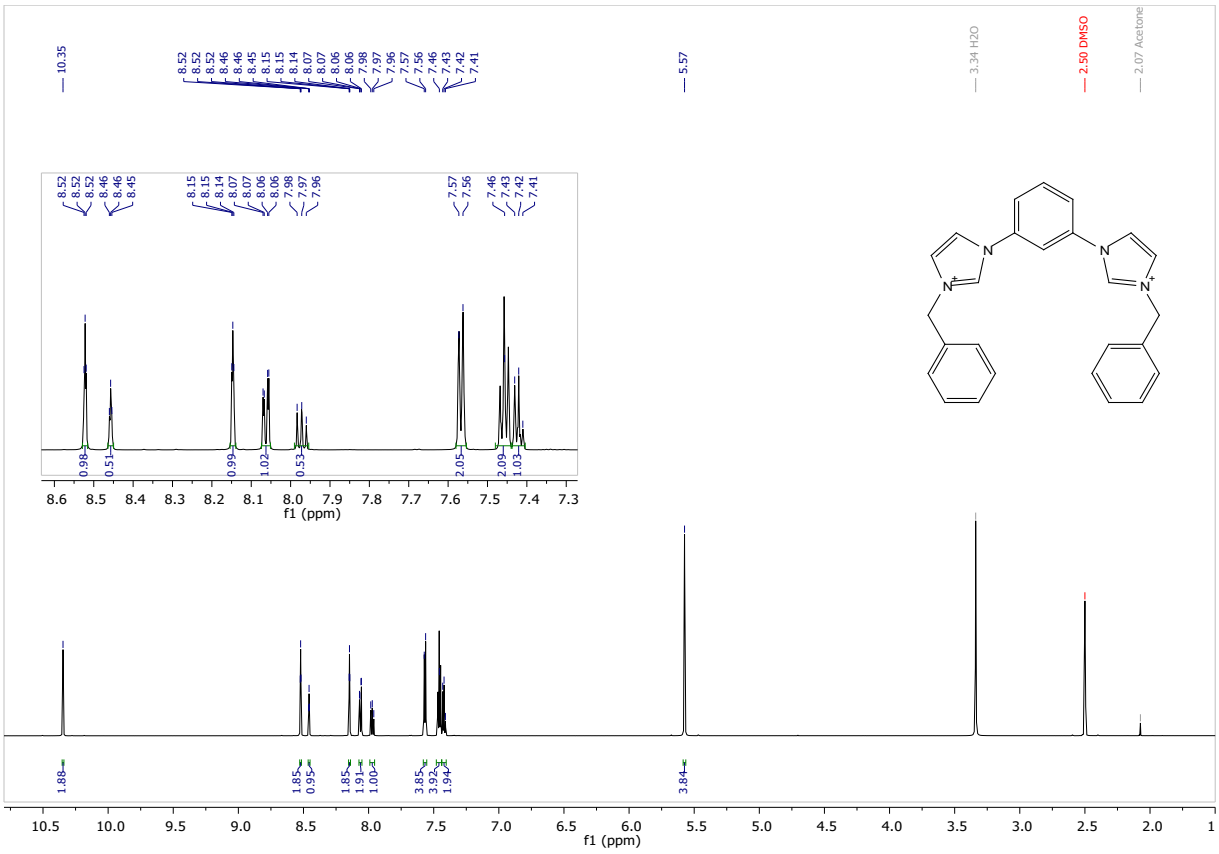

Figure S16: 1H-NMR spectrum of 2-Ph

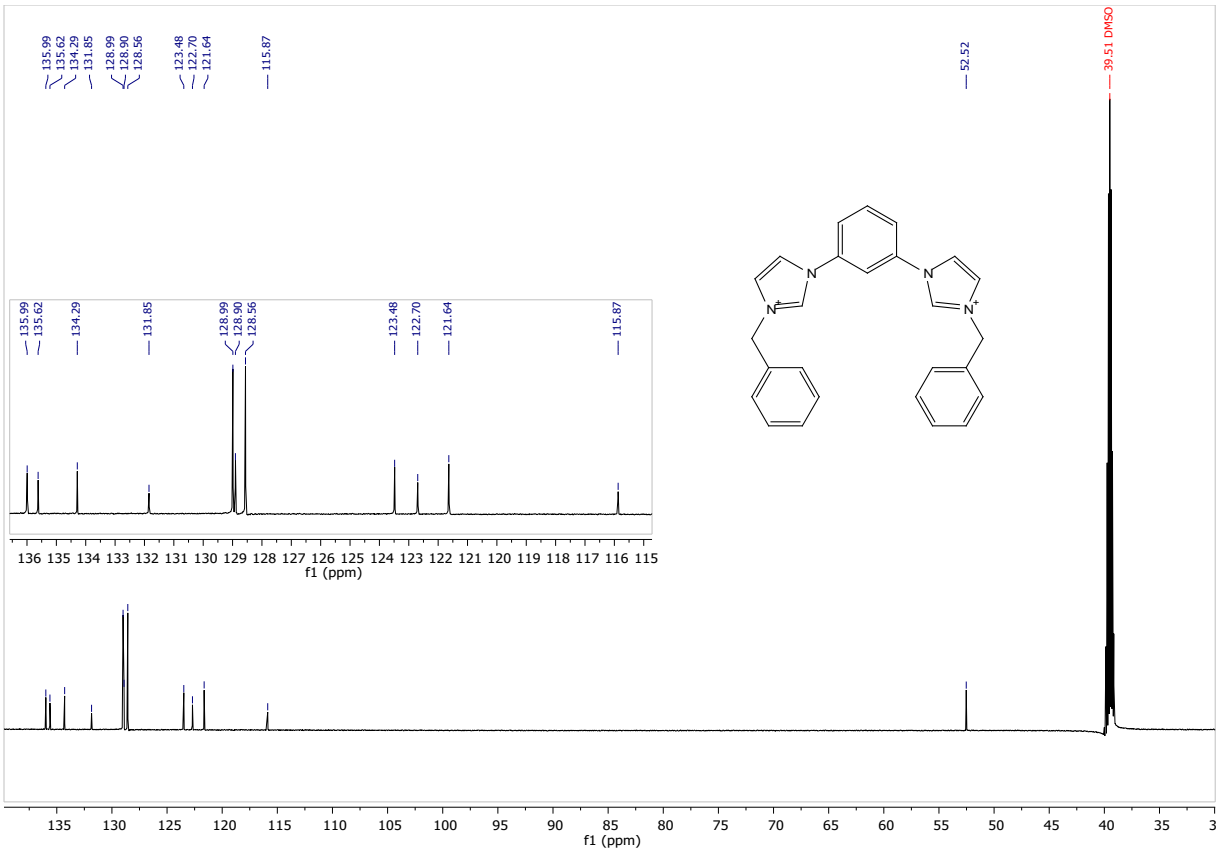

Figure S17: ^{13}C-NMR spectrum of **2-Ph**

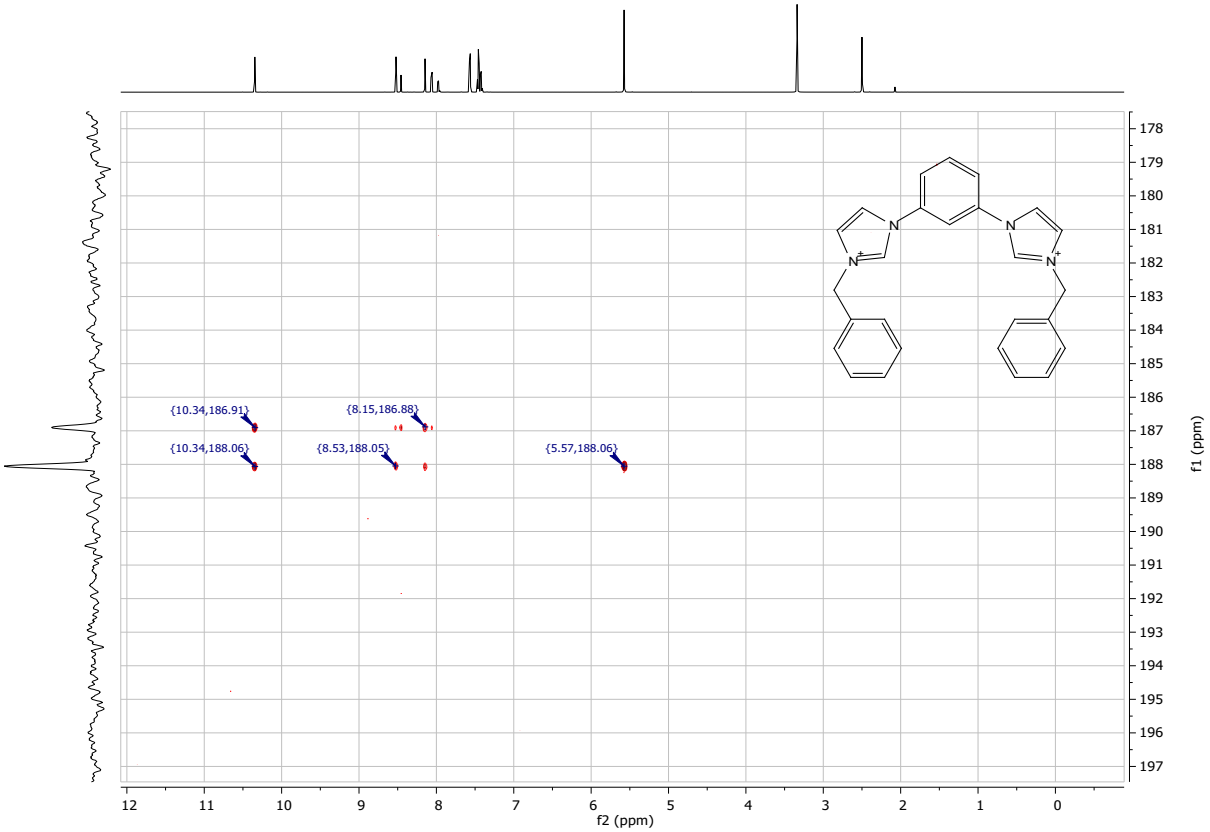

Figure S18: ^{15}N-NMR spectrum of **2-Ph**

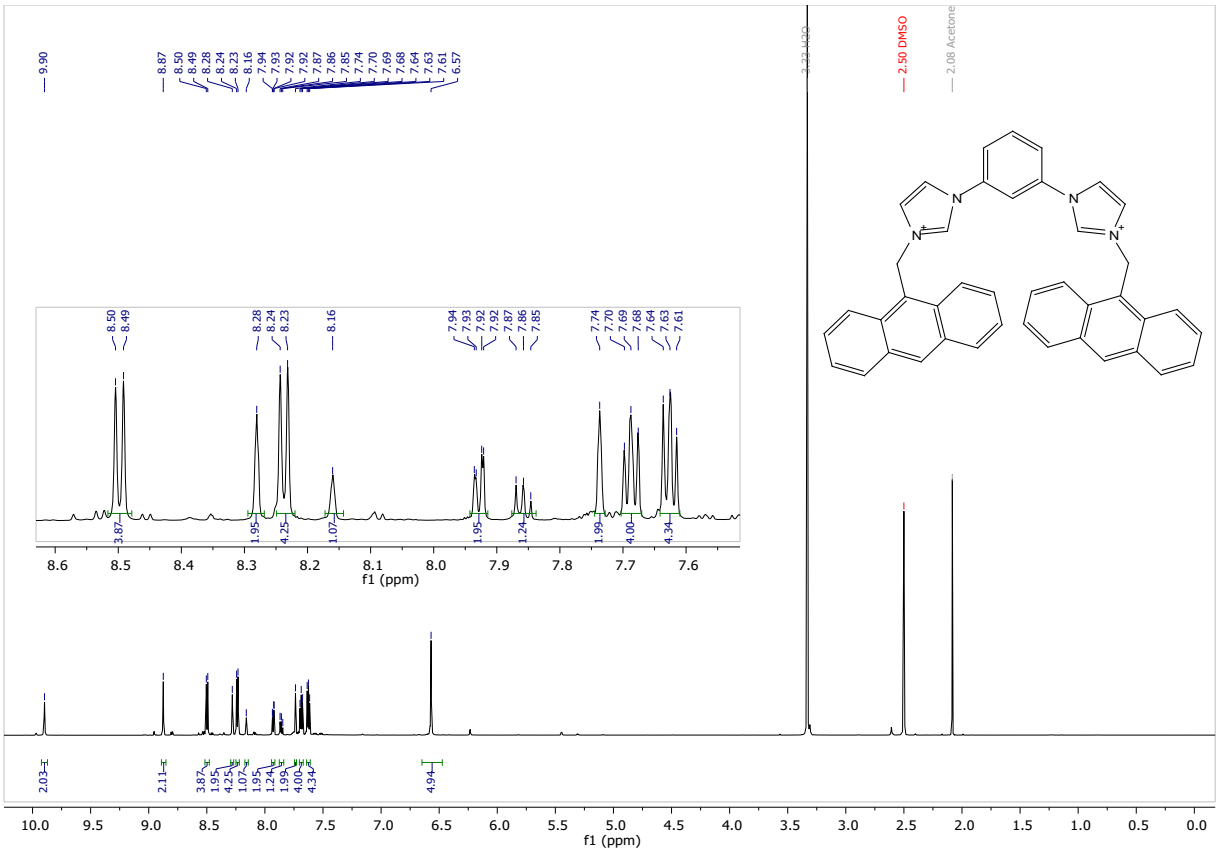

Figure S19: ^{1}H-NMR spectrum of **2-Ant**

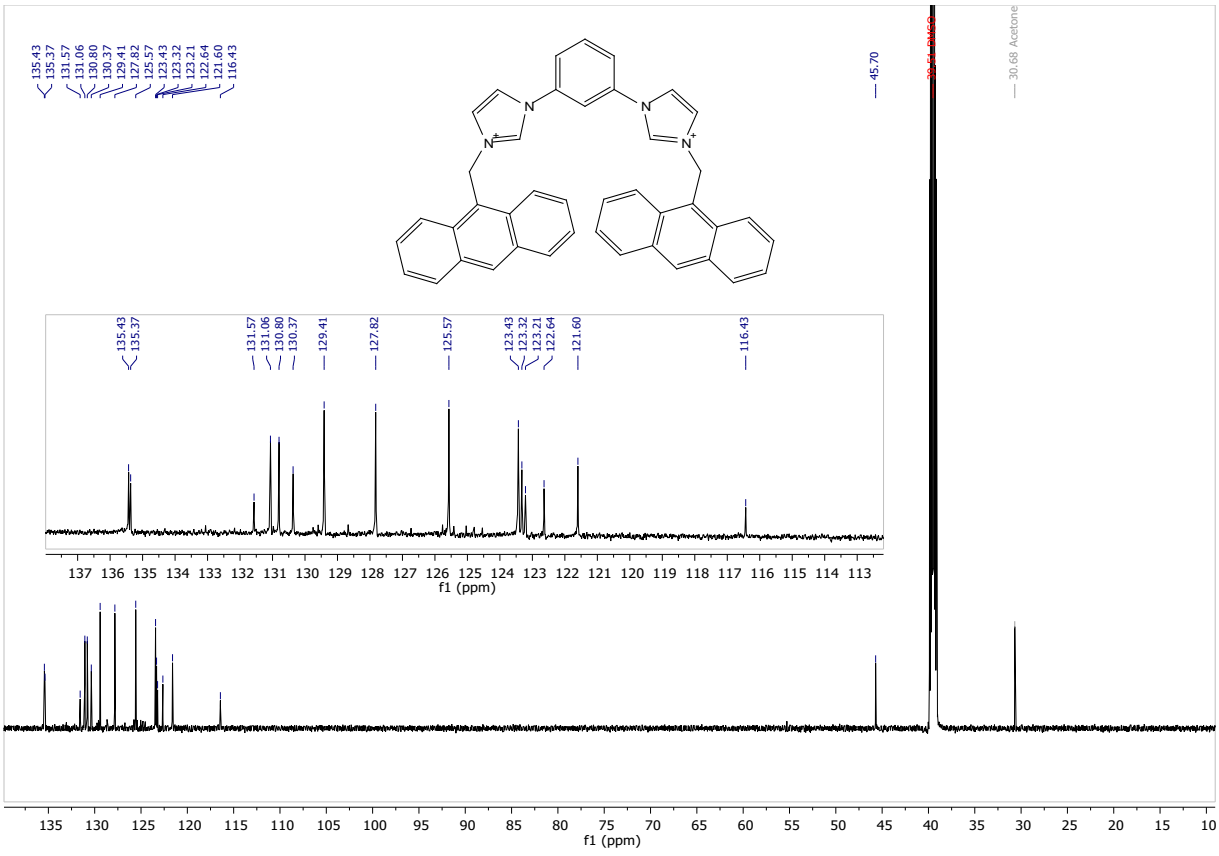

Figure S20: ^{13}C-NMR spectrum of **2-Ant**

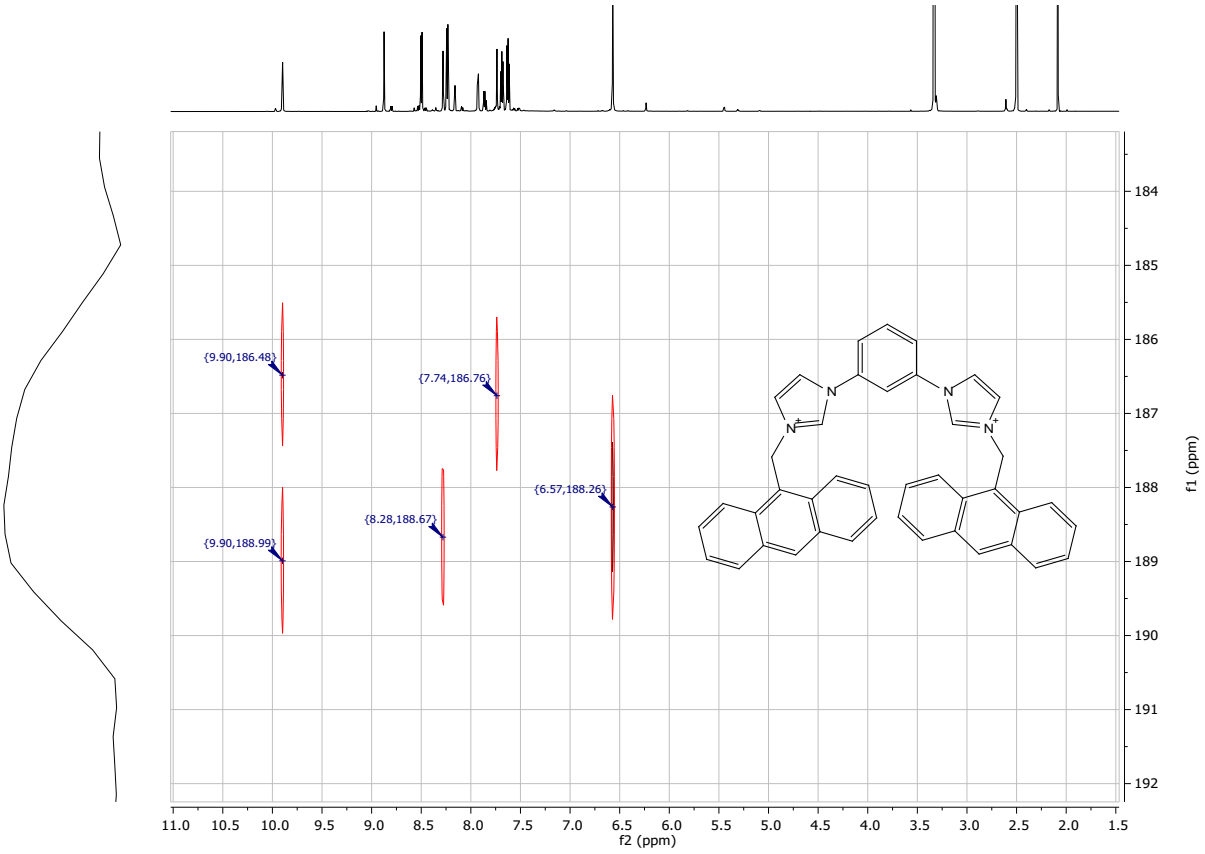

Figure S21: ^{15}N-NMR spectrum of **2-Ant**

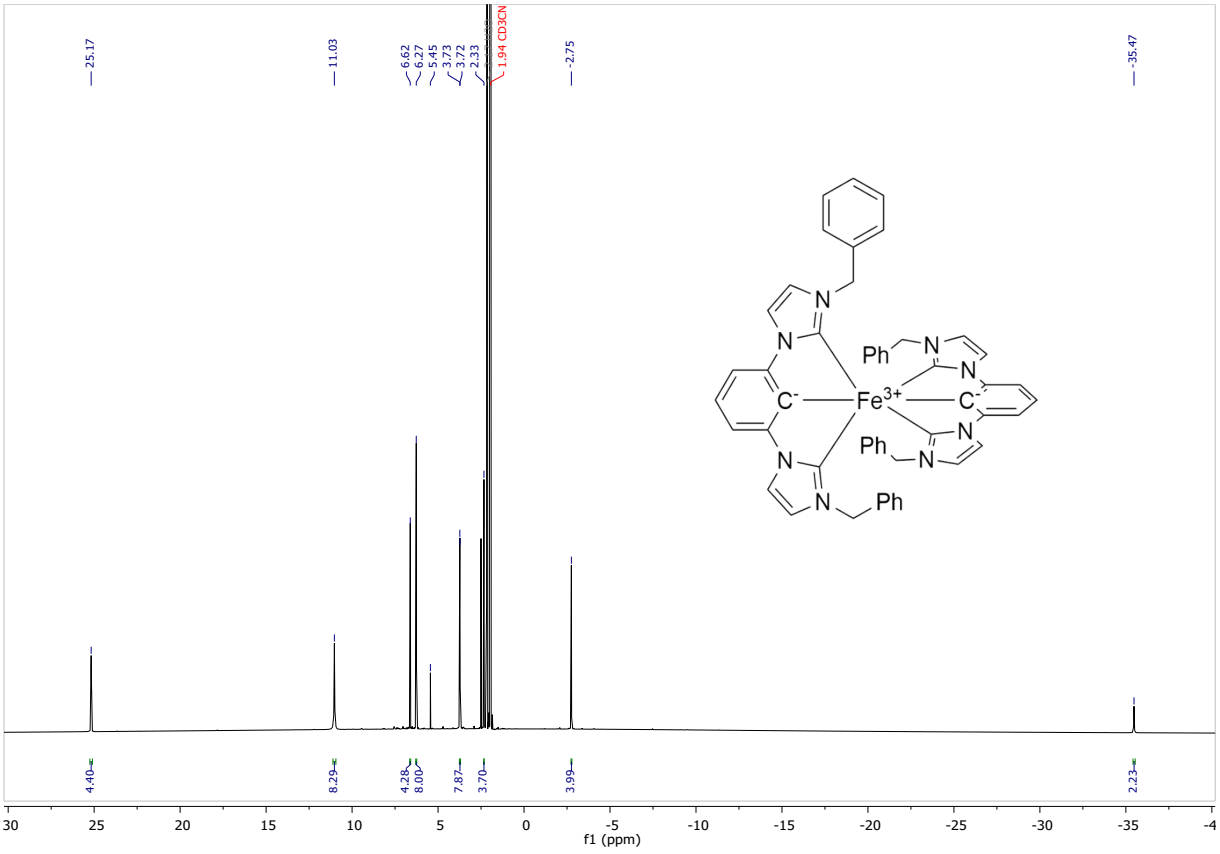

Figure S22: ^{1}H-NMR spectrum of **[Fe((ImPh)$_2$P)$_2$]$^{+}$**

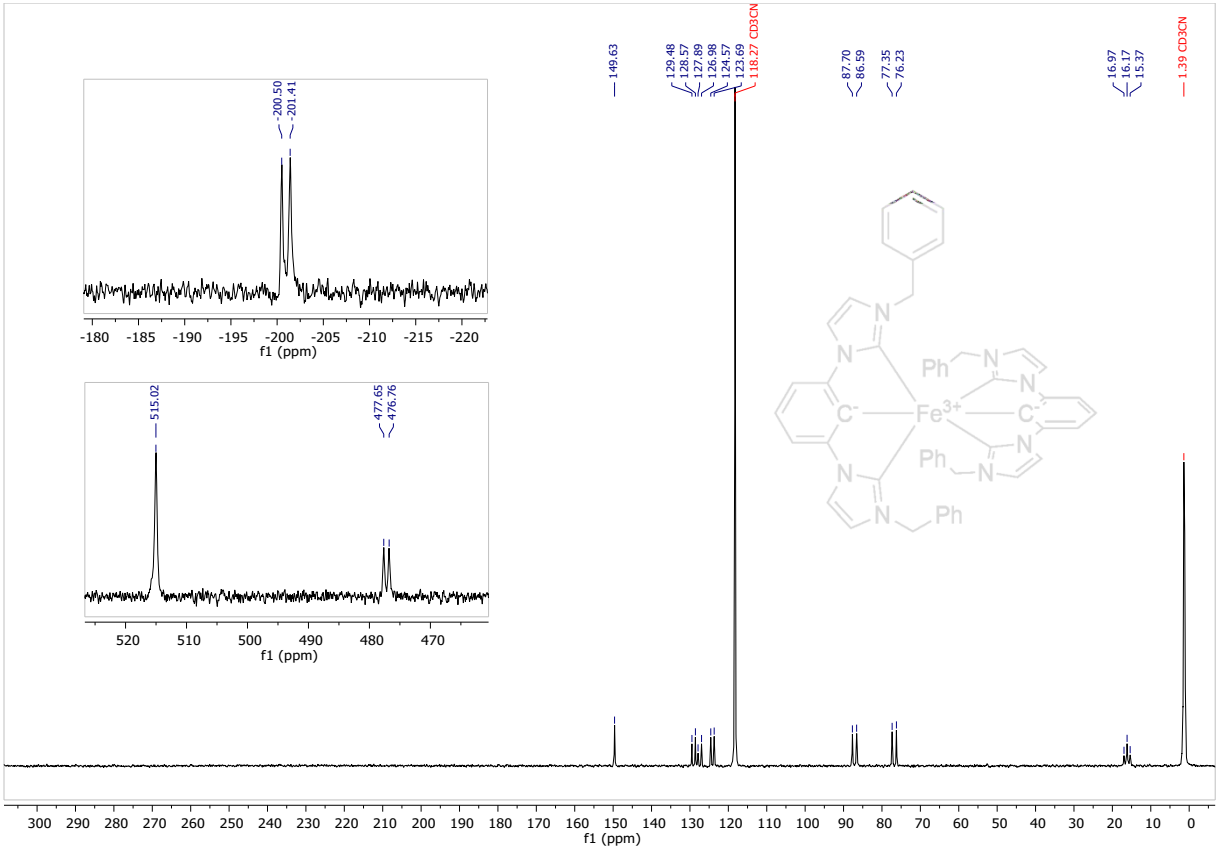

Figure S23: 13C-NMR spectrum of **[Fe((ImPh)$_2$P)$_2$]$^{+}$**

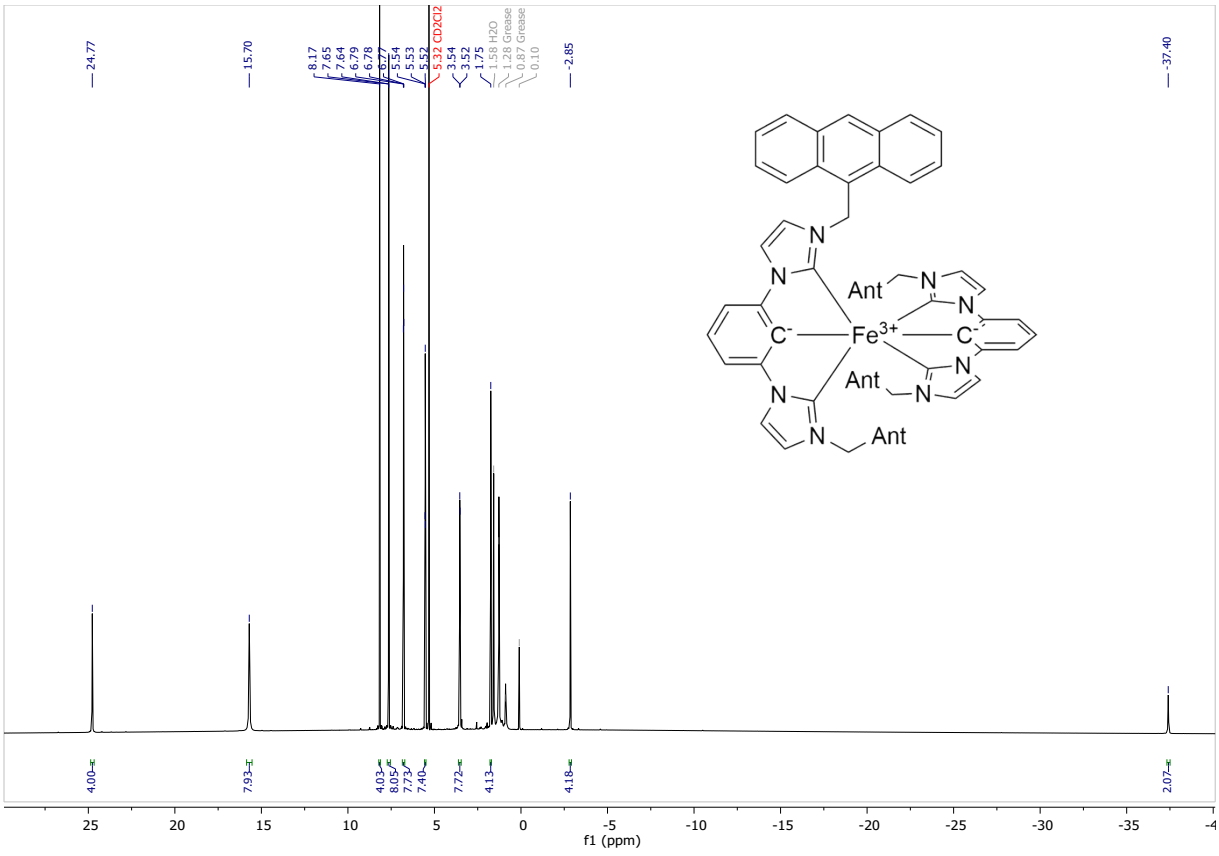

Figure S24: ^{1}H-NMR spectrum of **[Fe((ImAnt)$_2$P)$_2$]$^{+}$**

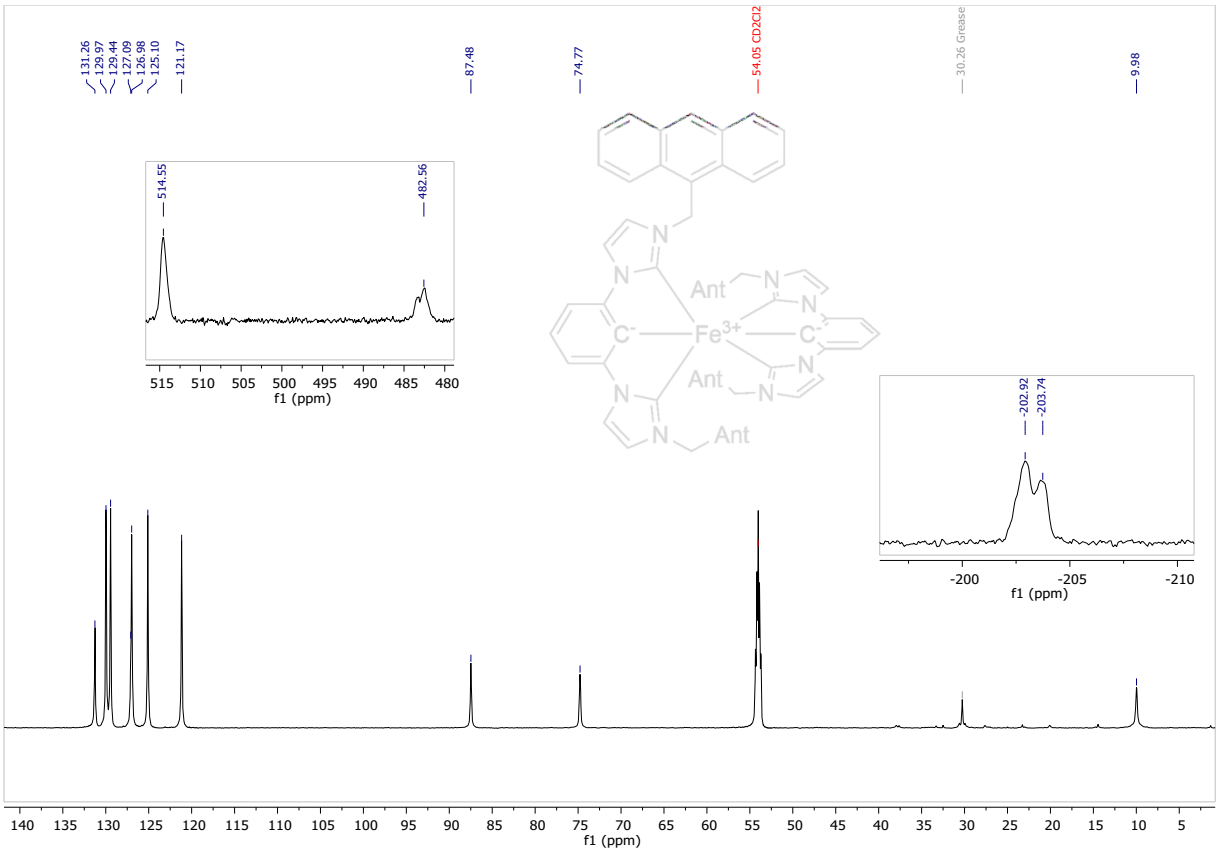

Figure S25: 13C-NMR spectrum of **[Fe((ImAnt)$_2$P)$_2$]$^+$**

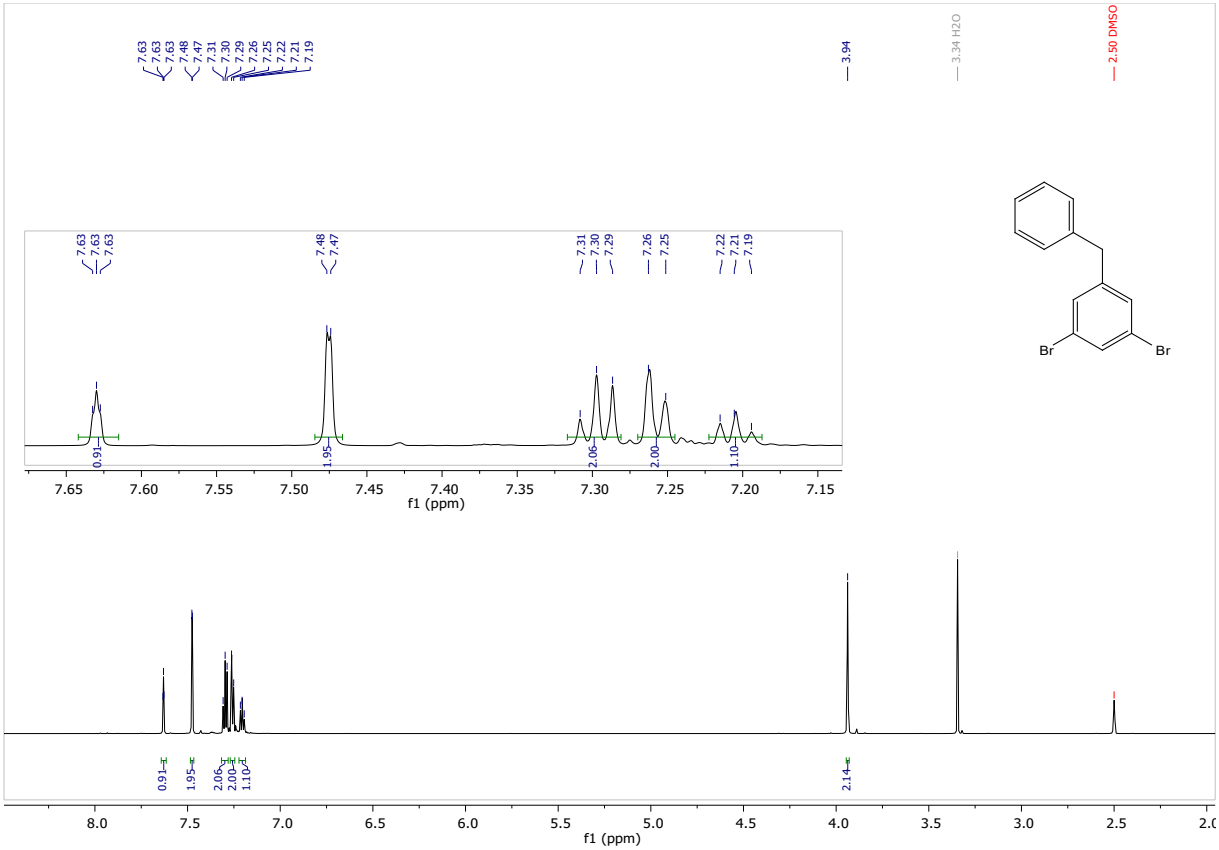

Figure S26: ^{1}H-NMR spectrum of **3-Ph**

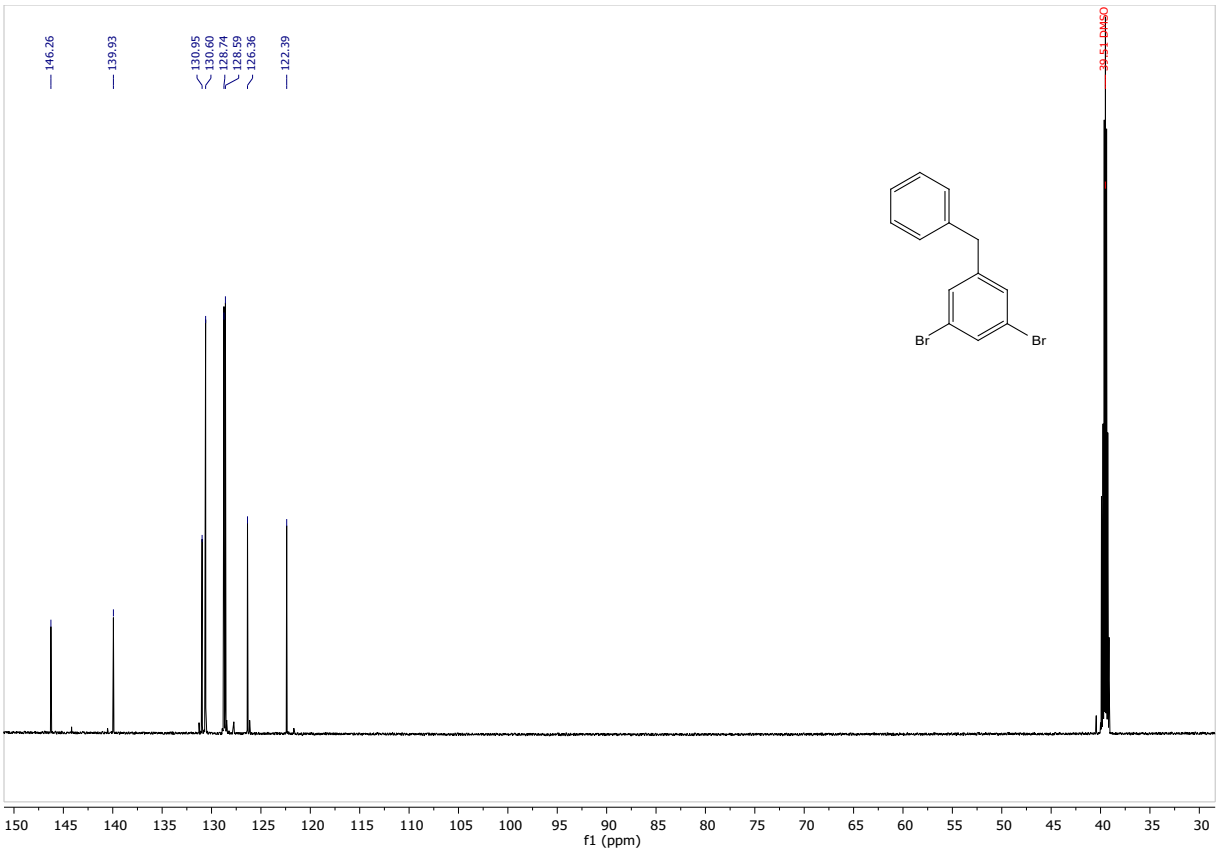

Figure S27: ^{13}C-NMR spectrum of **3-Ph**

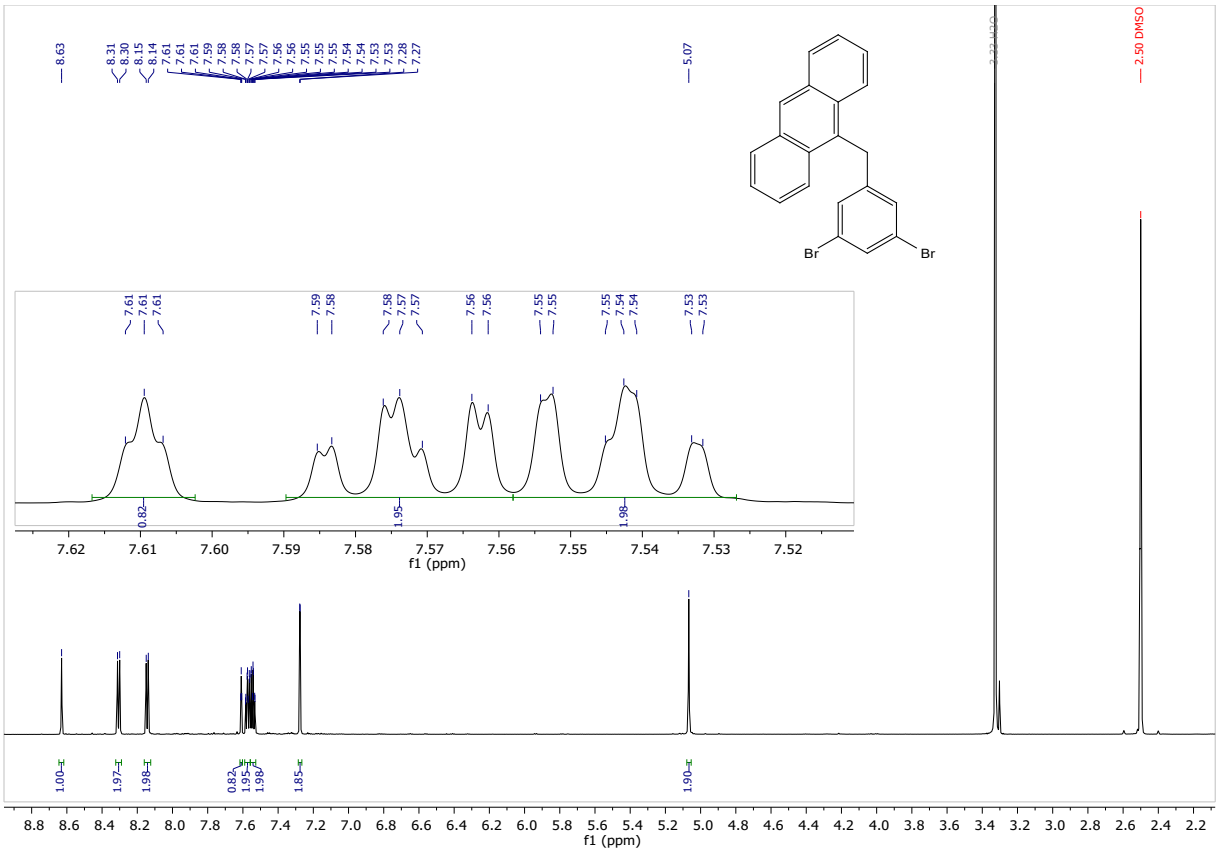

Figure S28: ^{1}H-NMR spectrum of **3-Ant**

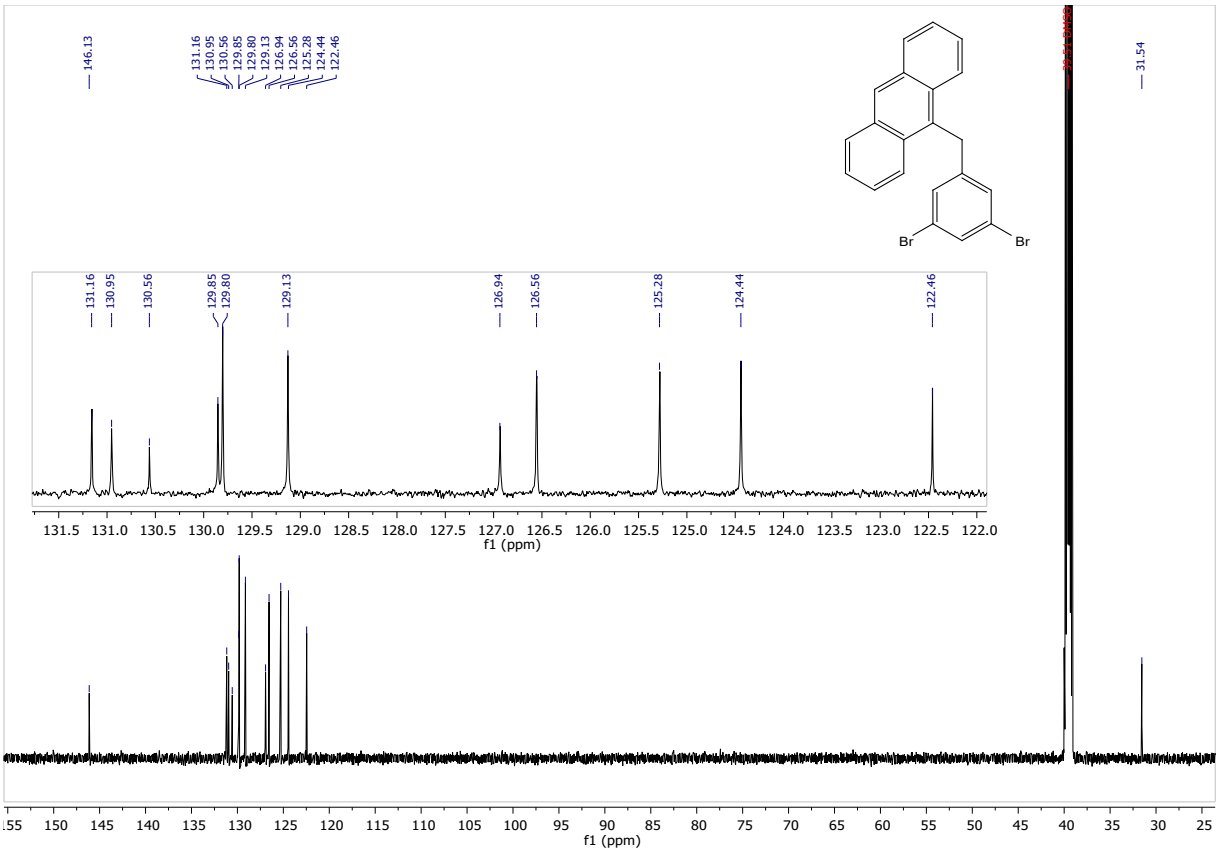

Figure S29: ^{13}C-NMR spectrum of **3-Ant**

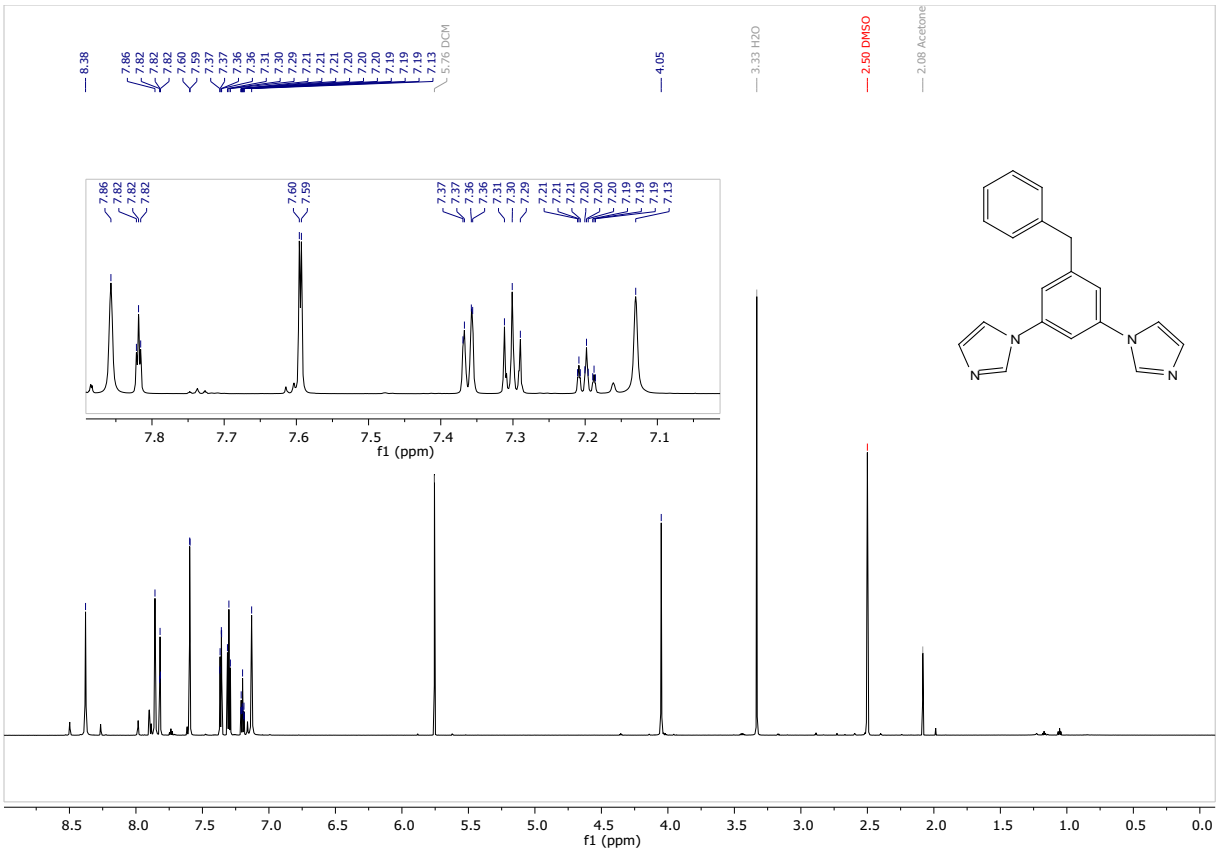

Figure S30: ^{1}H-NMR spectrum of **4-Ph**

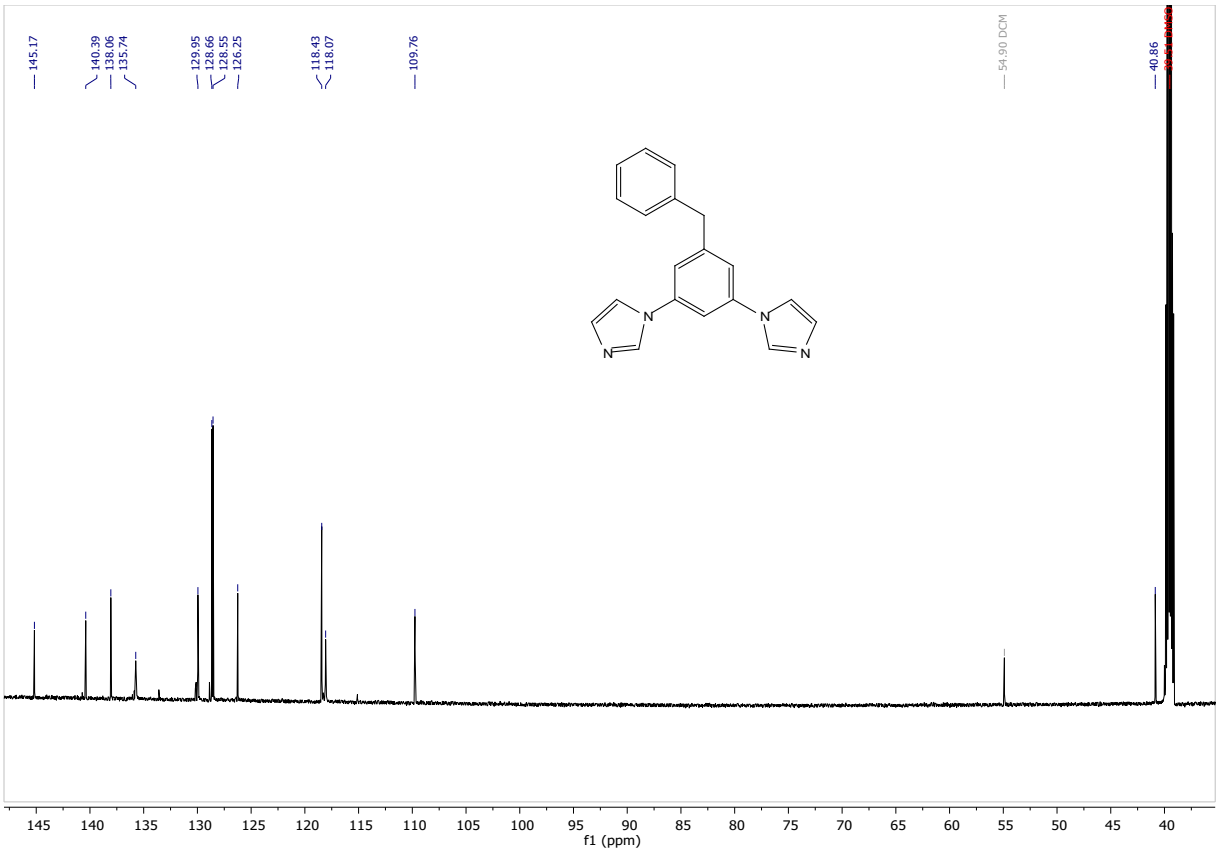

Figure S31: ^{13}C-NMR spectrum of **4-Ph**

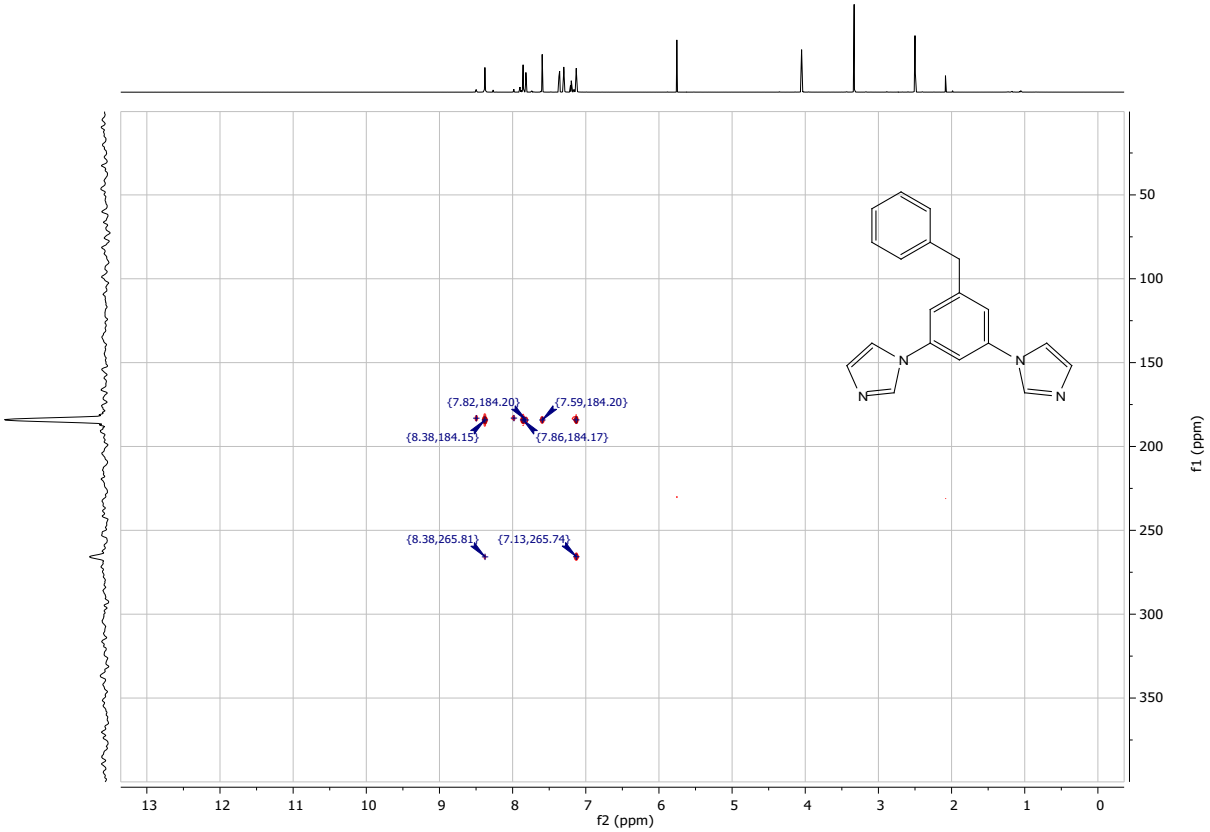

Figure S32: ^{15}N-NMR spectrum of **4-Ph**

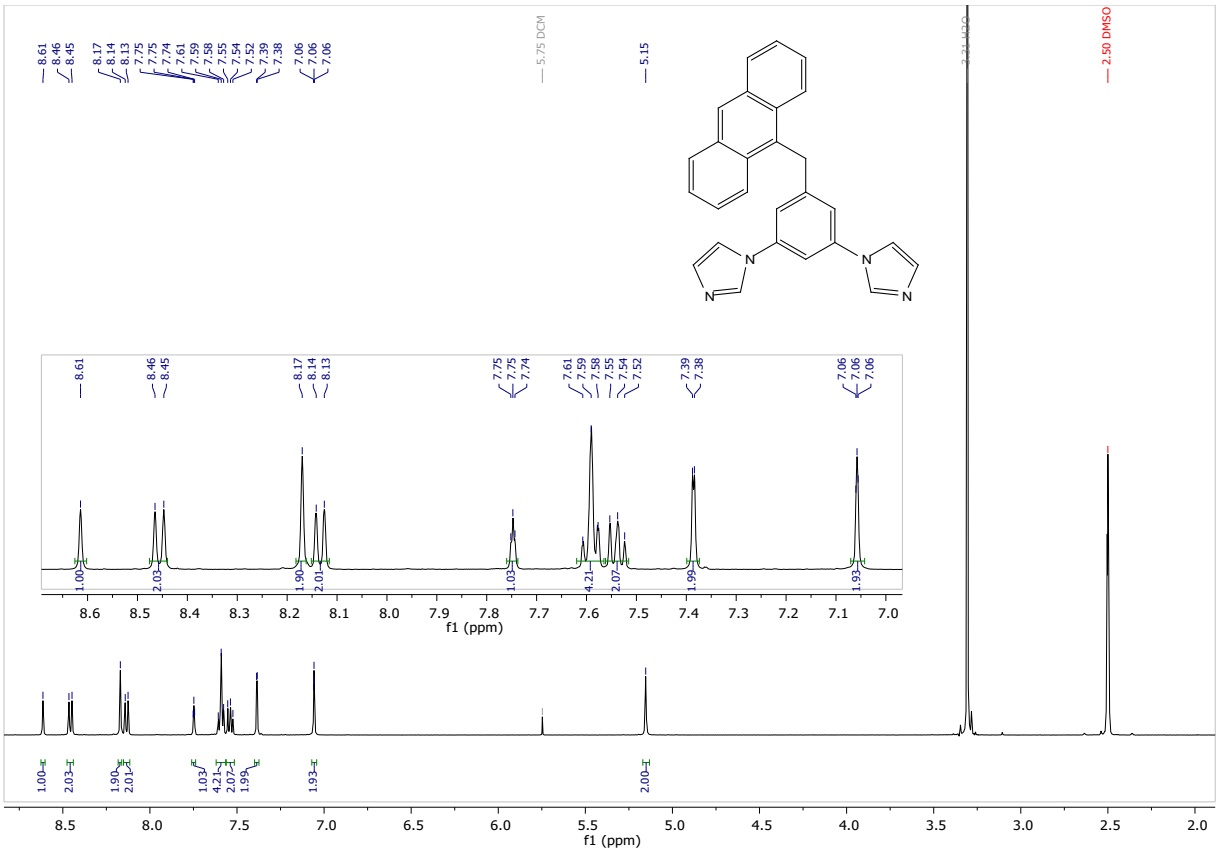

Figure S33: ^{1}H-NMR spectrum of **4-Ant**

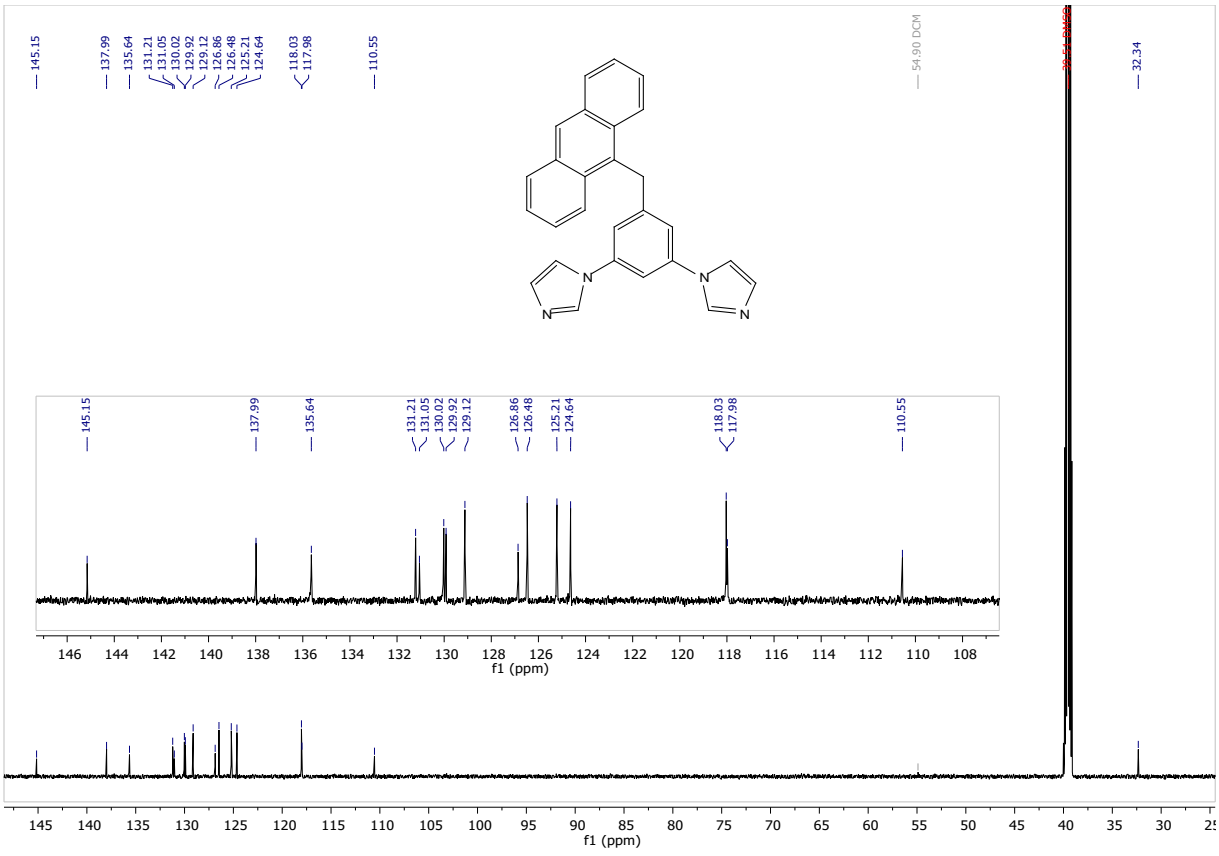

Figure S34: ^{13}C-NMR spectrum of **4-Ant**

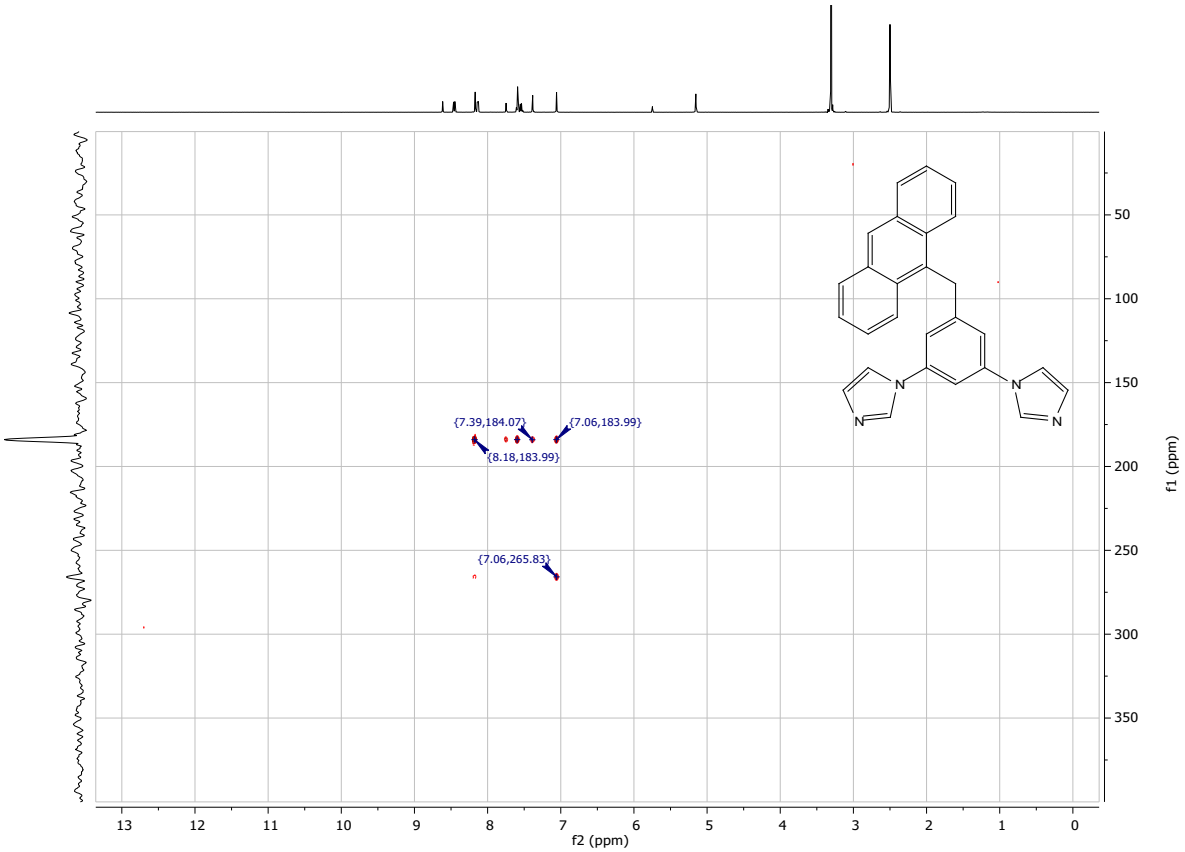

Figure S35: ^{15}N-NMR spectrum of **4-Ant**

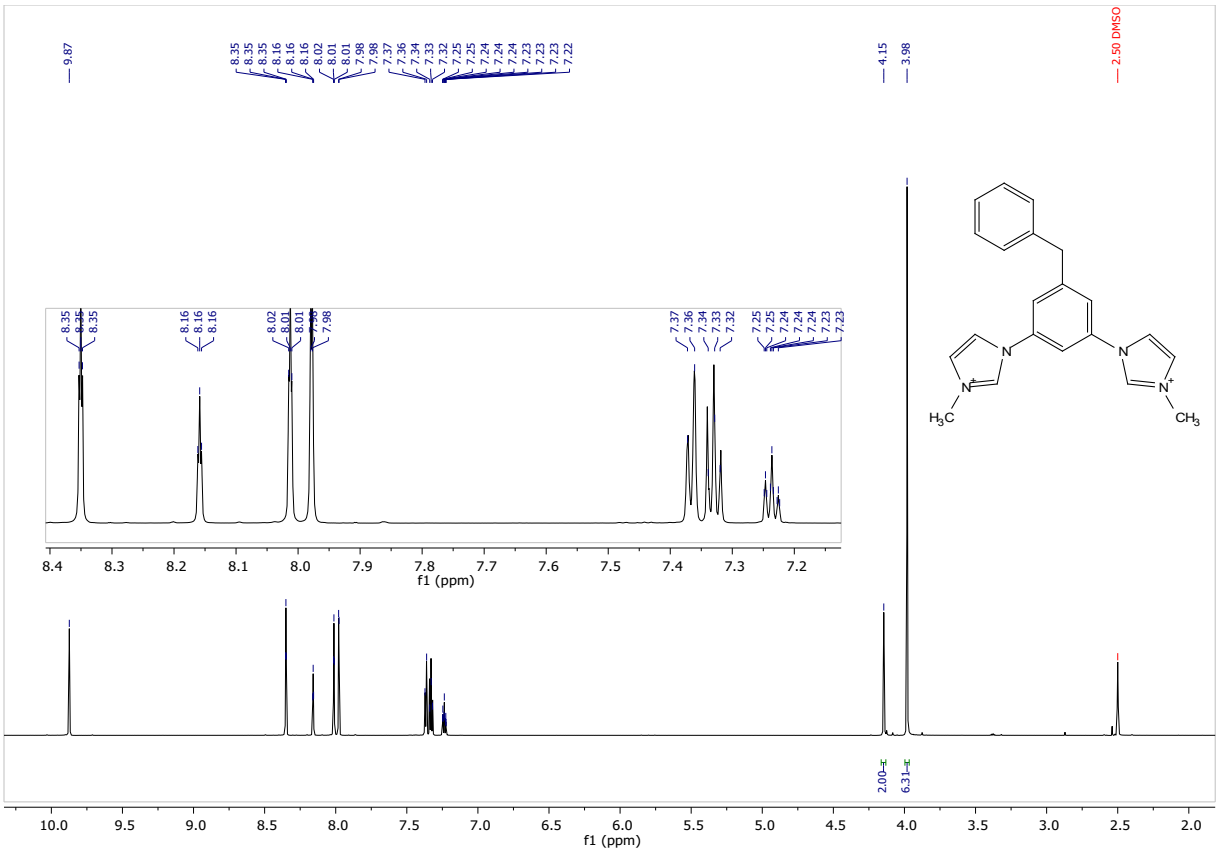

Figure S36: ^{1}H-NMR spectrum of **5-Ph**

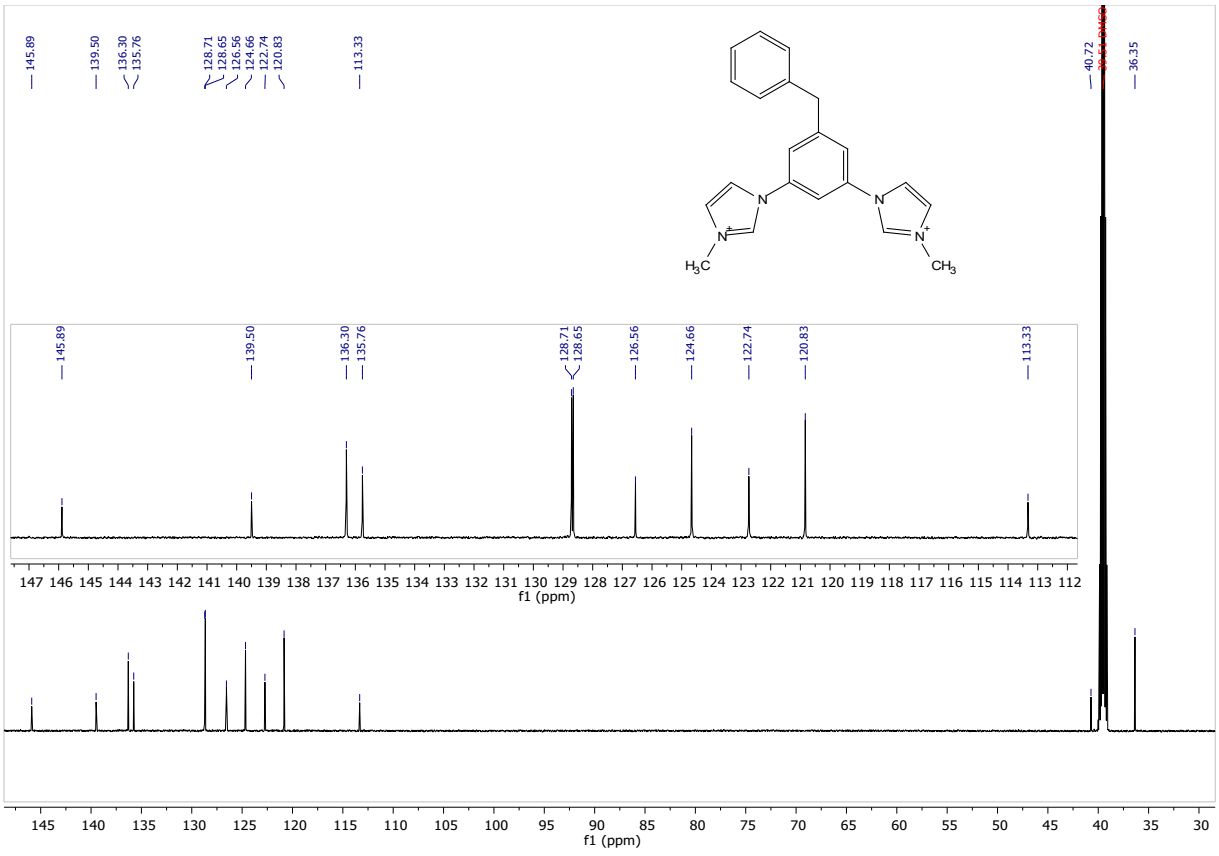

Figure S37: ^{13}C-NMR spectrum of **5-Ph**

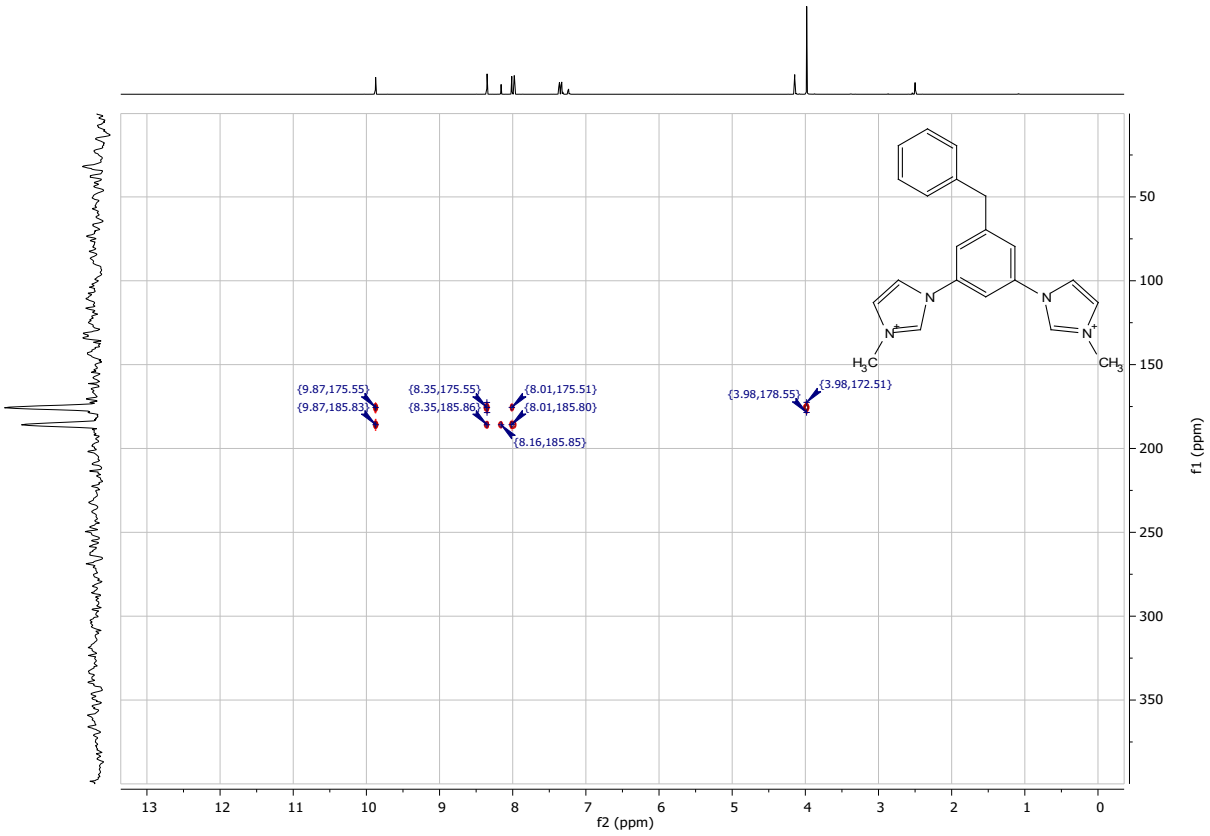

Figure S38: ^{15}N-NMR spectrum of **5-Ph**

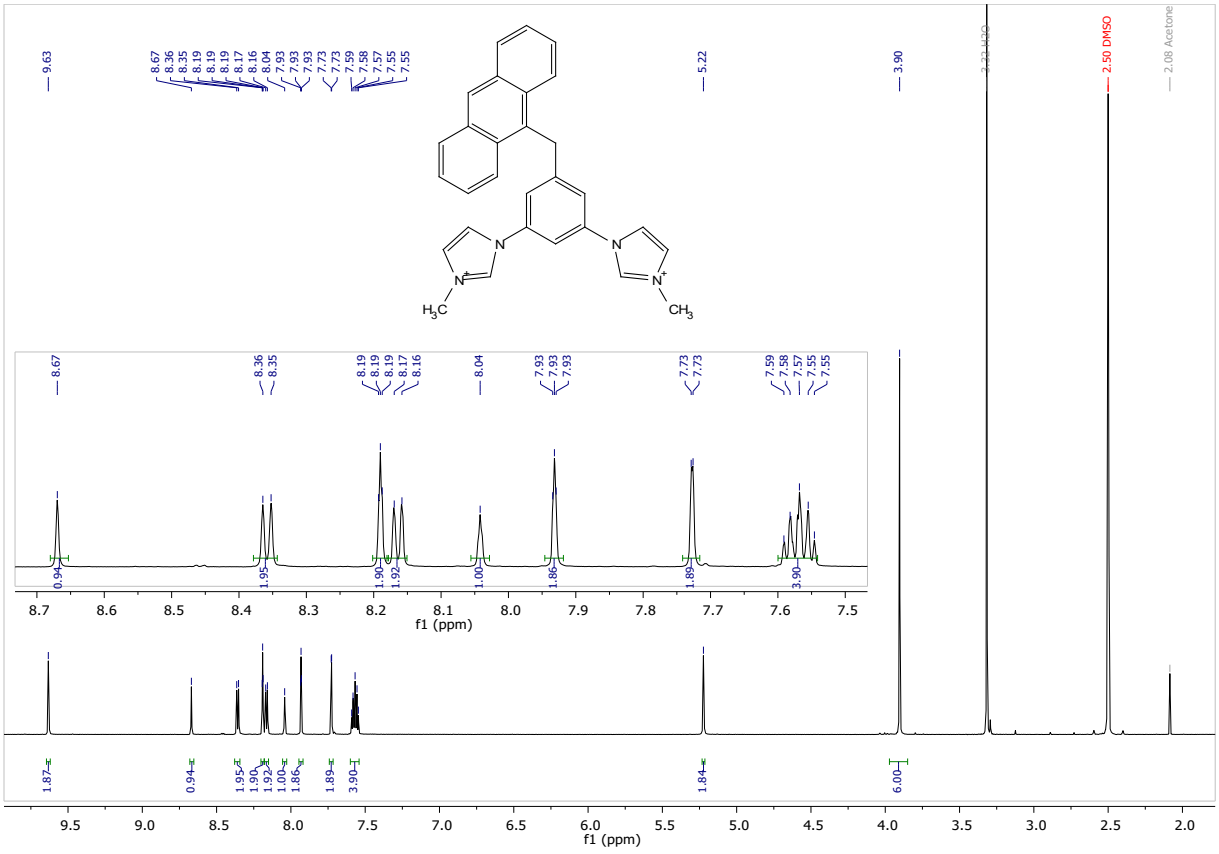

Figure S39: ^{1}H-NMR spectrum of **5-Ant**

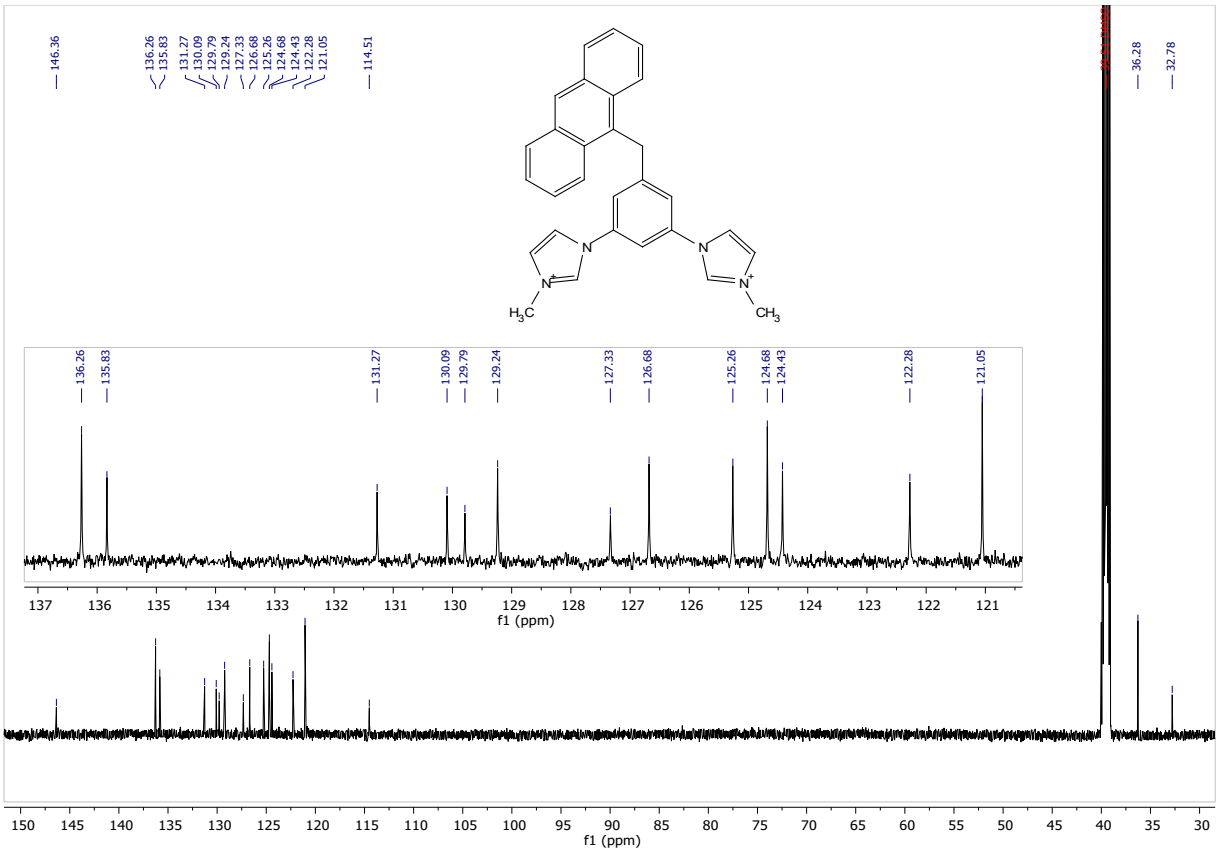

Figure S40: ^{13}C-NMR spectrum of **5-Ant**

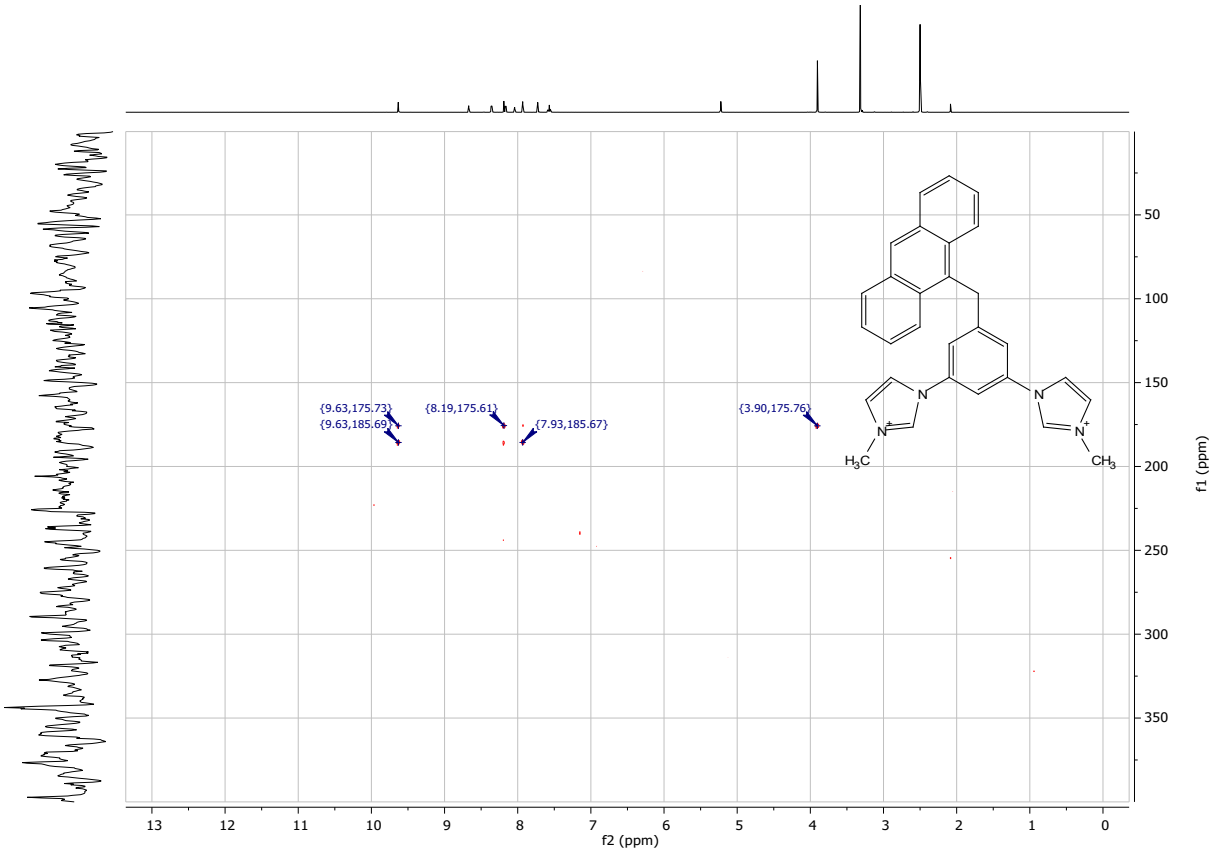

Figure S41: ^{15}N-NMR spectrum of **5-Ant**

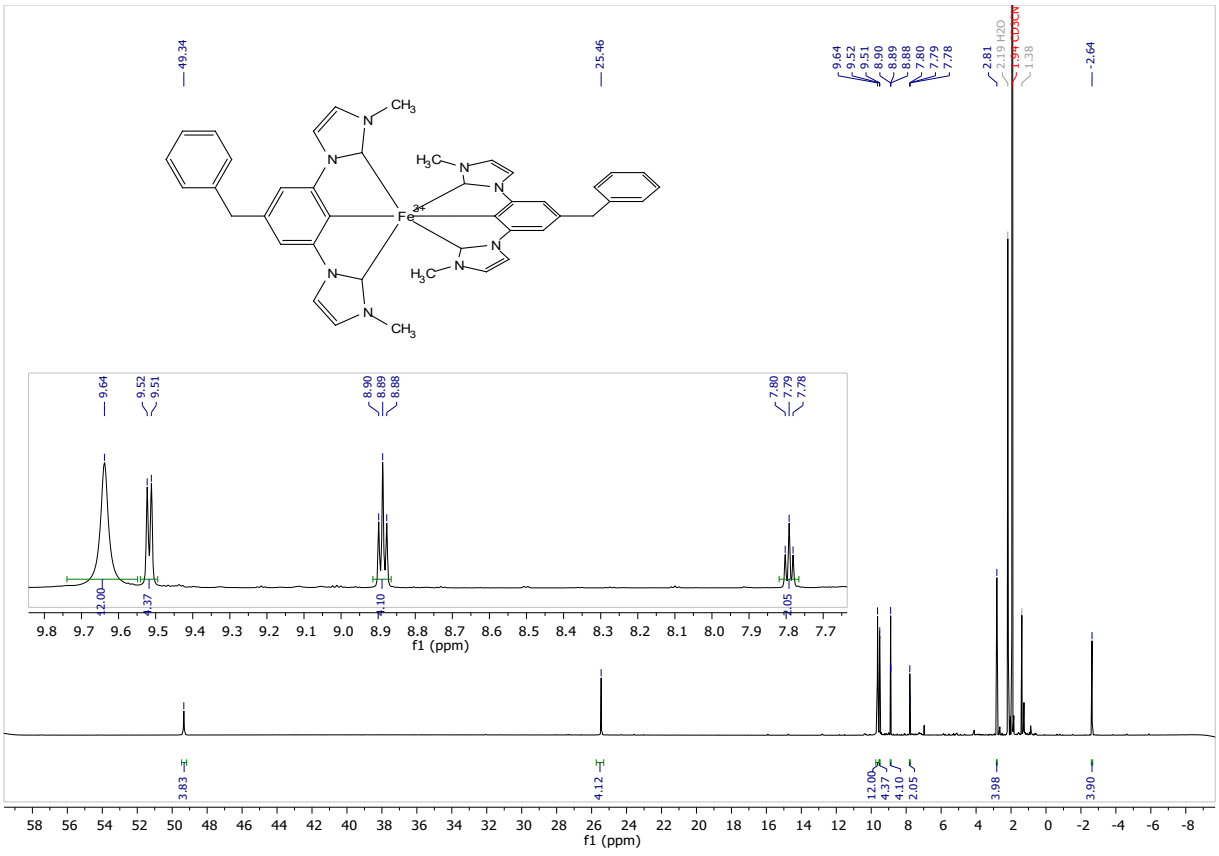

Figure S42: ^{1}H-NMR spectrum of **[Fe(Im$_2$PPh)$_2$]$^{+}$**

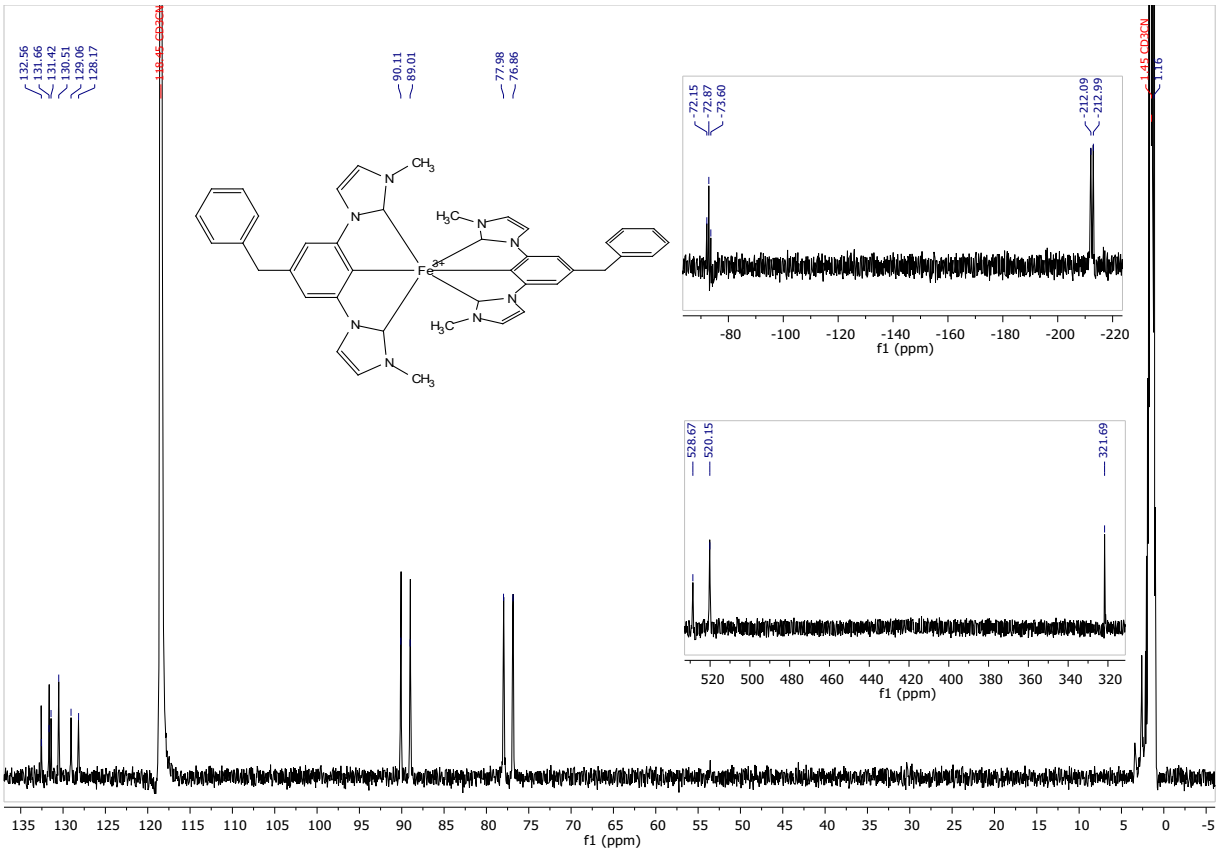

Figure S43: ^{13}C-NMR spectrum of **[Fe(Im$_2$PPh)$_2$]$^+$**

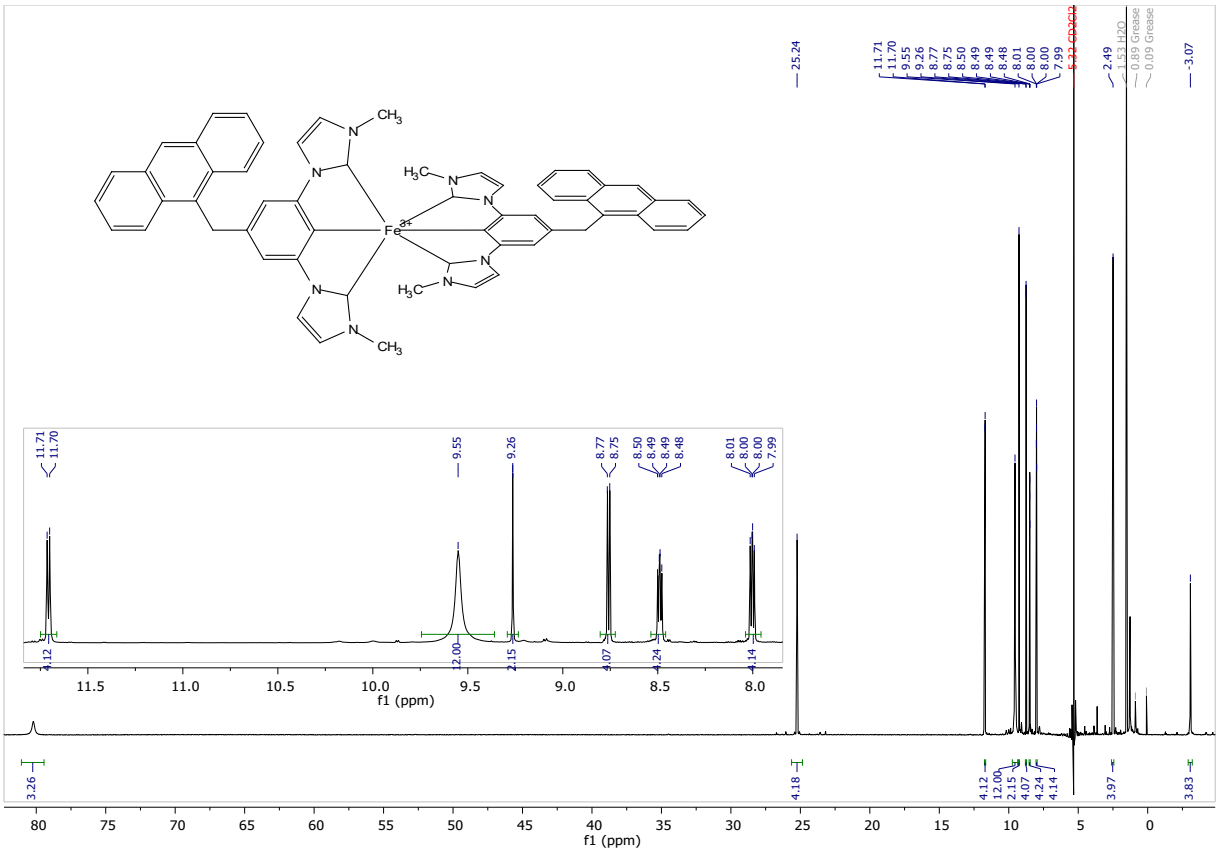

Figure S44: ^{1}H-NMR spectrum **[Fe(Im$_2$PAnt)$_2$]$^{+}$**

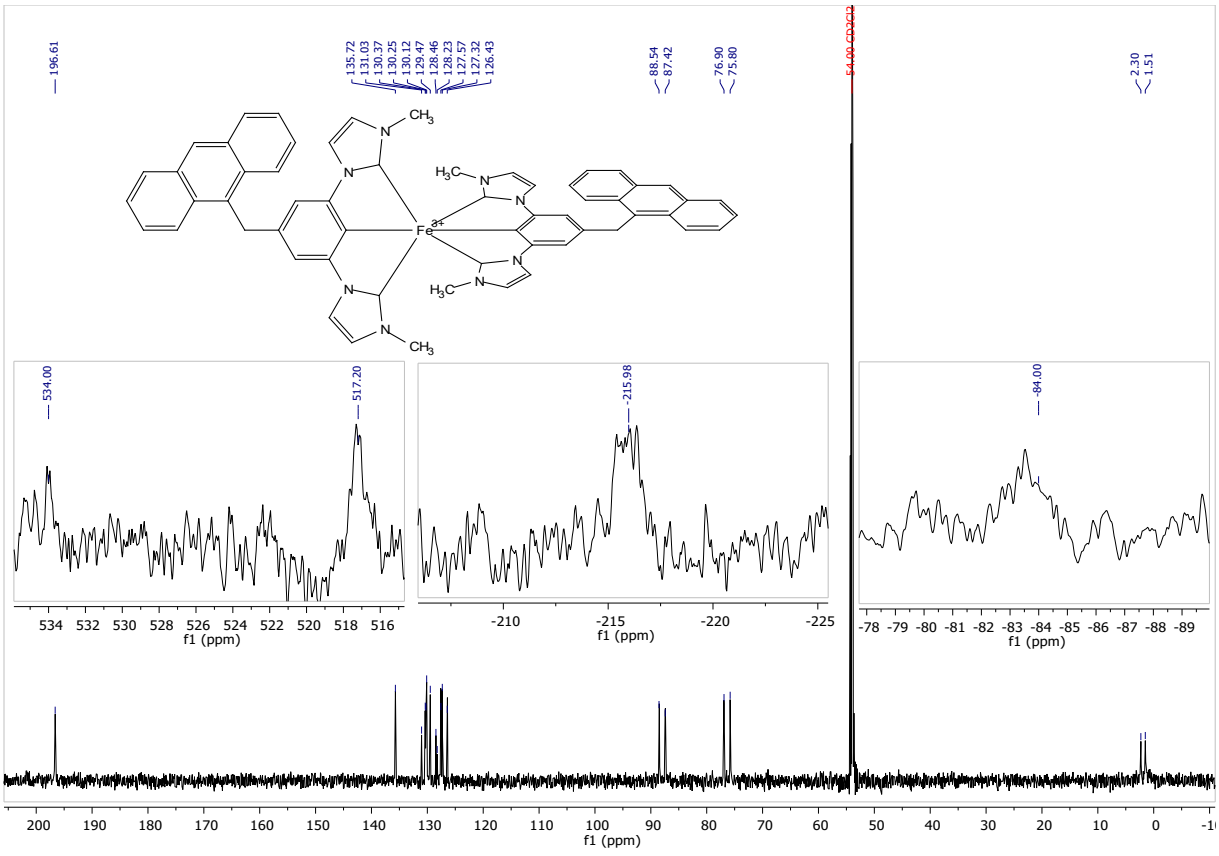

Figure S45: ^{13}C-NMR spectrum of **[Fe(Im$_2$PAnt)$_2$]$^+$**

11. Mass spectroscopy

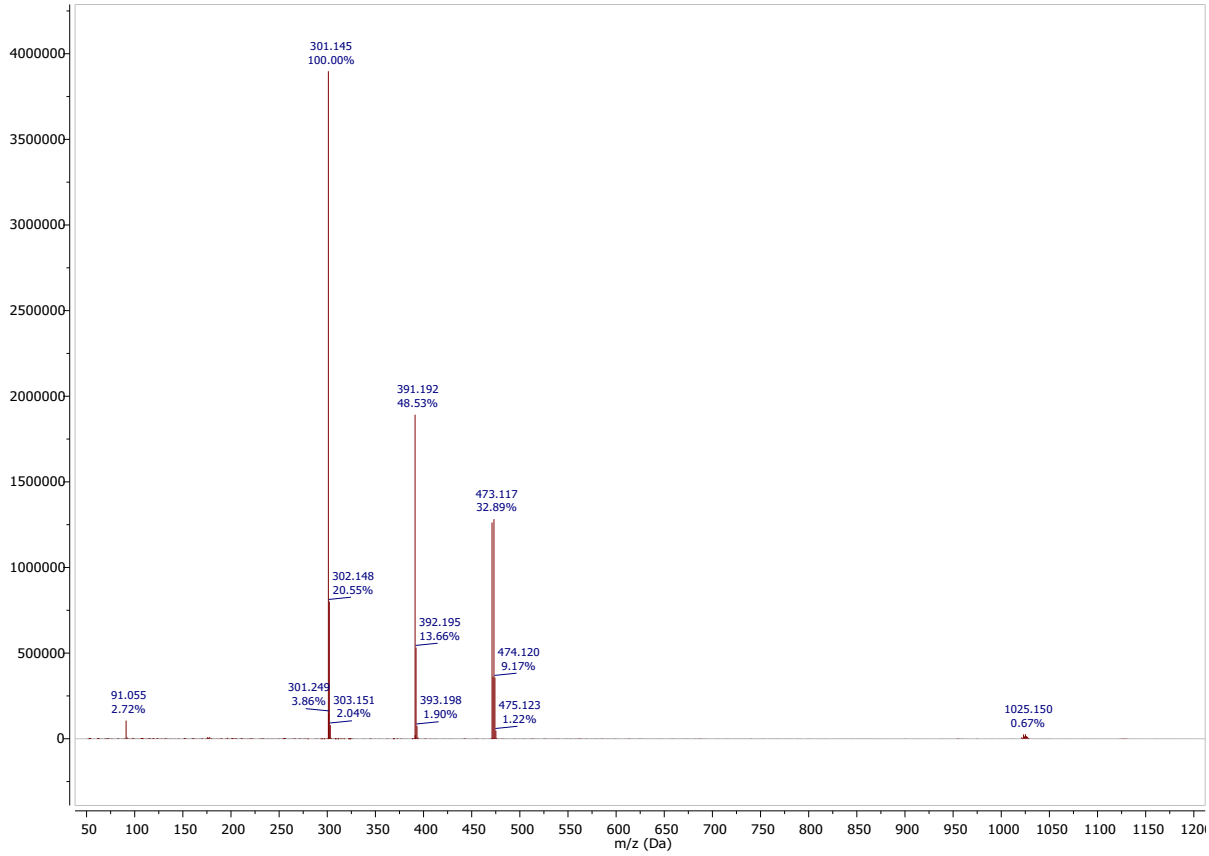

Figure S46: Mass spectrum of **2-Ph**

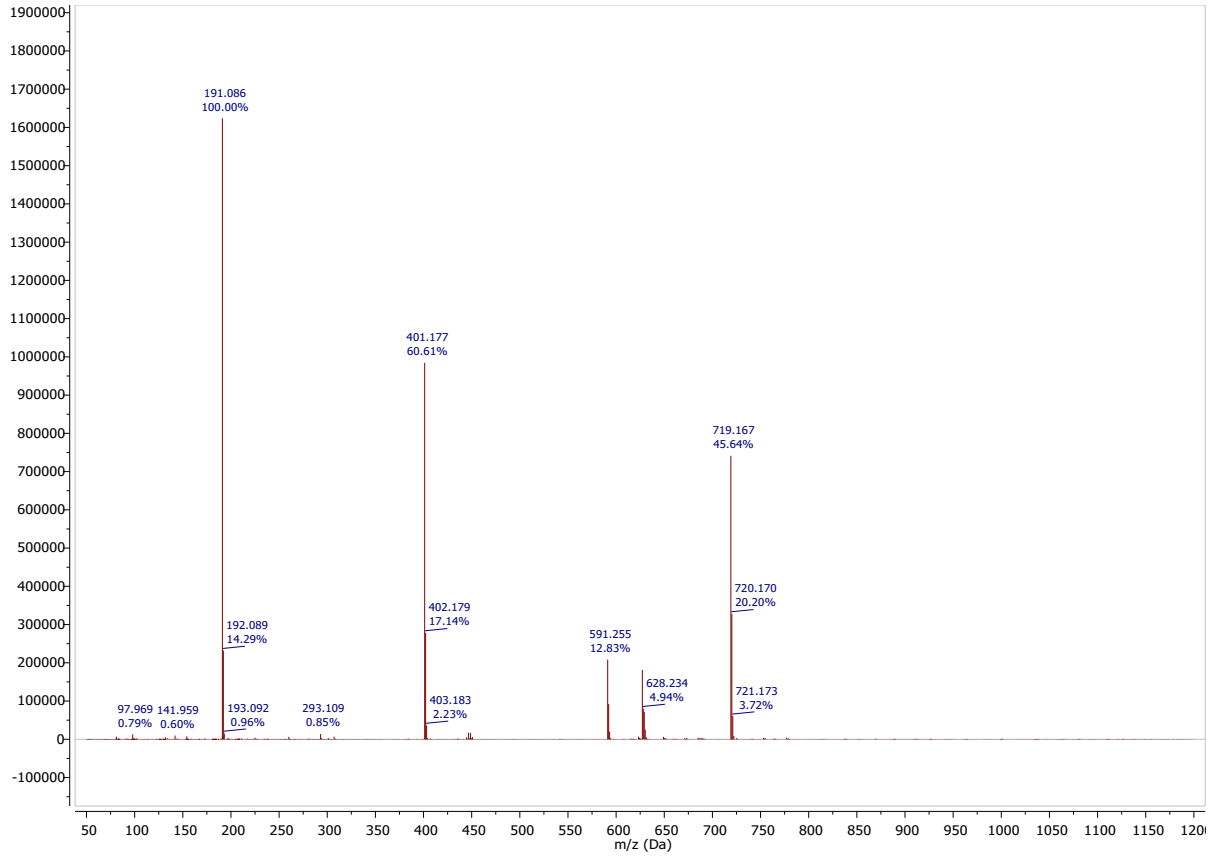

Figure S47: Mass spectrum of **2-Ant**

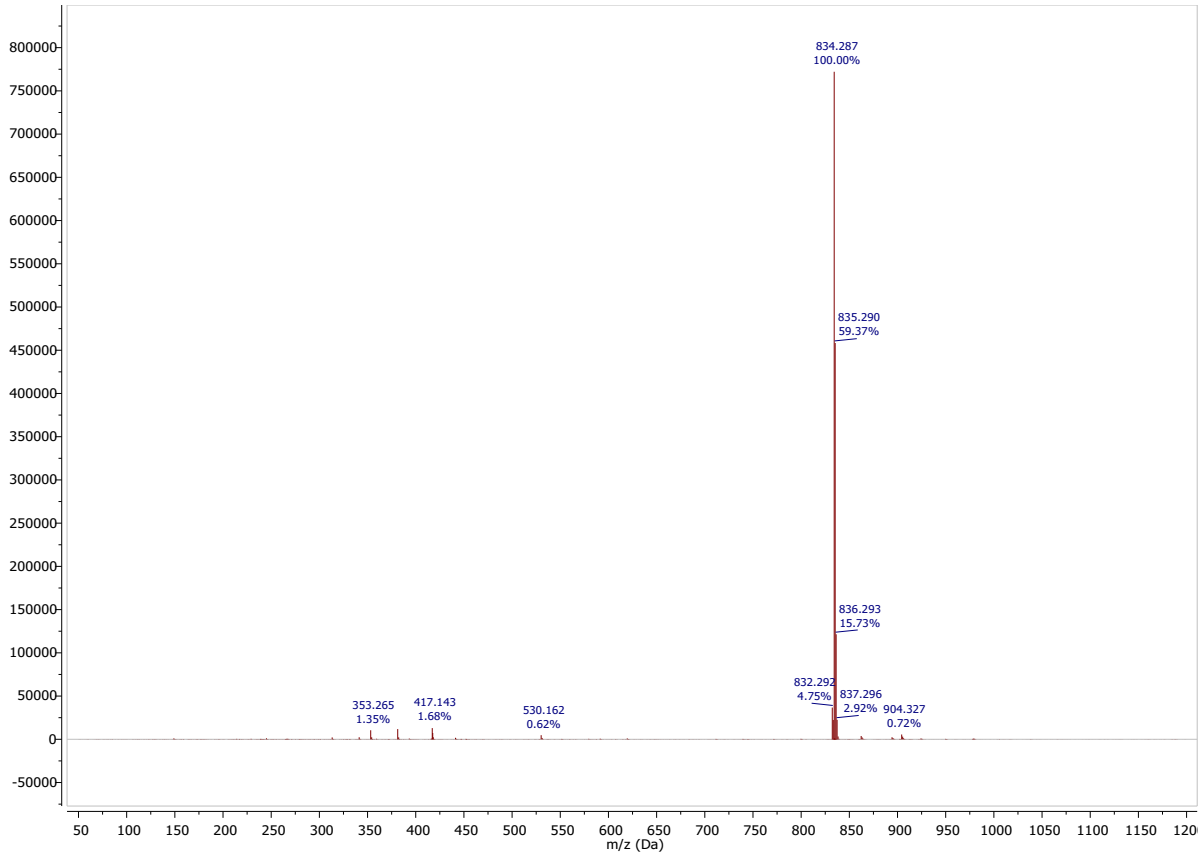

Figure S48: Mass spectrum of **$[Fe((ImPh)_2P)_2]^+$**

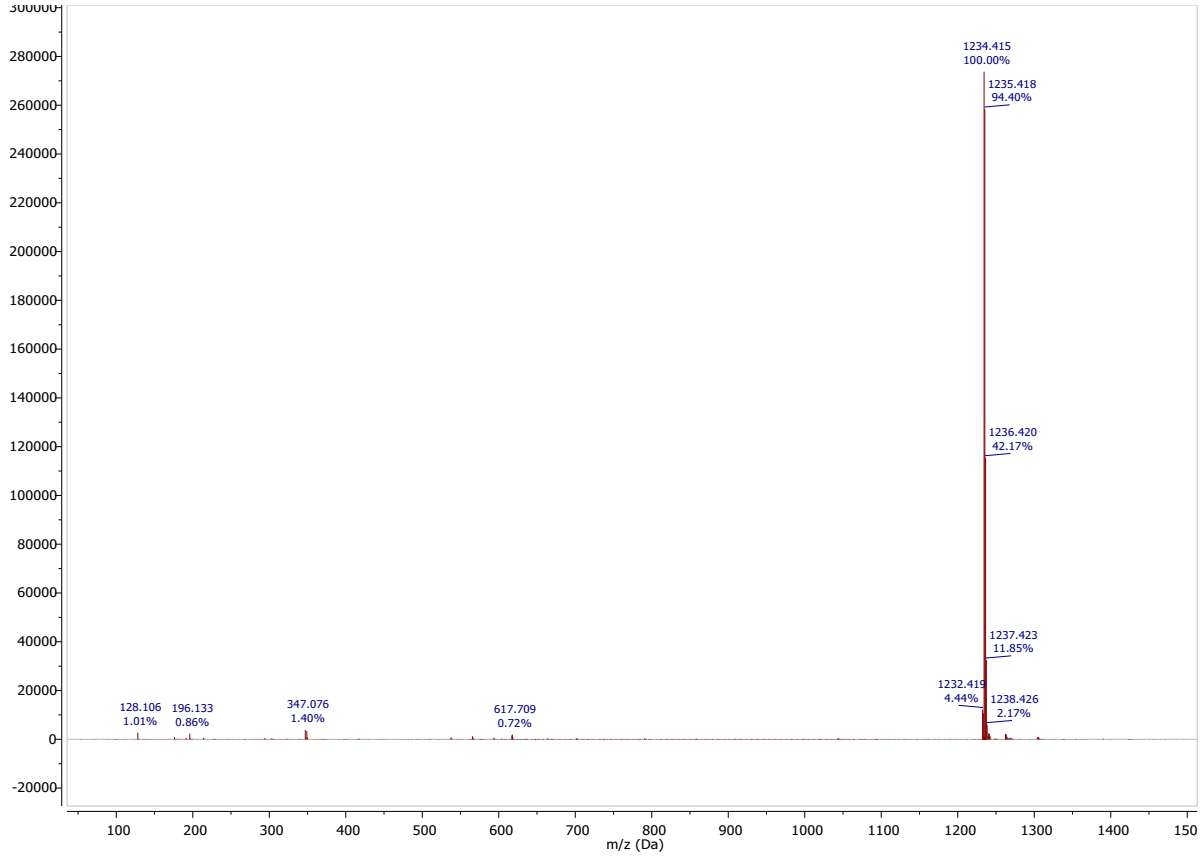

Figure S49: Mass spectrum of **$[Fe((ImAnt)_2P)_2]^+$**

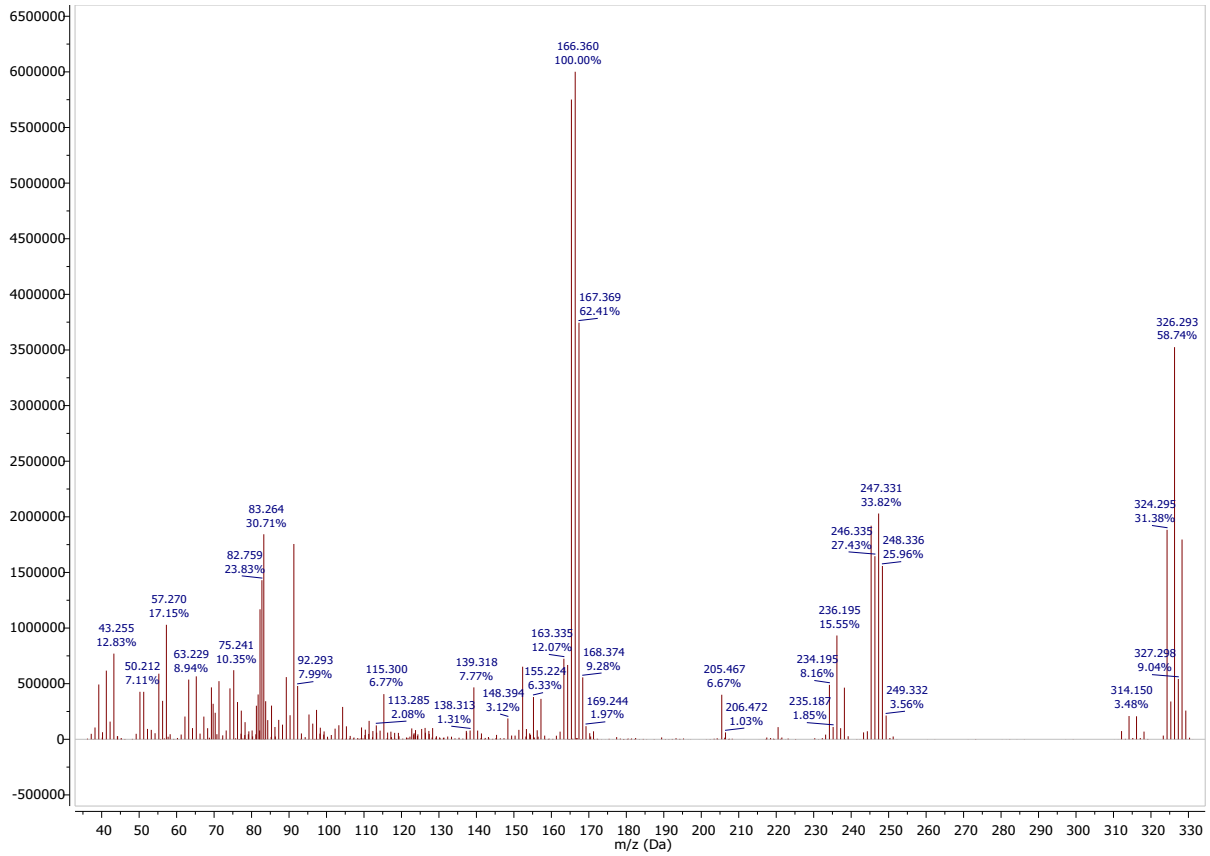

Figure S50: Mass spectrum **3-Ph**

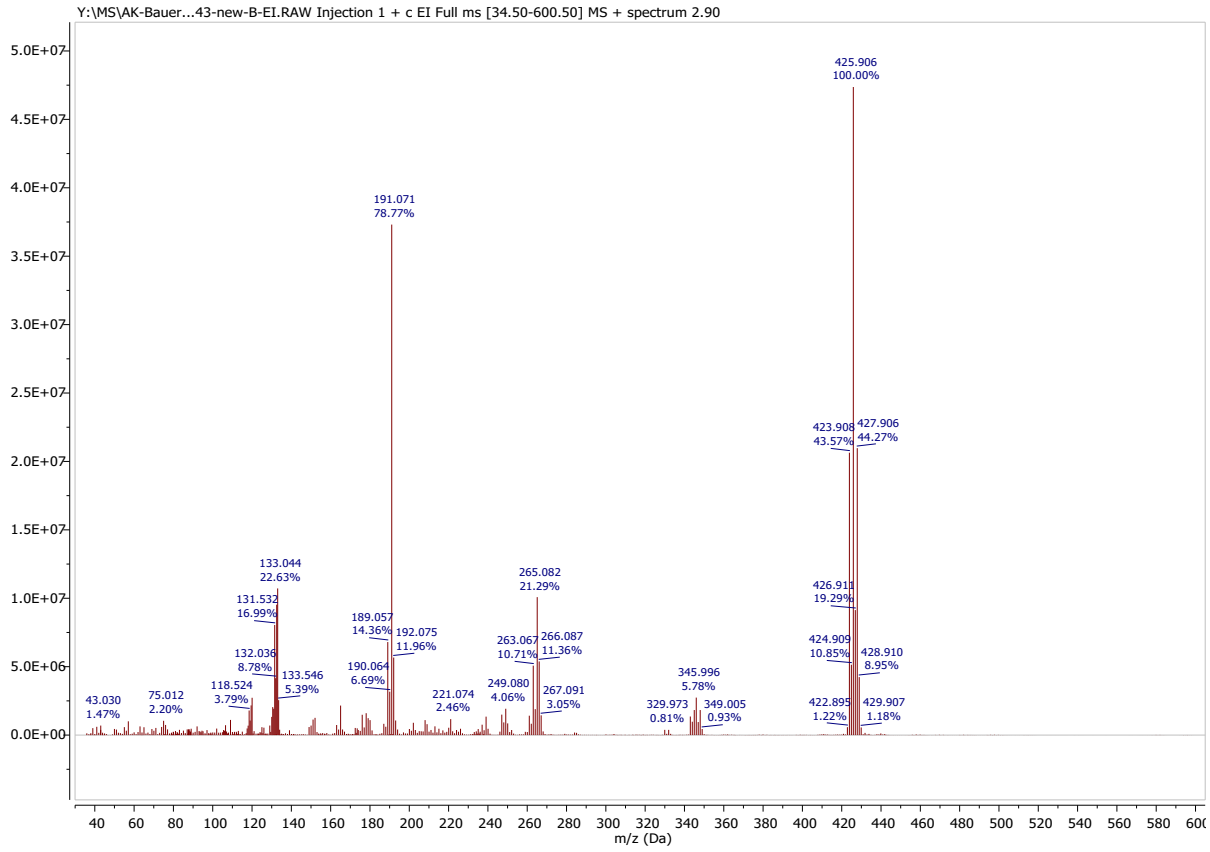

Figure S51: Mass spectrum **3-Ant**

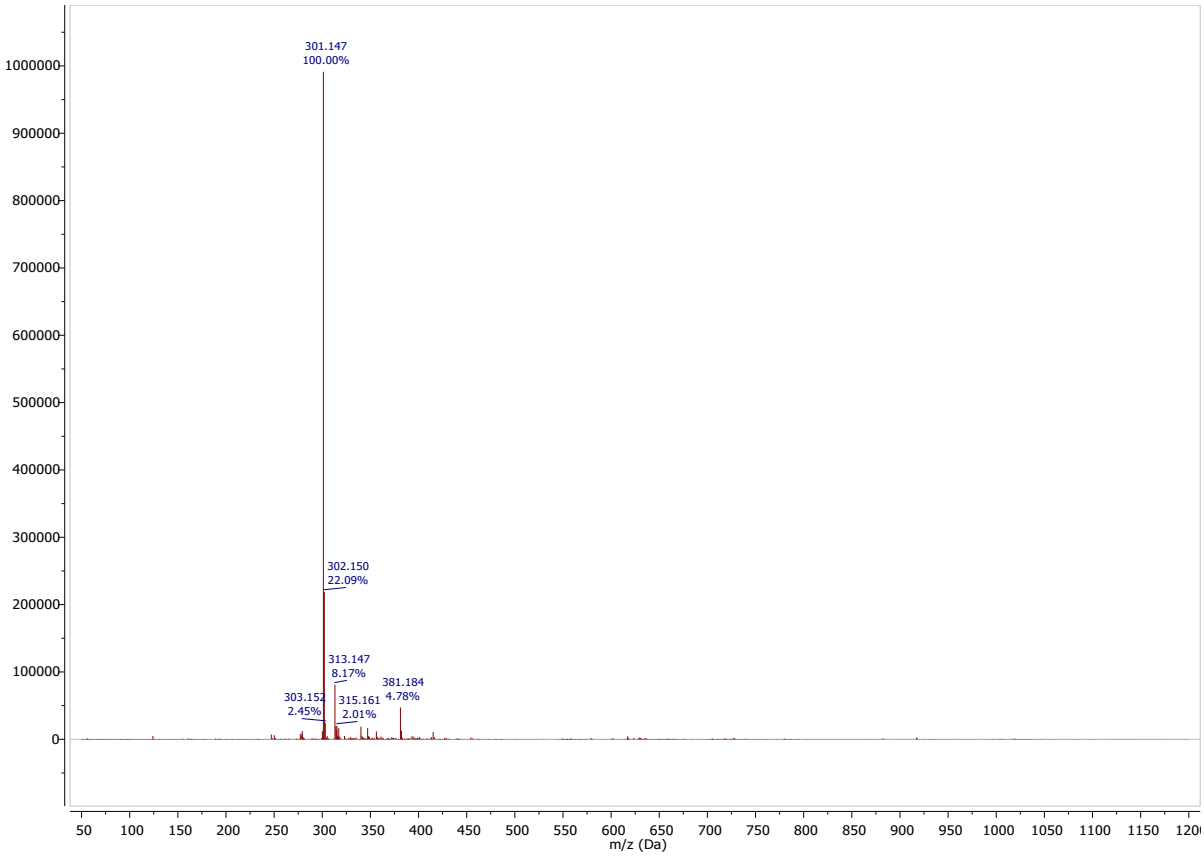

Figure 52: Mass spectrum of **4-Ph**

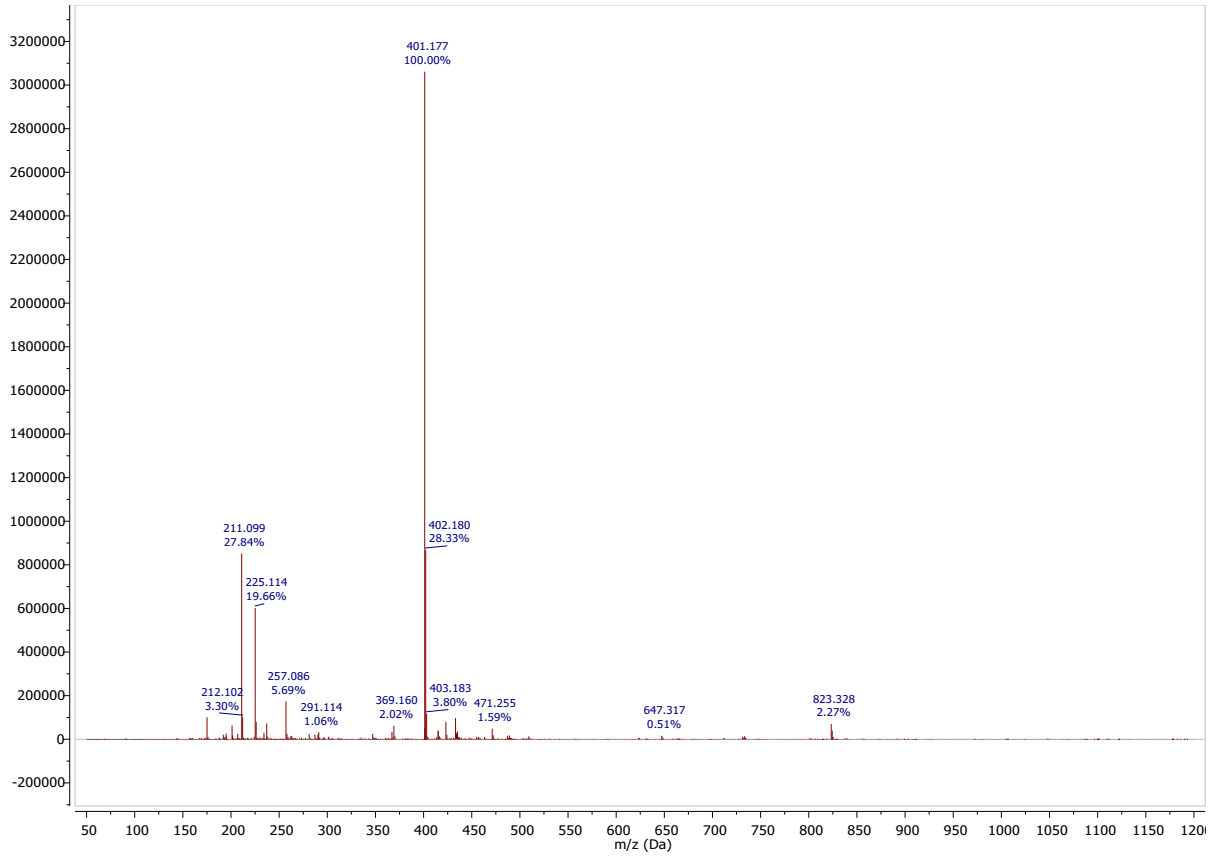

Figure S53: Mass spectrum of **4-Ant**

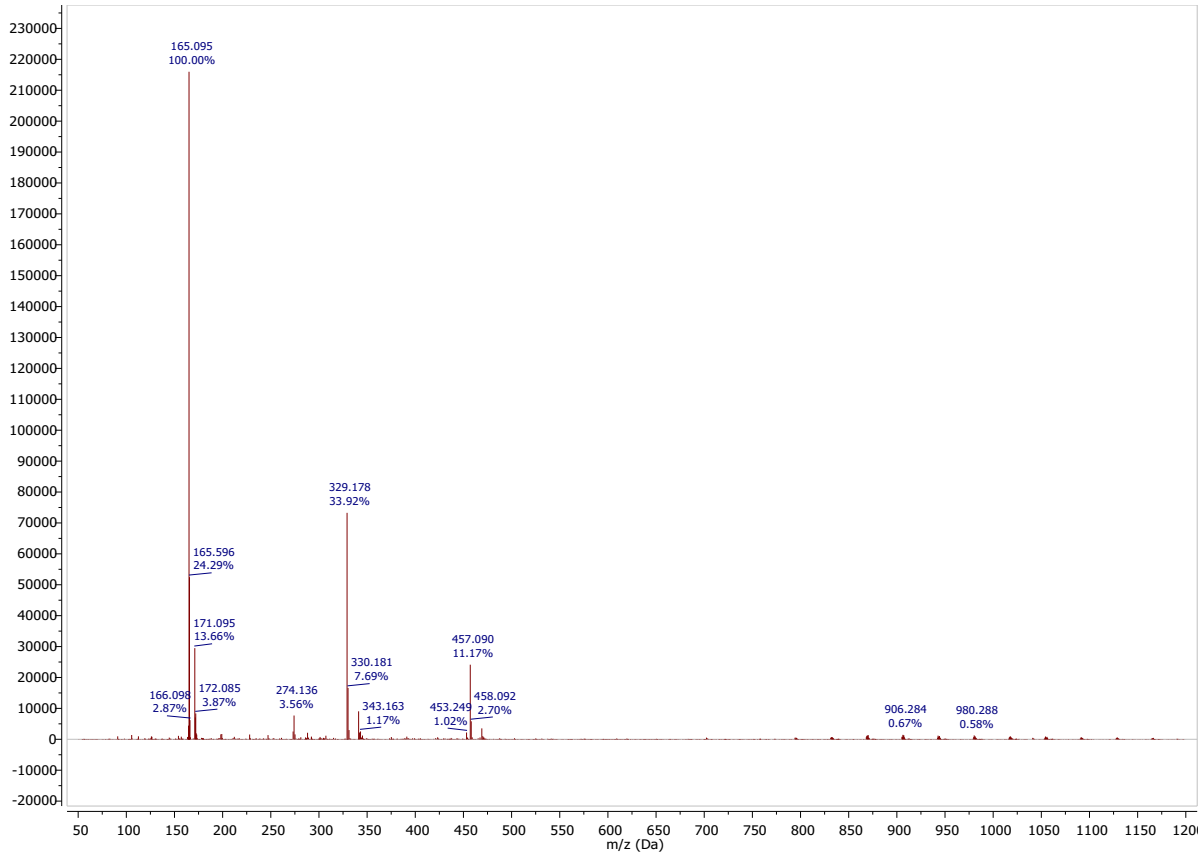

Figure S54: Mass spectrum of **5-Ph**

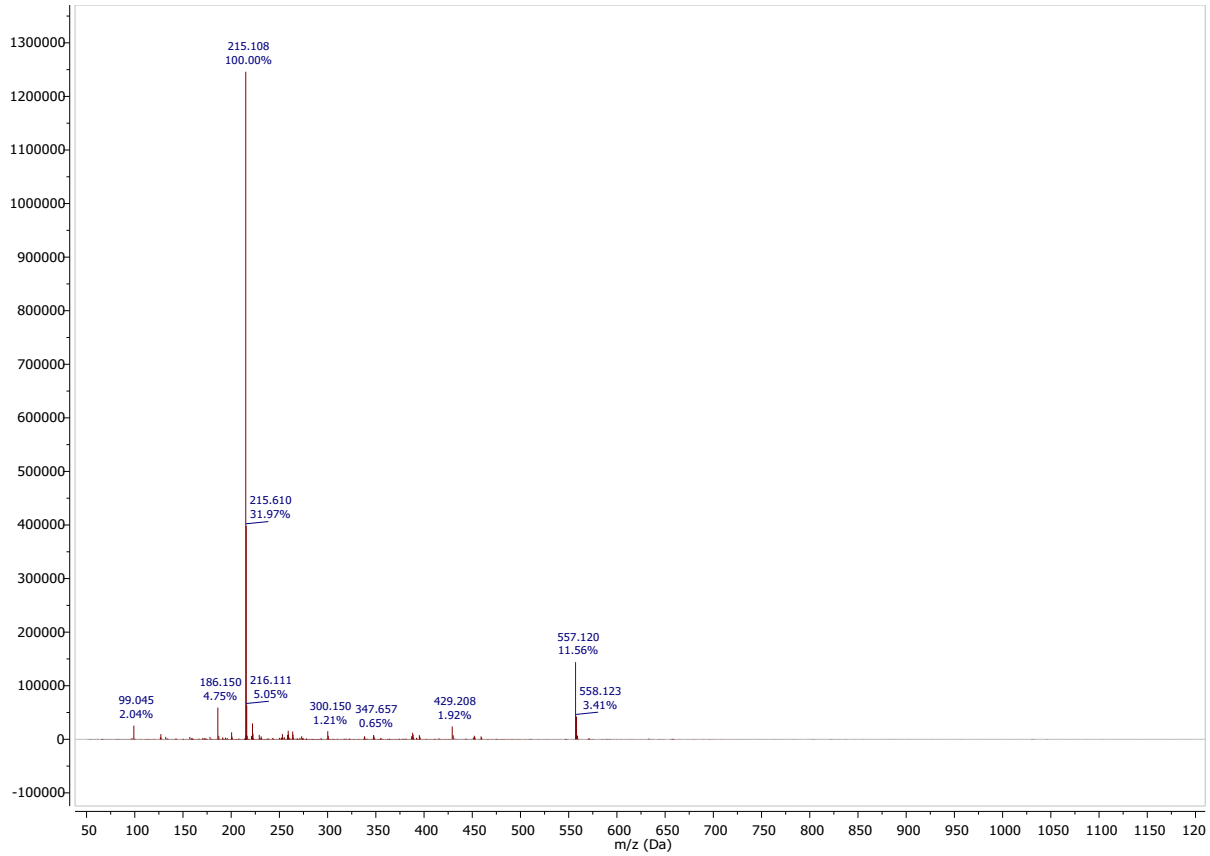

Figure S55: Mass spectrum of **5-Ant**

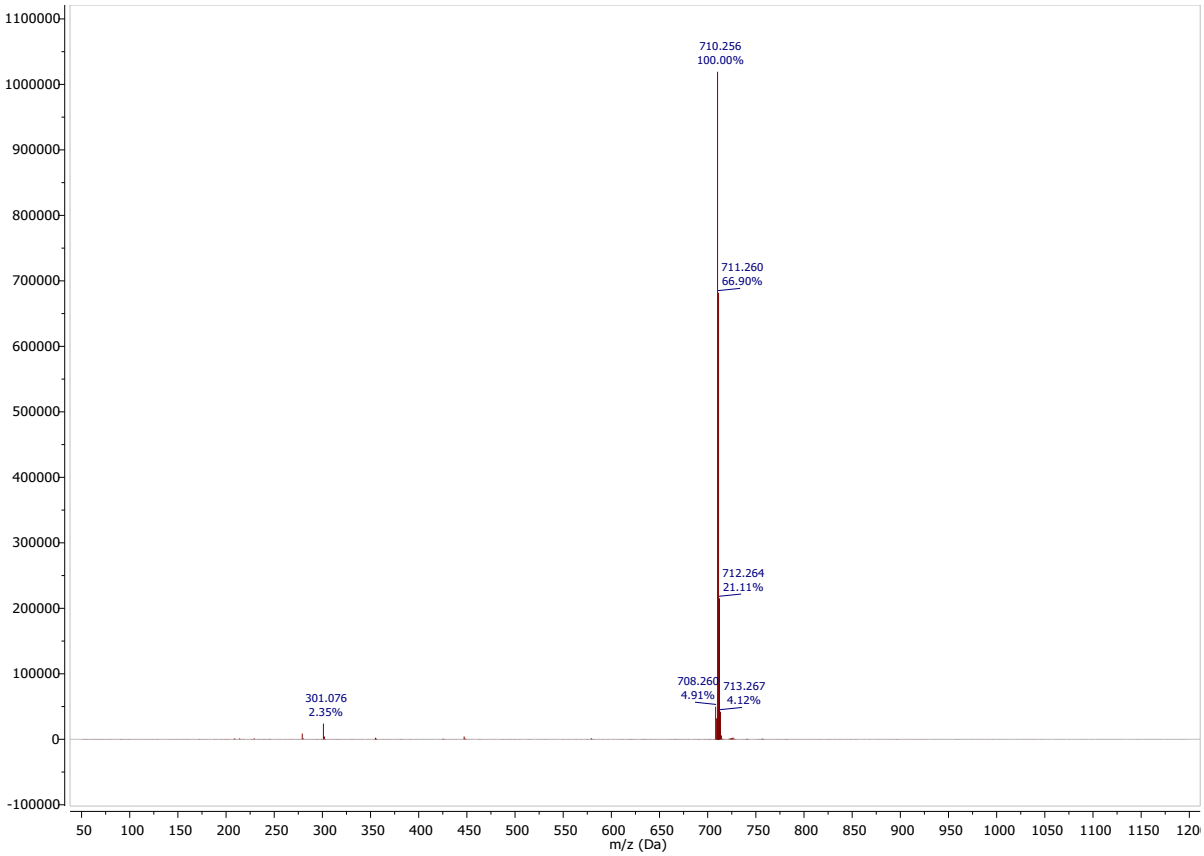

Figure S56: Mass spectrum of **$[Fe(Im_2PPh)_2]^+$**

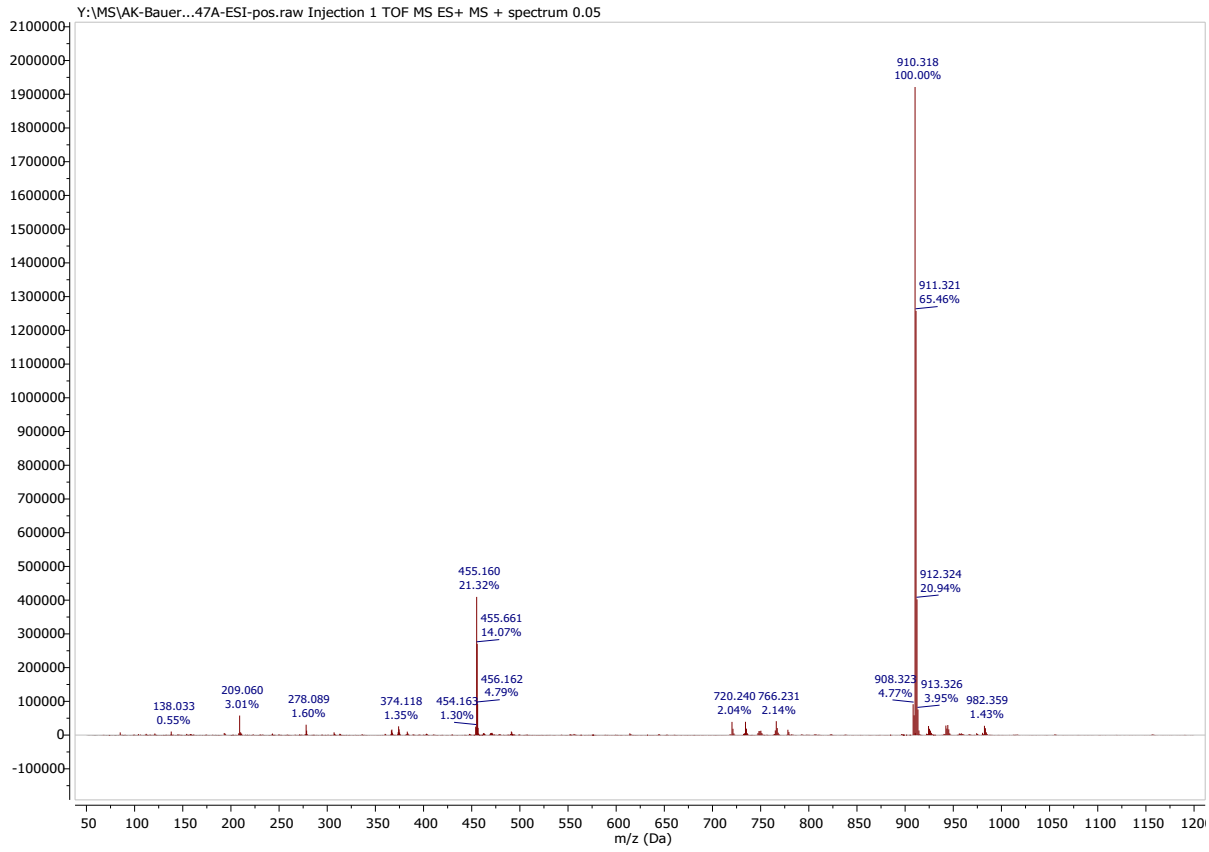

Figure S57: Mass spectrum of **[Fe(Im$_2$PAnt)$_2$]$^+$**

12. References

(1) Cho, J.; Hollis, T. K.; Valente, E. J.; Trate, J. M. CCC–N-heterocyclic carbene pincer complexes: Synthesis, characterization and hydroamination activity of a hafnium complex. *J. Organomet. Chem.* **2011**, *696* (1), 373–377.

(2) Brückner, R. *Reaktionsmechanismen*:*Organische Reaktionen, Stereochemie, moderne Synthesemethoden*, 3. Auflage, Nachdruck 2015; Lehrbuch; Springer Spektrum, **2004**.

(3) Steube, J.; Kruse, A.; Bokareva, O. S.; Reuter, T.; Demeshko, S.; Schoch, R.; Argüello Cordero, M. A.; Krishna, A.; Hohloch, S.; Meyer, F.; Heinze, K.; Kühn, O.; Lochbrunner, S.; Bauer, M. Janus-type emission from a cyclometalated iron(III) complex. *Nat. Chem.* **2023**, *15*, 468–474.

(4) Zhuang, L.; Wai, J. S.; Embrey, M. W.; Fisher, T. E.; Egbertson, M. S.; Payne, L. S.; Guare, J. P.; Vacca, J. P.; Hazuda, D. J.; Felock, P. J.; Wolfe, A. L.; Stillmock, K. A.; Witmer, M. V.; Moyer, G.; Schleif, W. A.; Gabryelski, L. J.; Leonard, Y. M.; Lynch, J. J.; Michelson, S. R.; Young, S. D. Design and synthesis of 8-hydroxy-1,6naphthyridines as novel inhibitors of HIV-1 integrase in vitro and in infected cells. *J. Med. Chem.* **2003**, *46* (4), 453–456.

(5) Li, C.; Gao, C.; Lan, J.; You, J.; Gao, G. An AIE active Y-shaped diimidazolylbenzene: aggregation and disaggregation for Cd(2+) and Fe(3+) sensing in aqueous solution. *Org. Biomol. Chem.* **2014**, *12* (47), 9524–9527.

(6) Rubio, R. J.; Andavan, G. T. S.; Bauer, E. B.; Hollis, T. K.; Cho, J.; Tham, F. S.; Donnadieu, B. Toward a general method for CCC N-heterocyclic carbene pincer synthesis: Metallation and transmetallation strategies for concurrent activation of three C–H bonds. *J. Organomet. Chem.* **2005**, *690* (23), 5353–5364.

(7) Zimmer, P.; Müller, P.; Burkhardt, L.; Schepper, R.; Neuba, A.; Steube, J.; Dietrich, F.; Flörke, U.; Mangold, S.; Gerhards, M.; Bauer, M. N-Heterocyclic Carbene Complexes of Iron as Photosensitizers for Light-Induced Water Reduction. *Eur. J. Inorg. Chem.* **2017**, *2017* (11), 1504–1509.

(8) Randles, J. E. B. A cathode ray polarograph. Part II.—The current-voltage curves. *Trans. Faraday Soc.* **1948**, *44* (0), 327–338.

(9) Päpcke, A.; Friedrich, A.; Lochbrunner, S. Revealing the initial steps in homogeneous photocatalysis by time-resolved spectroscopy. *J. Condens. Matter Phys.* **2020**, *32* (15), 153001.

(10) Neese, F. The ORCA program system. *WIREs Comput. Mol. Sci.* **2012**, *2* (1), 73–78.

(11) Grimme, S.; Brandenburg, J. G.; Bannwarth, C.; Hansen, A. Consistent structures and interactions by density functional theory with small atomic orbital basis sets. *Chem. Phys.* **2015**, *143* (5), 54107.

(12) Becke, A. D. Density-functional thermochemistry. III. The role of exact exchange. *J. Chem. Phys.* **1993**, *98* (7), 5648–5652.

(13) Weigend, F.; Ahlrichs, R. Balanced basis sets of split valence, triple zeta valence and quadruple zeta valence quality for H to Rn: Design and assessment of accuracy. *Phys. Chem. Chem. Phys.* **2005**, *7* (18), 3297–3305.

(14) Caldeweyher, E.; Bannwarth, C.; Grimme, S. Extension of the D3 dispersion coefficient model. *J. Chem. Phys.* **2017**, *147* (3), 34112.

(15) Dreuw, A.; Head-Gordon, M. Single-reference ab initio methods for the calculation of excited states of large molecules. *Chemical reviews* **2005**, *105* (11), 4009–4037.

(16) Plasser, F. TheoDORE: A toolbox for a detailed and automated analysis of electronic excited state computations. *J. Chem. Phys.* **2020**, *152* (8), 84108.

(17) Knizia, G. Intrinsic Atomic Orbitals: An Unbiased Bridge between Quantum Theory and Chemical Concepts. *J. Chem. Theory Comput.* **2013**, *9* (11), 4834–4843.

(18) Günther, H. *NMR Spectroscopy*:*Basic Principles, Concepts, and Applications in Chemistry*, 3. Auflage; Wiley-VCH, **2013**.

(19) Schmitz, L.; Argüello Cordero, M. A.; Al-Marri, M. J.; Schoch, R.; Egold, H.; Neuba, A.; Steube, J.; Bracht, B.; Bokareva, O. S.; Lochbrunner, S.; Bauer, M. Chromophore Induced Effects in Iron(III) Complexes. *Inorg. Chem.* **2025**, *64* (28), 14101–14117.